Order Number 9510641

Surface wave studies at air/liquid interfaces

Cao, Beihua, Ph.D.

City University of New York, 1995

U·M·I
300 N. Zeeb Rd.
Ann Arbor, MI 48106

SURFACE WAVE STUDIES AT AIR/LIQUID INTERFACES

by

BEIHUA CAO

A dissertation submitted to the Graduate Faculty in Physics in partial fulfillment of the requirements for the degree of Doctor of Philosophy, The City University of New York.

1994

This manuscript has been read and accepted for the Graduate Faculty in Physics in satisfaction of the dissertation requirement for the degree of Doctor of Philosophy.

July 6, 1994
Date

Prof. H. Z. Cummins
Chair of Examining Committee

August 10, 1994
Date

Prof. E. Tryon
Executive Officer

Dr. M. W. Kim

Prof. F. W. Smith

Prof. J. Koplik

Prof. M. Tomkiewicz

Supervisory Committee

Abstract

SURFACE WAVE STUDIES AT AIR/LIQUID INTERFACES

by

Beihua Cao

Advisers: Dr. Mahn Won Kim and Prof. Herman Z. Cummins

We use surface heterodyne light scattering to study the thermally excited surface waves at the interface between air and a polymer solution. Three specific polymer solutions are chosen to vary the degree of surface adsorption from a depletion layer to an adsorption layer. The first solution is polyisobutylene (PIB) in decane, which exhibits no depletion or adsorption at the interface; the second one is polybromostyrene (PBrS) in toluene which exhibits a depletion layer; and the third one is polyethyleneoxide (PEO) in water, which exhibits an adsorption layer since the polymer is surface active. Since the thicknesses of the depletion and adsorption layers depend on the molecular weight, we also study the interfacial properties of PBrS in toluene and PEO in water using polymers with both low and high molecular weights.

We measure the power spectra at several scattering vectors, and as the bulk polymer concentration and molecular weight are varied. Two theoretical models are used to analyze the experimental data. The first model uses the theory for capillary waves at a simple liquid interface. The second model uses the theory for viscoelastic polymer solutions at an air/solution interface.

For PIB in decane, we find that the theory for viscoelastic polymer solutions is a more suitable model for relatively high polymer concentrations; it also gives better results for the surface tensions and viscosities.

For PBrS in toluene, we find that, for low molecular weight (90K), the surface waves lie in the capillary wave regime over the entire concentration range accessible to our experiments. By contrast, for high molecular weight (900K) at high polymer concentrations, the surface waves are strongly affected by the viscoelastic behavior of the bulk. In all cases, the depletion layers have no effect on the surface waves. This result is consistent with the small thickness of the depletion layers.

For PEO in water, we find that, for low molecular weight (85K), the surface wave motion is strongly modified by the presence of the adsorption layers. By contrast, for high molecular weight (1000K), the adsorption layers appear to have no effect on the surface waves. This is consistent with the results of surface tension and ellipsometry measurements, which show that 85K PEO forms very dense and thick adsorption layers at the solution interface while 1000K PEO can not form this type of adsorption layer. We also show experimentally that the surface waves of PEO/water solutions with M_w = 1000K cross over from capillary waves to elastic waves as the polymer concentration is increased.

Finally, we study the interfacial properties of graft copolymers at the air/water interface using a surface balance, ellipsometry, surface light scattering and atomic force microscopy (AFM). This combination of techniques enables us to determine the surface structure of monolayers of graft copolymers at the air/water interface.

Acknowledgments

I wish to thank all people who have helped me during my thesis work at the Exxon Corporate Research Labs and during my graduate course work at the City College of New York.

I wish to thank Dr. Mahn Won Kim, who is my thesis advisor at the Exxon Corporate Research Labs, for his guidance and support. I would like to thank Prof. Herman Cummins, who is my adviser at the City College of New York, for many enlightening discussions and suggestions. I also want to express my special thanks to Dr. Dave Weitz for many fruitful discussions, suggestions and encouragement. He also improved my English writing a great deal with his patience.

I wish to thank my parents, Nanshan Cao and Yuqing Zhang, whom I love with all my heart, for their constant support and understanding.

Finally, I want to thank my husband, Han Chang, who always encourages and supports me. This thesis is dedicated to him.

To My Family

Table of Contents

ABSTRACT iv

ACKNOWLEDGMENTS vi

LIST OF FIGURES xi

Chapter 1 INTRODUCTION 1

References 5

Chapter 2 THEORETICAL BACKGROUND 7

2.1 Introduction to Polymers 7

2.2 Theory of Light Beating Spectroscopy 18

2.2.1 Heterodyne Detection 19

2.2.2 Homodyne Detection 21

2.3 Surface Waves on Liquid Interfaces 22

2.31 Dispersion Equation for Capillary Waves 23

2.32 Theoretical Power Spectrum for a Monolayer-Covered Surface 34

2.33 Dispersion Equation for Surface waves of Concentrated Polymer Solutions 36

2.34 Theoretical Power Spectrum of Thermal Fluctuation on an air/solution Interface 42

References 46

Chapter 3	EXPERIMENTAL METHODS	48
3.1	Surface Tension Measurements	48
3.2	The Technique of Surface Heterodyne Light Scattering	51
3.3	Rheological Measurements	59
	References	65
Chapter 4	SURFACE WAVES STUDIES OF POLYMER SOLUTIONS	66
4.1	Introduction	66
4.2	Surface Waves at Air/solution Interfaces of Polyisobutylene (PIB)/decane	72
4.3	Molecular Weight Dependence of Surface Waves at Air/solutions Interfaces of Polybromostyrene (PBrS)/toluene	81
	4.3.1 Polybromostyrene (PBrS) with Molecular Weight 90K	82
	4.3.2 Polybromostyrene (PBrS) with Molecular Weight 900K	89
4.4	Adsorption effects on Surface Waves at Air/solution Interfaces of Polyethyleneoxide (PEO)/water	97
	4.4.1 Polyethyleneoxide (PEO) with Molecular Weight 85K	99
	4.4.2 Polyethyleneoxide (PEO) with Molecular Weight 1000K	110
4.5	Conclusions	121
	References	123

Appendices 125

(A) Surface Activity of Polyethyleneoxide (PEO) 125

Abstract 125

Introduction 125

Experimental Section 128

Results and Discussion 129

References 150

(B) Interfacial Properties of Model Graft Copolymers 152

Abstract 152

Introduction 152

Experimental Section 156

Results and Discussion 159

References 170

BIBLIOGRAPHY 171

List of Figures

Fig. 2.1. Symbolic representations of linear and branched macromolecules (high-density polyethylene and low-density polyethylene, respectively): (a) linear, (b) branched.
Page 8

Fig. 2.2. Crossover between dilute and semi-dilute solutions: (a) dilute, (b) onset of overlap, and (c) semi-dilute.
Page 12

Fig. 2.3. A magnified view of polymer solutions at the semi-dilute regime.
Page 15

Fig. 2.4. Insoluble monomolecular monolayers at an air/water interface.
Page 26

Fig.2.5. Possible motions at the interfacial plane. The interface is in the x-y plane and the cylinders represent cross sections of the monolayer.
Page 28

Fig. 2.6. Surface mode diagram for polymer solutions showing regions of capillary, Rayleigh elastic, and overdamped liquid modes as a function of wave vector, k, and elastic modulus, G_0. Axes are scaled logarithmically, and mode regime boundaries are indicated by a characteristic wave vector $k_+ = \rho\sigma/\eta_s^2$ a characteristic modulus $G_+ = \rho\ (\sigma/\eta_s)^2$, where ρ and σ are,

respectively, the density and the surface tension of the polymer solutions, and where η_S is the viscosity of the solvent. The cuts along the k axis schematically indicate the existence of upper and lower bounds on the allowed wave vectors.

Page 41

Fig. 3.1. A Wilhelmy plate partially immersed in a water surface. The lower diagram shows the detailed side view of the plate.

Page 50

Fig. 3.2. The experimental setup for the technique of surface heterodyne light scattering.

Page 52

Fig. 3.3. A schematic drawing of the scattering process at the liquid surface. The laser light is incident on the surface with an angle $\theta_i \sim 60^0$. Scattered light from the incident beam is optically mixed with a diffracted beam. In this example, the PMT is centered on the third order diffraction spot from the transmission grating, and the scattering angle is defined by φ.

Page 56

Fig. 3.4. Power spectrum of water at the diffraction order n = 3. The solid line is the fit using Eq. (3.1) with $k = 137.87$ cm^{-1} and $\delta_d = 9.94$.

Page 58

Fig. 3.5. A Couette viscometer with sample loaded.

Page 60

Fig. 3.6. Cone and plate geometry with sample loaded.

Page 62

Fig. 3.7. Rheological measurements as a function of frequency ω for the 7.4 g/dl PEO/water solution with M_W = 1000K. The symbols correspond to: ● storage moduli G' and ■ loss moduli G''.

Page 64

Fig. 4.1. The chemical structures of the polymers used in this thesis.

Page 67

Fig. 4.2. Power spectra of the 8.0 g/dl concentration PIB/decane at the diffraction orders 2-4, corresponding to k = 105.1, 160.7, and 218.2 cm^{-1}. They are rescaled to have the same baseline. The solids lines are the fits using Eq. (4.2). The symbols correspond to: ● n=2; ◆ n=3; and ▲ n=4.

Page 74

Fig. 4.3. Power spectra of the 0.5 g/dl concentration PIB/decane at the diffraction orders 2-4, corresponding to k = 105.1, 160.7, and 218.2 cm^{-1}. They are rescaled to have the same baseline. The solids lines are the fits using Eq. (4.2). The symbols correspond to: ● n=2; ◆ n=3; and ▲ n=4.

Page 75

Fig. 4.4(a). Power spectra of the 4.0 g/dl concentration PIB/decane at the diffraction orders 2-4, corresponding to k = 105.1, 160.7, and 218.2 cm^{-1}. They are rescaled to have the same baseline. The solids lines are the fits using Eq. (4.2). The symbols correspond to: ● n=2; ◆ n=3; and ▲ n=4.

Fig. 4.4(b). Power spectra of the 4.0 g/dl concentration PIB/decane at the diffraction orders 5-8, corresponding to k = 276.3, 332.3, 388.4, and 442.0 cm^{-1}. They are rescaled to have the same baseline. The solids lines are the fits using Eq. (4.2). The symbols correspond to: ● n=5; ◆ n=6; ▲ n=7; and ▼ n=8.

Page 76

Fig. 4.5(a). Peak frequency, f_p, *vs.* bulk concentration for PIB/decane at the diffraction orders 2-5. The smooth curves are drawn through the data points for clarity. The symbols correspond to: ● n=2; ■ n=3; ◆ n=4; and ▲ n=5.

Fig. 4.5(b). Experimental frequency width, Δf_{exp}, $vs.$ bulk concentration for PIB/decane at the diffraction orders 2-5. The smooth curves are drawn through the data points for clarity. The symbols correspond to: ● n=2; ■ n=3; ◆ n=4; and ▲ n=5.

Page 77

Fig. 4.6. Plot showing the relationship between α, obtained from the fits of $\ln(f_p)$ *vs.* $\ln(k)$, and the bulk concentration of PIB/decane. The symbols correspond to: □ the theory for polymer solutions; + the capillary wave theory; and ◇ experimental.
Page 79

Fig. 4.7(a). Surface tension, σ, *vs.* bulk concentration of PIB/decane. The symbols correspond to: □ data obtained from the du Nouy ring method; o data obtained from the spectral fits using the capillary wave theory, Eq. (4.1); and ◇ data obtained from the spectral fits using the theory for polymer solutions, Eq. (4.2).

Fig. 4.7(b). Viscosity, η, *vs.* bulk concentration of PIB/decane. The symbols correspond to: □ data obtained from a Couette viscometer; o data obtained from the spectral fits using the capillary wave theory, Eq. (4.1); and ◇ data obtained from the spectral fits using the theory for polymer solutions, Eq. (4.2).
Page 80

Fig. 4.8. Power spectra of the 20.0 g/dl concentration PBrS/toluene with M_W = 90K at the diffraction orders 2-4, corresponding to = 94.1, 144.8, and 193.9 cm^{-1}. They are rescaled to have the same baseline. The solids lines are the fits using Eq. (4.2). The symbols correspond to: ● n=2; ◆ n=3; and ▲ n=4.
Page 83

Fig. 4.9. Power spectra of the 11.0 g/dl concentration PBrS/toluene with M_W = 90K at the diffraction orders 2-4, corresponding to k = 94.1, 144.8, and 193.9 cm^{-1}. They are rescaled to have the same baseline. The solids lines are the fits using Eq. (4.2). The symbols correspond to: ● n=2; ◆ n=3; and ▲ n=4.

Page 84

Fig. 4.10. Power spectra of the 3.0 g/dl concentration PBrS/toluene with M_W = 90K at the diffraction orders 2-4, corresponding to k = 94.1, 144.8, and 193.9 cm^{-1}. They are rescaled to have the same baseline. The solids lines are the fits using Eq. (4.2). The symbols correspond to: ● n=2; ◆ n=3; and ▲ n=4.

Page 85

Fig. 4.11(a). Peak frequency, f_p, *vs.* bulk concentration of PBrS/toluene with M_W = 90K at the diffraction orders 2-5. The smooth curves are drawn through the data points for clarity. The symbols correspond to: ● n=2; ■ n=3; ◆ n=4; and ▼ n=5.

Fig. 4.11(b). Experimental frequency width, Δf_{exp}, *vs.* bulk concentration of PBrS/toluene with M_W = 90K at the diffraction orders 2-5. The smooth curves are drawn over the data points for clarity. The symbols correspond to: ● n=2; ■ n=3; ◆ n=4; and ▲ n=5.

Page 86

Fig. 4.12(a). Surface tension, σ, $vs.$ bulk concentration of PBrS/toluene with M_W = 90K. The symbols correspond to: □ data obtained from the du Nouy ring method; o data obtained from the spectral fits using the capillary wave theory, Eq. (4.1); and ◇ data obtained from the spectral fits using the theory for polymer solutions, Eq. (4.2).

Fig. 4.12(b). Viscosity, η, *vs.* bulk concentration of PBrS/toluene with M_W = 90K. The symbols correspond to: □ data obtained from a Couette viscometer; o data obtained from the spectral fits using the capillary wave theory, Eq. (4.1); and ◇ data obtained from the spectral fits using the theory for polymer solutions, Eq. (4.2).

Page 88

Fig. 4.13. Power spectra of the 7.0 g/dl concentration PBrS/toluene with M_W = 900K at the diffraction orders 2-4, corresponding to k = 97.4, 146.1, and 194.5 cm^{-1}. They are rescaled to have the same baseline. The solids lines are the fits using Eq. (4.2). The symbols correspond to: ● n=2; ◆ n=3; and ▲ n=4.

Page 90

Fig. 4.14. Power spectra of the 4.0 g/dl concentration PBrS/toluene with M_W = 900K at the diffraction orders 2-4, corresponding to k = 97.4, 146.1, and 194.5 cm^{-1}. They are rescaled to have the same baseline. The solids lines are the fits using Eq. (4.2). The symbols correspond to: ● n=2; ◆ n=3; and ▲ n=4.

Page 91

Fig. 4.15. Power spectra of the 0.5 g/dl concentration PBrS/toluene with M_W = 900K at the diffraction orders 2-4, corresponding to k = 97.4, 146.1, and 194.5 cm^{-1}. They are rescaled to have the same baseline. The solids lines are the fits using Eq. (4.2). The symbols correspond to: ● n=2; ◆ n=3; and ▲ n=4.

Page 92

Fig. 4.16. Experimental power spectrum of the 7.0 g/dl concentration PBrS/toluene for $k = 97.4\ cm^{-1}$. The dashed line shows the power spectrum for the same k, using Eq. (4.1) with $\sigma = 27.5$ dyne/cm, $\eta = 43.8$ cp, and $\delta_d = 12.1$.

Page 93

Fig. 4.17(a). Surface tension, σ, $vs.$ bulk concentration of PBrS/toluene with $M_W = 900K$. The symbols correspond to: □ data obtained from the du Nouy ring method; o data obtained from the spectral fits using the capillary wave theory, Eq. (4.1); and ◇ data obtained from the spectral fits using the theory for polymer solutions, Eq. (4.2).

Fig. 4.17(b). Viscosity, η, $vs.$ bulk concentration for PBrS/toluene with M_W = 900K. The symbols correspond to: □ data obtained from a Couette viscometer; o data obtained from the spectral fits using the capillary wave theory, Eq. (4.1); and ◇ data obtained from the spectral fits using the theory for polymer solutions, Eq. (4.2).

Page 95

Fig. 4.18(a). Peak frequency, f_p, *vs.* bulk concentration of PBrS/toluene with M_W = 900K at the diffraction orders 2-5. The smooth curves are drawn through the data points for clarity. The symbols correspond to: ● n=2; ■ n=3; ◆ n=4; and ▲ n=5.

Fig. 4.18(b). Experimental frequency width, Δf_{exp}, *vs.* bulk concentration of PBrS/toluene with M_W = 900K at the diffraction orders 2-5. The smooth curves are drawn through the data points for clarity. The symbols correspond to: ● n=2; ■ n=3; ◆ n=4; and ▲ n=5.
Page 96

Fig. 4.19. Viscosity, η, and surface tension, σ, *vs.* bulk concentration of PEO/water with M_W = 85K. The symbols correspond to: ● viscosity from a Couette viscometer; ▲ surface tension from the du Nouy method. The smooth curves are drawn through the data points for clarity.
Page 100

Fig. 4.20. Power spectra of the 10.0 g/dl concentration PEO/water with M_W = 85K at the diffraction orders 2-4, corresponding to k = 91.7, 137.9, and 183.7 cm^{-1}. They are rescaled to have the same baseline. The solids lines are the fits using Eq. (4.2). The symbols correspond to: ● n=2; ◆ n=3; and ▲ n=4.
Page 101

Fig. 4.21. Power spectra of the 5.5 g/dl concentration PEO/water with M_W = 85K at the diffraction orders 2-4, corresponding to k = 91.7, 137.9, and 183.7 cm^{-1}. They are rescaled to have the same baseline. The solids lines are the fits using Eq. (4.2). The symbols correspond to: ● n=2; ◆ n=3; and ▲ n=4.

Page 102

Fig. 4.22. Power spectra of the 0.5 g/dl concentration PEO/water with M_W = 85K at the diffraction orders 2-4, corresponding to k = 91.7, 137.9, and 183.7 cm^{-1}. They are rescaled to have the same baseline. The solids lines are the fits using Eq. (4.2). The symbols correspond to: ● n=2; ◆ n=3; and ▲ n=4.

Page 103

Fig. 4.23(a). Peak frequency, f_p, *vs.* bulk concentration for PEO/water with M_W = 85K at the diffraction orders 2-5. The smooth curves are drawn through the data points for clarity. The symbols correspond to: ● n=2; ■ n=3; ◆ n=4; and ▲ n=5.

Fig. 4.23(b). Experimental frequency width, Δf_{exp}, $vs.$ bulk concentration for PEO/water with M_W = 85K at the diffraction orders 2-5. The smooth curves are drawn through the data points for clarity. The symbols correspond to: ● n=2; ■ n=3; ◆ n=4; and ▲ n=5.

Page 104

Fig. 4.24. Viscosity, η, *vs.* bulk concentration of PEO/water with M_W = 85K. The symbols correspond to: □ data obtained from a Couette viscometer; and o data obtained from the spectral fits using the theory for polymer solutions, Eq. (4.2).
Page 106

Fig. 4.25. Experimental Power spectrum of the 10.0 g/dl concentration PEO/water with M_W = 85K for k=137.9 cm^{-1}. The thin line is the fit using Eq. (4.2); the thick line is the fit using Eq. (4.4).
Page 107

Fig. 4.26(a). Surface longitudinal elasticity, ε, *vs.* bulk concentration of PEO/water with M_W = 85K. The symbols correspond to: ● n=2; ■ n=3; ◆ n=4; and ▲ n=5.

Fig. 4.26(b). Surface longitudinal viscosity, κ, *vs.* bulk concentration of PEO/water with M_W = 85K. The symbols correspond to: ● n=2; ■ n=3; ◆ n=4; and ▲ n=5.
Page 109

Fig. 4.27. Viscosity, η, and surface tension, σ, *vs.* bulk concentration of PEO/water with M_W = 1000K. The symbols correspond to: ● viscosity: from a Couette viscometer for bulk concentrations ≤ 2.5 g/dl, and from a cone and plate rheometer for bulk concentrations > 2.5 g/dl; and ▲ surface tension from the du Nouy method. The smooth curves are drawn through the data points for clarity.
Page 111

Fig. 4.28. Power spectra of the 5.0 g/dl concentration PEO/water with M_W = 1000K at the diffraction orders 2-4, corresponding to k = 88.6, 133.2, and 179.0 cm^{-1}. They are rescaled to have the same baseline. The solids lines are the fits using Eq. (4.2). The symbols correspond to: ● n=2; ◆ n=3; and ▲ n=4.

Page 113

Fig. 4.29. Power spectra of the 2.0 g/dl concentration PEO/water with M_W = 1000K at the diffraction orders 2-4, corresponding to k = 88.6, 133.2, and 179.0 cm^{-1}. They are rescaled to have the same baseline. The solids lines are the fits using Eq. (4.2). The symbols correspond to: ● n=2; ◆ n=3; and ▲ n=4.

Page 114

Fig. 4.30. Power spectra of the 0.5 g/dl concentration PEO/water with M_W = 1000K at the diffraction orders 2-4, corresponding to k = 88.6, 133.2, and 179.0 cm^{-1}. They are rescaled to have the same baseline. The solids lines are the fits using Eq. (4.2). The symbols correspond to: ● n=2; ◆ n=3; and ▲ n=4.

Page 115

Fig. 4.31(a). Power spectra of PEO/water with M_W = 1000K for k = 88.6 cm^{-1} at the different bulk concentrations. The symbols correspond to: ● 7.4 g/dl; ◆ 4.0 g/dl; and ▲ 3.0 g/dl. The solid lines are the fits using Eq. (4.2).

Fig. 4.31(b). Power spectra of PEO/water with M_W = 1000K for k = 88.6 cm^{-1} at the different bulk concentrations. The symbols correspond to: ● 2.0 g/dl; ◆ 0.75 g/dl; and ▲ 0.5 g/dl. The solid lines are the fits using Eq. (4.2).
Page 116

Fig. 4.32(a). Peak frequency, f_p, *vs.* bulk concentration of PEO/water with M_W = 1000K at the diffraction orders 2-5. The smooth curves are drawn through the data points for clarity. The symbols correspond to: ● n=2; ■ n=3; ◆ n=4; and ▲ n=5.

Fig. 4.32(b). Experimental frequency width, Δf_{exp}, *vs.* bulk concentration of PEO/water with M_W = 1000K at the diffraction orders 2-5. The smooth curves are drawn over the data points for clarity. The symbols correspond to: ● n=2; ■ n=3; ◆ n=4; and ▲ n=5.
Page 119

Fig. 4.33(a). Transient modulus, G_0, *vs.* bulk concentration of PEO/water with M_W = 1000K. The symbols correspond to: o data obtained from the spectral fits using the theory for polymer solutions, Eq. (4.2); and □ data obtained from the fits to the rheological measurements.

Fig. 4.33(b). Relaxation time, τ, *vs.* bulk concentration of PEO/water with M_W = 1000K. The symbols correspond to: o data obtained from the

spectral fits using the theory for polymer solutions, Eq. (4.2); and □ data obtained from the fits to the rheological measurements.
Page 120

Fig. A.1. A block diagram of the ellipsometry instrument.
Page 130

Fig. A.2. Surface pressure $\sigma_0-\sigma$ and the change in the ellipsometric phase angle *vs.* bulk concentration of PEO solutions with M_W = 85K. The symbols correspond to: ▲ surface pressure and o ellipsometry signal. The solid line is the fit to a polynomial function.
Page 130

Fig. A.3. Surface pressure and the change in the ellipsometric phase angle *vs.* surface concentration of an 85K PEO monolayer.
Page 132

Fig. A.4. Surface pressure and the change in the ellipsometric phase angle *vs.* surface concentration of a 100K CPC monolayer.
Page 134

Fig. A.5. Surface pressure, $\sigma_0-\sigma$, *vs.* bulk concentration of PEO solutions with different molecular weights. The molecular weights and the corresponding symbols are shown in the legend. The solid lines are drawn through the data points for clarity.
Page 140

Fig. A.6. Surface pressure, $\sigma_0 - \sigma$, *vs.* molecular weight of PEO for two typical bulk concentrations in regime III. The bulk concentrations and the corresponding symbols are shown in the legend.
Page 141

Fig. A.7(a). Surface pressure *vs.* surface concentration of PEO monolayers with two different molecular weights. The molecular weights and the corresponding lines are shown in the legend.

Fig. A.7(b). The change in the ellipsometric phase angle *vs.* surface concentration of PEO monolayers with two different molecular weights. The molecular weights and the corresponding symbols are shown in the legend.
Page 143

Fig. A.8. Surface pressure *vs.* surface concentration of CPC monolayers with different molecular weights. The molecular weights and the corresponding symbols are shown in the legend.
Page 144

Fig. A.9. Surface pressure *vs.* area per $C_{16}H_{33}$ end group of CPC monolayers with different molecular weights. The molecular weights and the corresponding symbols are shown in the legend. The scaled experimental data collapses reasonably well onto the single solid curve.
Page 146

Fig. A.10. The change in the ellipsometric phase angle *vs.* bulk concentration of PEO solutions with two different molecular weights. The molecular weights and the corresponding symbols are shown in the legend.
Page 148

Fig. B.1. A schematic drawing of atomic force microscopy (AFM).
Page 158

Fig. B.2. Surface pressure *vs.* surface concentration of a PEA monolayer and the related graft copolymer monolayers. The PS graft levels are shown in the plot.
Page 160

Fig. B.3. Surface pressure *vs.* the measured surface concentration after scaling by the weight ratio of the PEA backbone for PEA and its related graft copolymers. The PS graft levels are shown in the plot.
Page 161

Fig. B.4. Logarithmic plot of surface pressure *vs* the measured surface concentration (multiplied by the weight ratio of the PEA backbone) for PEA and its related graft copolymers. The PS graft levels are shown in the plot.
Page 163

Fig. B.5. The change in the ellipsometric phase angle *vs.* the measured surface concentration (multiplied by the weight ratio of the PEA backbone) for PEA and its related graft copolymers. The PS graft levels are shown in the plot.

Page 164

Fig. B.6. Power spectra of a monolayer of the graft copolymer with 28% PS at Γ = 1.0 mg/m^2 at the diffraction orders 2-4, corresponding to k = 134.68, 199.07, and 263.30 cm^{-1}. They are rescaled to have the same baseline. The solids lines are the fits using Eq. (4.4). The symbols correspond to: ● n=2; ◆ n=3; and ▲ n=4.

Page 165

Fig. B.7(a). Surface dynamic longitudinal elasticity, ε, *vs.* the measured surface concentration (multiplied by the weight ratio of the PEA backbone) for PEA and its related graft copolymers. The symbols correspond to: ● PEA; ▲ 28% PS; and ■ 47% PS. The solid lines show the static elasticity calculated using Eq. (B.7) for all samples.

Fig. B.7(b). Surface longitudinal viscosity, κ, *vs.* the measured surface concentration (multiplied by the weight ratio of the PEA backbone) for PEA and its related graft copolymers. The symbols correspond to: ● PEA; ▲ 28% PS; and ■ 47% PS.

Page 166

CHAPTER 1

INTRODUCTION

Liquid surfaces are constantly being deformed by thermal motion in the form of waves.[1] For simple liquids, these waves are typically of small amplitude ($\sim$ 10 Å) with characteristic wavelength $\sim 100\mu m$ and propagate as capillary waves also called "ripplons". The propagation of capillary waves is controlled by the surface tension and its temporal damping by the liquid viscosity.

When a beam of light is incident on the interface, the light scattered by these capillary waves will have a small frequency shift (10-100kHz) compared to the incident frequency (10^{15}Hz). These small frequency changes can be used to study dynamic and structural properties of the medium. The measurement of these small frequency shifts has been made possible by the development of the surface scattering techniques.[2,3] Furthermore, because of the small amplitude of the waves, the scattered intensity is extremely weak and is best detected by the heterodyne techniques.[2,3] The scattered light whose spectrum is to be measured is mixed with some unscattered light (which acts as a local oscillator) and detected by a photodetector.

In heterodyne surface light scattering studies, a series of wave vectors corresponding to a sequence of grating orders is selected by using a transmission diffraction grating.[4–6] The power spectrum of ripplon scattering has approximately a Lorentzian line shape with a peak frequency which is related to the ripplon propagation speed and a linewidth due to temporal ripplon damping and instrumental broadening. The frequency shift, which is approximately equal to the resonant frequency, and the full-width at half-maximum are measured. The approximate physical properties of the solution, *i.e.* the surface tension and the viscosity, are then obtained. The complete power spectrum can also be analyzed using more complete models. The major advantage of this technique of investigation is that the system under study is not disturbed.

Since the first surface light scattering experiments in 1967 on aqueous interfaces,[7,8] the surface scattering technique has been used to study surface waves on water and other monolayer-free surfaces.[4–6,9–11] The bulk viscosity in the case of simple liquids is a constant and the surface waves are the standard capillary waves. The proper bulk viscosity and surface tension of a liquid can be obtained by surface light scattering with correct instrumental calibration. Surface light scattering has also been used to study liquid crystals, the xenon vapor/liquid interface, and carbon dioxide vapor/liquid interfaces.[12] Surface light scattering has been proved to be a powerful technique in the study of ultra-low interfacial tensions of microemulsion systems where no other techniques can probe such low surface tension.[13,14]

Furthermore, numerous studies of surface waves on monolayer-covered interfaces have been reported. In the case of monolayer-covered interfaces, besides the bulk viscosity and surface tension of the liquid, several other monolayer viscoelastic parameters become important in describing capillary wave motion. There are two types of monolayers: monomolecular and polymeric monolayers. The monomolecular monolayers studied by surface light scattering are mainly fatty acids at air/water interfaces.[15–19] Polymeric monolayers at air/water interfaces have also been studied by surface light scattering.[20–23]

While simple liquid interfaces and monolayer-covered interfaces have been extensively studied, considerably less attention has been devoted to surface waves on polymer solutions. Surface hydrodynamics of polymer solutions have been studied by Harden *et al.* theoretically.[24] There have been, however, very few experimental studies of surface waves of polymer solutions.

Polymer solutions are one of the most common fluids in today's world, ranging from foods to many industrial solutions. In a very simple physical picture, polymer molecules can be viewed as long flexible chains. When such a polymer is dissolved in a simple liquid solvent at very low polymer concentration, the polymer chains are far away from each other, and the solution is not very different from the pure solvent. However, when the polymer concentration is increased enough, the polymer chains start to entangle, and the resulting solution exhibits viscoelastic properties

that are determined by the degree of polymerization and the polymer concentration. One of the most direct and interesting results due to the viscoelastic properties of polymer solutions is that several types of surface modes can exist at the air/solution interface.[24] These surface modes include Rayleigh elastic waves (resonant frequency of the surface waves $\omega_k \propto k$), capillary waves (resonant frequency $\omega_k \propto k^{3/2}$), and overdamped modes, depending on the concentrations of polymer solutions and the wave vector. By studying the surface waves on polymer solutions, we can therefore determine the surface properties as well as the bulk properties of the polymer solutions. Recent developments in the technique of surface heterodyne light scattering have made direct experimental measurements of surface waves on polymer solutions possible.

The major part of this thesis is an experimental study of surface waves of polymer solutions at the air/solution interface by the technique of surface heterodyne light scattering. The surface waves on polymer solution are very sensitive to the polymer concentration and structure near the interface. For a given polymer solution, depending on the interaction between polymers and the solvent, the polymer concentration near the interface can be different from the bulk. In principle, three different cases can occur. In the first, polymers are attracted to the interface, forming an adsorption layer with surface polymer concentration higher than that in the bulk. In the second, polymers are attracted equally to the interface and the bulk. In the third, polymers are repelled from the interface which forms a depletion layer. We have chosen three specific polymer solution systems with which to study the surface waves under each of the above conditions.

Since polymer solutions are the main systems studied in this present work, Chapter 2.1 will give a brief introduction to polymers. Also, the theoretical background of both surface fluctuations and the light scattering method will be reviewed. Chapter 2.2 introduces the principles of light beating spectroscopy while Chapter 2.3 provides a detailed analytical treatment of surface waves and the associated light scattering spectrum. Chapter 3 reviews the experimental methods which we have used to investigate surface and bulk properties of polymer solutions.

The principles developed are then applied in Chapter 4 to study surface waves at air/polymer solution interfaces. Chapter 4 will present the study of three types of polymer solutions in detail. For each type of polymer solutions, the experimental approach will be described and the results will be presented and discussed.

The appendices will present the other experiments which I did during my thesis study. Appendix A is a study of surface activity of polyethyleneoxide (PEO). Ellipsometry and static surface tension measurements were combined to examine the interfacial properties of PEO. Appendix B is a study of graft copolymer monolayers at the air/water interface. We combined measurements using a surface balance, ellipsometry, surface light scattering, and atomic force microscopy (AFM) in order to study the surface structure of graft copolymers at the air/water interface.

References

1. L. D. Landau and E. M. Lifshitz, *Fluid Mechanics* (Pergamon Press, N.Y. 1959), Ch. VII.

2. H. Z. Cummins and H. L. Swinney, *Prog. Opt.* **8**, 133 (1970).

3. B. Chu, *Laser Light Scattering* (Academic Press, N.Y. 1974), Ch. IV.

4. S. Hård, Y. Hamnerius, and O. Nilsson, *J. Appl. Phys.* **47**, 2433 (1976).

5. M. Sano, M. Kawaguchi, Y-L. Chen, R.L. Skarlupka, T. Chang, G. Zografi, and H. Yu, *Rev. Sci. Instrum.* **57**(6), 1158 (1986).

6. R.B. Dorshow, A. Hajiloo, and R.L. Swofford, *J. Appl. Phys.* **63**, 1265 (1988).

7. R.H. Katyl and U. Ingard, *Phys. Rev. Lett.* **19**, 64 (1967).

8. R.H. Katyl and U. Ingard, *Phys. Rev. Lett.* **20**, 248, (1968).

9. M. A. Bouchiat and J. Meunier, *C. R. Acad. Sc. Paris* **266b**, 301 (1969).

10. D. Langevin, *J. Chem. Soc. Faraday Trans.1* **70**, 95 (1974).

11. D. Byrne and J. C. Earnsharw, *J. Phys. D: Appl. Phys.* **12**, 1133 (1979).

12. P. A. Fleury and J. P. Boon, in *Advances in Chemical Physics* edited by I. Prigogine and S. A. Rices (John Wiley and Sons, N.Y. 1973); Vol. 24., and references therein.

13. A. Pouchelon, J. Meunier, D. Langevin and A. M. Cazabat, *J. Phys. (Paris)* **41**, 1239 (1980).

14. D. I. Jon, H. L. Rosano and H. Z. Cummins, *J. Colloid Interface Sci.* **114**, 330 (1986).

15. D. Langevin and C. J. Griesmar, *J. Phys. D: Appl. Phys.* **13**, 1189 (1980).

16. D. Langevin, *J. Colloid Interface Sci.* **80**, 412 (1981).

17. S. Hård and R. D. Neuman, *J. Colloid Interface Sci.* **83**, 315 (1981).

18. D. Byrne and J. C. Earnshaw, *J. Phys. D: Appl. Phys.* **12**, 1145 (1979).

19. Y.L. Chen, M. Kawaguchi, H. Yu, and G. Zografi, *Langmuir* **2**, 349 (1986).

20. Y.L. Chen, M. Kawaguchi, H. Yu, and G. Zografi, *Langmuir* **3**, 31 (1987).

21. B. B. Sauer, H. Yu, C. Tien and D. F. Hager, *Macromolecules* **20**, 393 (1987).

22. B. B. Sauer, M. kawaguchi, and H. Yu, *Macromolecules* **20**, 2732 (1987).

23. M. Kawaguchi, B. B. Sauer and H. Yu, *Macromolecules* **22**, 1735 (1989).

24. J. L. Harden, H. Pleiner, and P. A. Pincus, *J. Chem. Phys.* **94**, 5208 (1991).

Chapter 2

THEORETICAL BACKGROUND

2.1 Introduction to Polymers

A. Basic Concepts of Polymers

A macromolecule (or polymer) is a large molecule composed of many simple chemical units, generally called structural units or monomers. In some polymers, each structural unit is connected to precisely two other structural units, and the resulting chain structure is called a linear macromolecule. In other polymers most structural units are connected to two other units, although some structural units connect to three or more units, and we talk of branched molecules. Where the chains terminate, special units called end groups are found. Fig. 2.1 shows symbolic representations of linear and branched macromolecules. The polymers used in this thesis work are linear polymers. In the following, we only consider linear polymers.

The length of a polymer chain is specified by the number of repeat unit, N, in the chain which is called the degree of polymerization (DP). The molecular weight of the polymer is the product of the molecular weight of the monomer unit and N. One important feature of polymers is the existence of a distribution of chain lengths and therefore degrees of polymerization and molecular weights. To describe molecular weight distributions in simple quantitative terms, we introduce various molecular weight averages.[1]

If the sample contains N_i moles of the ith kind with molecular weight M_i, the number-average molecular weight is introduced by multiplying the molecular weight of each kind by its number of moles, summing and dividing by the total number of moles,

$$\bar{M}_n = \frac{\Sigma_{i=1}^{\infty} M_i N_i}{\Sigma_{i=1}^{\infty} N_i}. \tag{2.1}$$

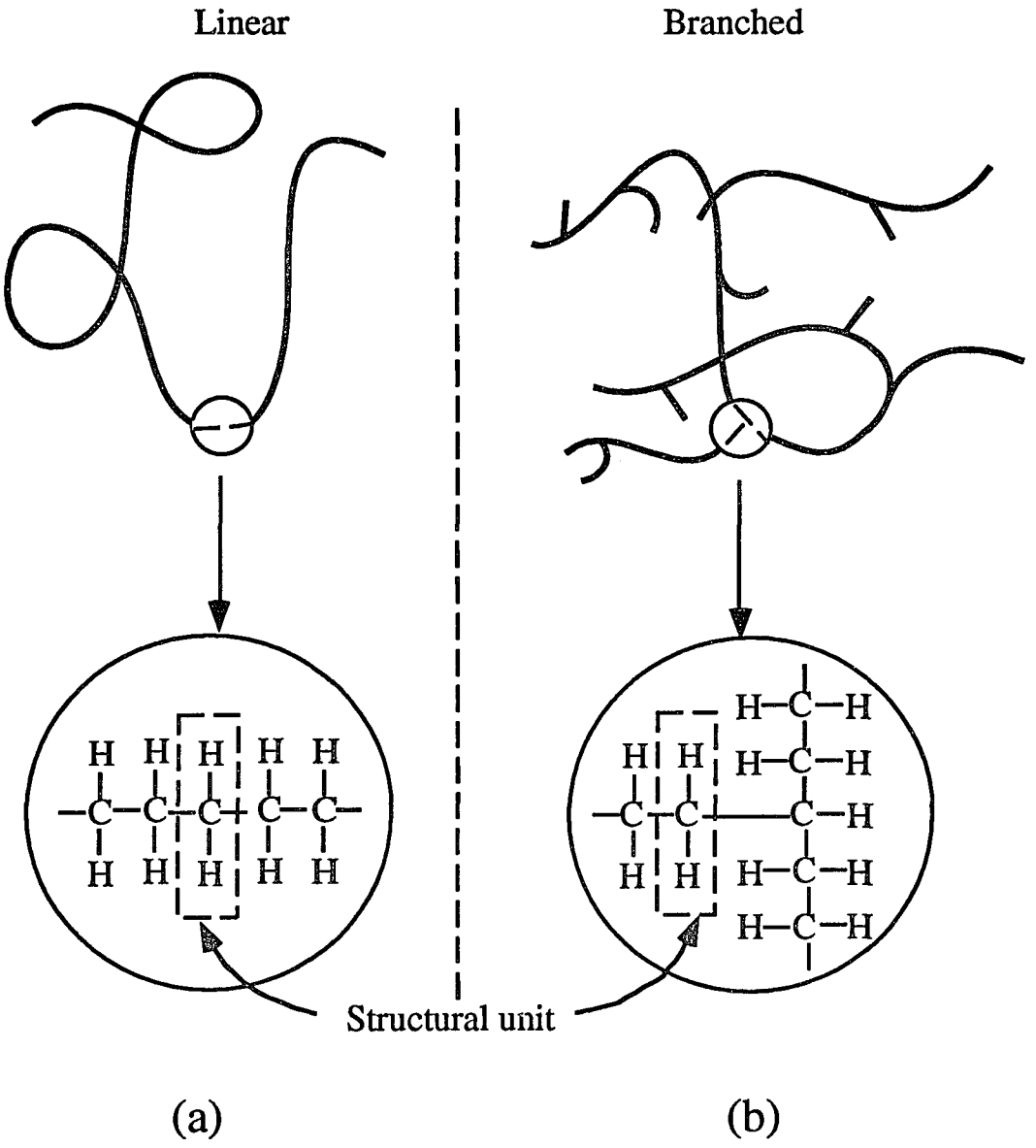

Fig. 2.1. Symbolic representations of linear and branched macromolecules (high-density polyethylene and low-density polyethylene, respectively): (a) linear, (b) branched.

Since the mass of the ith kind w_i is $w_i = N_iM_i$, we may alternatively form an average, the weight (or mass) average, by weighting the M_i with respect to the mass,

$$\bar{M}_w = \frac{\Sigma_{i=1}^{\infty} N_i M_i^2}{\Sigma_{i=1}^{\infty} NiM_i}. \tag{2.2}$$

If the quantity $\bar{M}_w/\bar{M}_n$ is in the range 1.0 to 1.2, such a polymer is called monodisperse. For large quantity $\bar{M}_w/\bar{M}_n$, the polymer is polydisperse.

B. Polymer Solutions

Most polymers of interest are flexible, meaning that rotation about the backbone bonds, if they are single bonds, is possible. Bond lengths and bond angles are fixed, but different rotational states have only small energy differences ($\Delta E \leq k_B T$).

A very simple model for a flexible polymer chain is the random walk: the chain backbone is a connected sequence of N bonds, each of length a (a= 1.53 Å for a C-C single bond), and each bond can choose any direction in space, irrespective of the directions of the other bonds.[2]

Then the end-to-end vector **r** is the sum of N "jump vector"

$$\mathbf{r} = \Sigma_{i=1}^{N} \mathbf{a}_i \tag{2.3}$$

where $\mathbf{a}_i$ is the ith bond vector. Different $\mathbf{a}_i$ vectors have completely independent orientations, which have many consequences:

(1) the average square end-to-end distance $\langle \mathbf{r}^2 \rangle$ is linear in N

$$\langle \mathbf{r}^2 \rangle = \Sigma_{nm} \langle \mathbf{a}_n \cdot \mathbf{a}_m \rangle = \Sigma_n \langle \mathbf{a}_n^2 \rangle = Na^2 = R_0^2 \tag{2.4}$$

since all cross-products vanish. Qualitatively, we can say that a random walk has a size $R_0 \sim N^{1/2}a$.

(2) the distribution function $p(\mathbf{r})$ for $\mathbf{r}$, has the Gaussian distribution

$$p(x, y, z) = constant N^{-1/2} exp(\frac{-x^2}{2\langle x^2 \rangle}) exp(\frac{-y^2}{2\langle y^2 \rangle}) exp(\frac{-z^2}{2\langle z^2 \rangle}) \cong N^{-3/2} exp(\frac{-3r^2}{2Na^2})$$

where the factor $N^{-3/2}$ arise from normalization conditions.

Light scattering experiments show that the real chain dimensions in solvent are bigger than predicted by the unrestricted random walk model. There are two major factors:

(1) Local restriction on chain conformation; these depend on the chemical microstructure of the polymer, and always act to expand the length. Bond angles are fixed, so the chain can never be modeled as a completely unrestricted random walk. Rotational states are subject to steric restrictions which will depend on side group sizes and shapes.

(2) Long range restrictions on chain conformation; these depend on the thermodynamic interaction between the solvent molecules and polymer segments. A polymer chain differs from a random walk because it cannot intersect and cross over itself. Each segment occupies some volume and no two segments can occupy the same space simultaneously. This excluded volume forces the chain into more expanded conformations. The exclude volume effect depends on the molecular interactions of polymer units and solvent molecules. It is large in good solvents, weak in poor solvents and is exactly canceled in a theta solvent.

A more precise model for real chains is called self-avoiding walk. Flory gave a simple scheme for computing the real chain length R_F.[3] The starting point is a chain, with a certain unknown radius R and an internal monomer concentration

$$c_{int} \cong \frac{N}{R^d} \tag{2.6}$$

where d is the dimension.

There is a certain repulsive energy in the chain due to monomer-monomer interaction. If c is the local concentration of monomers, the repulsive energy per cm^3 is proportional to the number of pairs present, *i.e.* to c^2. We write this energy (per unit volume) as:

$$F_{rep} = \frac{1}{2} T v(T) c^2 \tag{2.7}$$

where v has the dimension of a (d dimensional) volume and is positive. We call v the excluded volume parameter, $v = (1 - 2\chi)a^d$ where a^d is the monomer volume

and χ is an interaction parameter. For a good solvent $\chi < 1/2$ and $v > 0$.

One essential approximation is to replace the average of c^2 (inside the coil) by the square of the average

$$\langle c^2 \rangle \rightarrow \langle c \rangle^2 \sim c_{int}^2. \tag{2.8}$$

Eq. (2.8) is typical of a mean field approach: all correlations between monomers are ignored. The overall repulsive energy F_{tot}, after integration over a volume R^d, scales as:

$$F_{tot} \cong Tv(T)c_{int}^2 R^d = Tv\frac{N^2}{R^d}. \tag{2.9}$$

This tends to favor large values of R (*i.e.* to swell the chain). However if the distortion is too large, the chain entropy becomes too small, and this is unfavorable. Flory includes this through an entropic elastic energy term derived from the ideal chain result

$$F_{el} \cong T\frac{R^2}{Na^2}. \tag{2.10}$$

Eq. (2.10) is also a very strong approximation; the spring constant of a real chain is much smaller than that suggested by Eq. (2.10). Adding Eq. (2.9) and Eq. (2.10) gives

$$\frac{F}{T} \cong v\frac{N^2}{R^d} + \frac{R^2}{Na^2}. \tag{2.11}$$

Eq. (2.11) has a minimum for a well defined radius $R = R_F$. Omitting all numerical coefficients, we find

$$R_F^{d+2} \cong va^2N^3 \tag{2.12}$$

or $R_F \sim N^\nu$ with

$$\nu = \frac{3}{d+2}. \tag{2.13}$$

Usually the methods used to determinate macromolecular structure, *i.e.* osmotic pressure, static or dynamic light scattering, and viscometry, depend on measurements in solutions when the chains are well separated from one another. We need to define concentration regimes for polymer solutions. For polymer solutions in good solvents, a fundamental distinction exists between dilute polymer solutions where the coils are separate - Fig. 2.2(a) and more concentrated solutions where

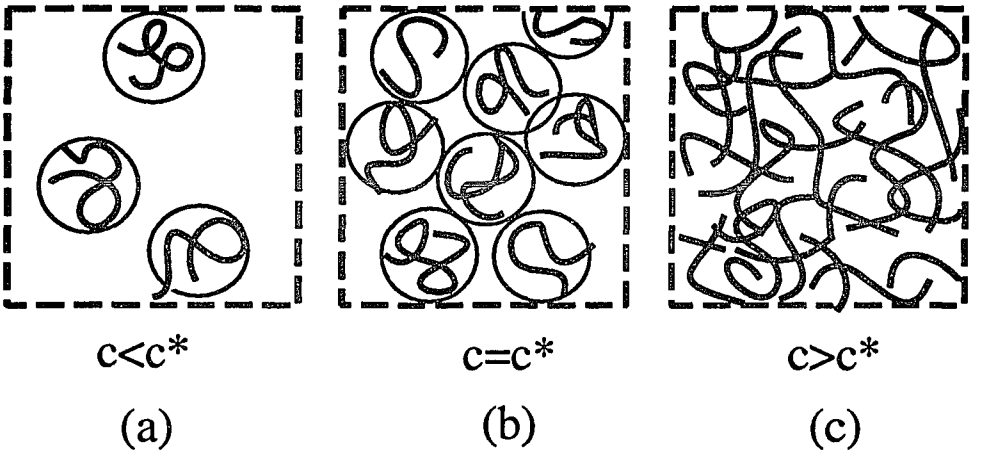

Fig. 2.2. Crossover between dilute and semi-dilute solutions: (a) dilute, (b) onset of overlap, and (c) semi-dilute.

the coils overlap - Fig. 2.2(c). At the overlap threshold - Fig. 2.2(b), where $c = c^*$, the coils begin to overlap. Clearly this threshold is not sharp; it is more properly defined as a region of crossover between regimes (a) and (c), but the scaling properties of c^* are essential. We expect c^* to be comparable to the local concentration inside a single coil. In a very good solvent, this implies:

$$c^* \cong N/R_F^3 = a^{-3}N^{1-3\nu} = a^{-3}N^{-4/5}. \tag{2.14}$$

There are three concentration regimes for polymer solutions: (1) Dilute - $c < c^*$, where the coils are separated. (2) Semi-dilute - $c > c^*$, but where the polymer concentration is still relatively small, typically up to $\sim$ 10% polymer. The coils overlap, but most of the solution is still solvent. (3) Concentrated - high concentrations, up to the polymer melt. In this regime, entanglement and free volume effects dominate the dynamics.

We can estimate c^* based on dilute solution viscosity data. First, we introduce the concept of the intrinsic viscosity $[\eta]$ which represents the capacity of a polymer to increase the viscosity of a dilute solution of polymer and solvent ($[\eta]$ increases with molecular weight). For a polymer solution system, the intrinsic viscosity is related to molecular weight by the Mark-Houwink equation:

$$[\eta] = K\bar{M}_n^a \tag{2.15}$$

where K and a are experimentally determined constants. The exponent ranges from $a \sim 0.50$ for theta solvents to a $a \sim 0.75$ for good solvents.

For a dilute solution, the viscosity can be written as:

$$\frac{\eta - \eta_s}{\eta_s c} = [\eta] + k_H[\eta]^2 c + ... \tag{2.16}$$

where η is the viscosity of the solution, η_s is the viscosity of the solvent, c is the concentration of solution and k_H is the Huggins coefficient which is dimensionless.

The intrinsic viscosity is the limiting value of η_{sp}/c at infinite dilution:

$$[\eta] = lim_{c\to 0}\frac{\eta_{sp}}{c} = lim_{c\to 0}\frac{\eta - \eta_s}{\eta_s c} \tag{2.17}$$

At a dilute concentration, polymer coils behave hydrodynamically like solid spheres of radius R. From the Einstein equation for hard spheres, we have

$$\eta = \eta_s[1 + 2.5\psi] \tag{2.18}$$

where $\psi \sim c/NR^3$ is the volume fraction occupied by the spheres. Eqs. (2.16) - (2.18) gives

$$[\eta] \cong \frac{R^3}{N} \cong \frac{R_F^3}{N}. \tag{2.19}$$

Using Eq. (2.14), we have

$$c^* \cong 1/[\eta]. \tag{2.20}$$

Eq. 2.10 gives a good estimate of c^* from dilute solution viscosity data. Viscosity measurements provide an easy way to measure the hydrodynamic size of a polymer.

In the semi-dilute regime, a quantity of interest is the correlation length, ξ, that is, the mean distance between polymer chains - Fig. 2.3. We can determine how ξ varies with concentration from scaling arguments and a few simple physical considerations. First, we expect that for $c > c^*$, the solution structure on the length scale ξ will not depend on molecular weight since we are looking only at rather small sections of the molecule. Secondly, at $c = c^*$ we expect ξ to be approximately the same as the size of the coil R_F. These requirements lead to the form

$$\xi(c) \cong R_F\left(\frac{c^*}{c}\right)^{m_\xi} \quad (c > c^*) \tag{2.21}$$

where the exponent m_ξ must be such the powers of N from $R_F(\sim N^{3/5})$ and from $c^*(\sim N^{-4/5})$ cancel. This means that $m_\xi = 3/4$

$$\xi(c) \cong ac^{-3/4}. \tag{2.22}$$

Thus, the mesh size decreases rapidly with concentration.

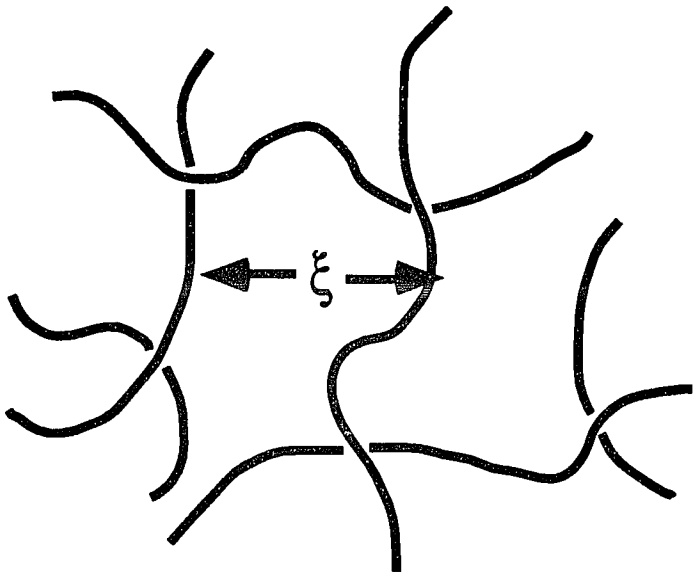

Fig. 2.3. A magnified view of a polymer solution in the semi-dilute regime.

C. Viscoelastic Properties of Polymer Solutions

For solids, the relation between force and deformation is Hooke's law; the force is proportional to the deformation

$$\sigma(t) = G\gamma \tag{2.23}$$

where $\sigma(t)$ is the force per unit area or stress and γ is the relative length change or strain. G is a constant of proportionality called the elastic modulus. It is an intrinsic property of a solid.

For simple liquids, the simplest constitutive equation is Newton's law; the stress is proportional to the rate of deformation:

$$\sigma(t) = \eta\dot{\gamma} \tag{2.24}$$

where $\dot{\gamma} = d\gamma/dt$ is the rate of strain, and η is the shear viscosity.

Polymeric materials belong to an intermediate class of materials that are termed viscoelastic. They exhibit both liquid-like (viscous) and solid-like (elastic) behavior during the response to an applied deformation. The relative proportion of viscous or elastic responses depends on the time scale of the deformation and the amount of deformation applied. When the time scale of the deformation is short, viscoelastic materials exhibit elastic response, but when deformed at a constant rate for long times the stress achieves a steady state value as in the case of viscous liquids. Linear viscoelastic behavior is obtained if the deformation is sufficiently small for all past times (infinitesimal deformation) or if it is imposed sufficiently slowly (infinitesimal rate of deformation). If both strain and rate of strain are infinitesimal, and the time-dependent stress-strain relation can be described by linear differential equations with constant coefficients, we have linear viscoelastic behavior; then in a given experiment the ratio of stress to strain is a function of time (or frequency) alone, and not of stress magnitude.

The viscoelastic properties of polymer liquids can be obtained by measuring the steady state response to a small amplitude sinusoidal deformation. For linear

viscoelastic response at steady state, the stress and strain will vary sinusoidally but the strain will lag behind the stress. The polymer is subjected to a sinusoidal shear strain at frequency:

$$\gamma(t) = \gamma^0 sin\omega t \tag{2.25}$$

where γ^0 is the strain amplitude, which is maintained sufficiently small so that the response varies linearly with strain. The shear stress is given by

$$\sigma(t) = \sigma^0 sin(\omega t + \delta) \tag{2.26}$$

where δ is the phase lag. When a viscoelastic material is subjected to small amplitude oscillatory shear flow, the shear stress $\sigma(t)$ is always sinusoidal but lags the strain with a phase lag δ which depends on the frequency ω of the oscillation. Expanding Eq. (2.26), one obtains

$$\sigma(t) = \sigma^0(sin\omega t cos\delta + cos\omega t sin\delta). \tag{2.27}$$

The stress is composed of two component: one of magnitude $\sigma^0 cos\delta$ in-phase with the strain, (G', storage modulus) and a component 90^0 out-of-phase with the strain, (G'', loss modulus), of magnitude $\sigma^0 sin\delta$. The stress may be written as

$$\sigma(t) = \gamma^0(G' sin\omega t + G'' cos\omega t) \tag{2.28}$$

where

$$G' = \sigma^0 cos\delta/\gamma^0 \quad and \quad G'' = \sigma^0 sin\delta/\gamma^0. \tag{2.29}$$

This relationship suggests a complex representation of the modulus. Expressing Eqs. (2.25) and (2.26) in exponentials:

$$\gamma(t) = \gamma^0 e^{-i\omega t} \quad \sigma(t) = \sigma^0 e^{-i(\omega t+\delta)}. \tag{2.30}$$

The complex modulus $G^*(\omega)$ may be written as[4]

$$G^*(\omega) = \frac{\sigma(t)}{\gamma(t)} = \frac{\sigma^0}{\gamma^0} e^{i\delta} \tag{2.31}$$

which yields:

$$G^*(\omega) = \frac{\sigma^0}{\gamma^0}(cos\delta + isin\delta). \tag{2.32}$$

Substituting the relationship for G' and G'' from Eq. (2.29) yields

$$G^*(\omega) = G' + iG'' \tag{2.33}$$

The components of the complex modulus $G'(\omega)$ and $G''(\omega)$ in small sinusoidal deformations are related to the stress relaxation modulus, $G(t)$:

$$G'(\omega) = \omega \int_0^\infty G(t) sin\omega t dt \tag{2.34}$$

$$G''(\omega) = \omega \int_0^\infty G(t) cos\omega t dt. \tag{2.35}$$

It is also convenient to define a complex viscosity $\eta^* = \eta' - i\eta''$ by

$$\eta^* = \frac{G^*}{i\omega}. \tag{2.36}$$

It follows that

$$\eta' = \frac{G''}{\omega} \quad and \quad \eta'' = \frac{G'}{\omega}. \tag{2.37}$$

The simple Maxwell model can be used to describe the viscoelastic behavior of entangled polymer chains:[4]

$$G^* = \frac{iG_0\omega\tau}{(1 + i\omega\tau)} \tag{2.38}$$

where G_0 is the transient modulus of the polymer network, and τ is the relaxation time of the medium. For $\omega \gg \tau^{-1}$, polymer solutions will behave as an elastic medium with modulus given by the transient modulus G_0. For $\omega \ll \tau^{-1}$, polymer solutions will flow like a viscous fluid of viscosity $\eta \sim G_0\tau$.

2.2 Theory of Light Beating Spectroscopy

Optical mixing or light beating spectroscopy enables us to study many phenomena which were previously inaccessible by other techniques. This high resolution

spectroscopy is well suited to the study of quasi-elastic light scattering from random thermal fluctuations. The theory and applications of the technique are well documented.[5–9]

There are two experimental approaches: heterodyne and homodyne spectroscopy. In heterodyne spectroscopy, the scattered light and a portion of the incident light (the local oscillator) beat at the photo detector to yield the Doppler frequency. This technique can be used to study weakly scattering systems. In homodyne spectroscopy, the scattered light beats with itself and a frequency shift cannot be measured. The homodyne approach is generally used for relatively strong scattering systems. This section will give a brief outline of light beating spectroscopy with respect to surface light scattering and dynamic light scattering.

2.2.1 Heterodyne Detection

Since the photomultiplier tube is a square-law detector, its instantaneous current output, $i(t)$, is proportional to the square of the incident electric field

$$i(t) \propto |E(t)|^2. \tag{2.39}$$

The current autocorrelation function is defined by

$$\langle i(0)i(t)\rangle = lim_{T\to\infty}\frac{1}{T}\int_0^T dt' i(t')i(t'+t). \tag{2.40}$$

When t is very small compared to times typifying the fluctuations in i, $i(t'+t)$ will be very close to $i(t')$, so $\langle i(0)i(t)\rangle \approx \langle i^2\rangle$. As t increases, the deviation of $i(t'+t)$ from $i(t')$ is more likely to be nonzero, for $t \to \infty$, all correlation is lost and $\langle i(0)i(t)\rangle \to \langle i\rangle^2$. Thus, we can say $i(t'+t)$ is correlated with $i(t')$ when t is small.

Using Eq. (2.39) and Eq. (2.40), the time correlation function is

$$\langle i(0)i(t)\rangle = B\langle |E(0)|^2 |E(t)|^2\rangle \tag{2.41}$$

where B is a proportionality constant.

In the frequency domain, the spectral density (or power spectrum) $P_i(\omega)$ of a time correlation function $\langle i(0)i(t)\rangle$ is defined by the Wiener-Khinchine theorem

$$P_i(\omega) \equiv \frac{1}{2\pi}\int_{-\infty}^{+\infty} e^{-i\omega t}\langle i(0)i(t)\rangle dt. \tag{2.42}$$

$\langle i(0)i(t)\rangle$ and $P_i(\omega)$ are Fourier transforms of one another and an experimental determination of one as a function of its argument is sufficient for the determination of the other. $P_i(\omega)$ is often measured in surface light scattering experiments.

In the heterodyne method, a small portion of the unscattered light acts as a local oscillator and is mixed with the scattered light on the photomultiplier cathode. Let the field under study be $E_s(t)$ and the local oscillator field be $E_{LO}(t) = E^0_{LO}exp(-i\omega_{LO}t)$. Then the electric field at the PMT is the sum of $E_{LO}(t)$ and $E_s(t)$. This gives for the autocorrelation function:

$$\langle i(0)i(t)\rangle = B\langle|E_{LO}(0) + E_s(0)|^2|E_{LO}(t) + E_s(t)|^2\rangle. \tag{2.43}$$

By proper choice of the experimental conditions, the amplitude of the local oscillator is much greater than the amplitude of the scattered field

$$|E_{LO}(t)| \gg |E_s(t)|. \tag{2.44}$$

By neglecting the small term I_s^2, the current autocorrelation function can be simplified to

$$\langle i(0)i(t)\rangle = B[I^2_{LO} + I_{LO}\langle I_s\rangle\{[exp(i\omega_{LO}t)]g_s^{(1)}(t) + [exp(-i\omega_{LO}t)]g_s^{(1)*}(t)\}] \tag{2.45}$$

where $I_{LO} = \langle|E_{LO}|^2\rangle$, $\langle I_s\rangle = \langle|E_s|\rangle^2$, $g_s^{(1)}(t) = \langle E_s^*(0)E_s(t)\rangle/\langle I_s\rangle$ and $\langle|E_s(0)|^2|E_s(t)|^2\rangle$ is neglected.

The power spectrum produced by the combined signal and local oscillator field is found from Eq. (2.42) and Eq. (2.45):

$$P_i(\omega) = B\{I^2_{LO}\delta(\omega) + \frac{I_{LO}\langle I_s\rangle}{2\pi}\int_{-\infty}^{\infty} e^{i\omega t}\{[exp(i\omega_{LO}t)]g_s^{(1)}(t) + [exp(-i\omega_{LO}t)]g_s^{(1)*}(t)\}dt\}. \tag{2.46}$$

Characteristically, $g_s^{(1)}(t) = [exp(-i\omega_0 t)][exp(-t/\tau)]$ for a random Gaussian system with a single relaxing species, then

$$P_i(\omega) = B\{I_{LO}^2\delta(\omega) + \frac{2I_{LO}\langle I_s\rangle/\tau\pi}{(\omega - |\omega_0 - \omega_{LO}|)^2 + (\frac{1}{\tau})^2}\}. \tag{2.47}$$

The power spectrum is described by a Lorentzian centered at frequency $|\omega_0 - \omega_{LO}|$. The measurement of a frequency shift is one major advantage of the heterodyne detection technique. Heterodyne spectroscopy has been used to detect the power spectrum of the thermal fluctuations at an air/liquid interface.

2.2.2 Homodyne Detection

Since in the homodyne method only the scattered light impinges on the photocathode, $E(t)$ in Eq. (2.39) is equal to the scattered field $E_s(t)$. We have

$$\langle i(0)i(t)\rangle = \langle |E_s(0)|^2 |E_s(t)|^2\rangle. \tag{2.48}$$

Eq. (2.48) is sometimes referred to as the homodyne correlation function. If the scattered field is a Gaussian random process, then the correlation function can be expressed as

$$\langle i(0)i(t)\rangle = |\langle E_s(0)^* E_s(0)\rangle|^2 + |\langle E_s(0)^* E_s(t)\rangle|^2. \tag{2.49}$$

Notice that the second term is the square of the heterodyne correlation function $g_s^{(1)}(t)$. For dynamics described by a single relaxing species the normalized heterodyne correlation function decays exponentially, $g_s^{(1)}(t) = [exp(-i\omega_0 t)][exp(-t/\tau)]$. We then have for the normalized homodyne correlation function $g_s^{(2)}(t)$,

$$g_s^{(2)}(t) = \langle i(0)i(t)\rangle/\langle i\rangle^2 = 1 + exp(-2t/\tau). \tag{2.50}$$

If the relaxation is a diffusional process, then τ is related to the diffusion constant D by

$$\frac{1}{\tau} = Dk^2 \tag{2.51}$$

where k is the wave vector.

The power spectrum of the photocurrent from the PMT in a homodyne experiment is the Fourier transform of $g_s^{(2)}(t)$:

$$P_i(\omega) = \delta(\omega) + \frac{2/\tau\pi}{\omega + (\frac{2}{\tau})^2}. \tag{2.52}$$

2.3 Surface Waves on Liquid Interfaces

The liquid surface is not a perfectly plane. As a result of random thermal disturbances, it becomes deformed and shifts from the equilibrium state. For long waves ($k < 3cm^{-1}$), the dominant restoring force is gravitational and the surface fluctuations are gravity waves. For short waves ($k > 3cm^{-1}$), surface tension plays the major role in wave propagation and the surface fluctuations are capillary waves. Since the wave vector of surface light scattering is typically $100 - 1000cm^{-1}$, the gravitation force will be ignored in deriving the dispersion equation for surface waves in this chapter.

Surface waves on a simple liquid interface or a monolayer-covered interface are capillary waves. The dispersion equation for capillary wave motion can be derived by hydrodynamic theory with proper boundary conditions.[10–17] The general dispersion equation for a monolayer-covered liquid/liquid interface will be derived in Chapter 2.31. The dispersion equations at other interfaces such as monolayer-free liquid interfaces and monolayer-covered air/liquid interfaces are derived from this general dispersion equation at liquid/liquid interface by setting the appropriate parameters equal to zero. Chapter 2.32 will give a brief description of the power spectrum of monolayer-covered air/liquid interfaces.

Because of the viscoelastic properties of polymer solutions, it has been shown theoretically that several types of surface modes can exist.[18] These surface modes include Rayleigh elastic waves (resonant frequency of the surface waves $\omega_k \propto k$), capillary waves (resonant frequency $\omega_k \propto k^{3/2}$), and overdamped modes depending on the concentrations of polymer solutions and wave vectors. The derivation of the dispersion equation for the air/solution interface will be presented in Chapter 2.33.

For the case of very low concentration polymer solutions, the capillary dispersion equation for the air/liquid interface can be recovered from this dispersion equation.

Chapter 2.34 will treat the theoretical power spectrum of surface waves on concentrated polymer solutions. The predicted surface mode power spectrum was used to fit the experimental power spectrum of polymer solutions in this thesis. By setting the appropriate parameters equal to zero, the theoretical power spectrum can be reduced to describe an air/simple liquid interface. This reduced power spectrum was use for calibration of the surface light scattering instrument at the air/solvent interface in this thesis.

2.31 Dispersion Equation for Capillary Waves

The presence of a surface-active film produces surface forces which change the wave motion compared with that of a free surface. These forces change the boundary conditions at the free surface. The changes in the boundary conditions lead, in turn, to a change in the velocity distribution in the fluid which produces the effect of the surface active film on the wave motion. The dispersion equation for capillary wave motion for a monolayer-covered interface has been derived by many workers.[10–17] The treatments are essentially the same in their basic assumptions. We follow the strategy of Kramer[15] in the derivation of the dispersion equation for a monolayer-covered liquid/liquid interface. Our presentation will also make extensive use of the formalism of Bouchiat and Meunier.[30]

A. Properties of Monolayers

Insoluble monolayers fall into two general classes. The first, and by far the most extensively studied, consists of simple, nonpolymeric substances which are substantially insoluble, but whose molecules have sufficient attraction for the subphase to permit them to spread and disperse at the surface. The second class consists of a wide range of polymeric materials, which are positively adsorbed at the liquid/air

interface.

Materials which form monolayers are those which have a molecular structure composed of a large nonpolar or hydrophobic portion, the hydrocarbon chain, and at the end a polar or hydrophilic function group, such as -COOH or -OH. The balance between these two groups determines whether a molecule will form an insoluble monolayer, *i.e.* if the hydrophobic group is much smaller than the hydrophilic group, the material will be miscible with water.

In studies of insoluble monolayers on liquid surfaces, what we are interested in, and able to measure is the difference in surface tension between a clean or pure liquid surface and one covered with such films. The surface pressure, π, is defined as the reduction of the pure liquid-surface tension by the film,

$$\pi \equiv \sigma_0 - \sigma(\Gamma) \tag{2.53}$$

where σ_0 is the surface tension of pure liquid and $\sigma(\Gamma)$ is the surface tension of the film-covered surface at a surface concentration Γ. By taking the derivative of the π-Γ isotherm, a quantity known as the static surface dilational elasticity is determined and is calculated using[19]

$$\varepsilon_s = \Gamma \frac{\delta \pi}{\delta \Gamma}. \tag{2.54}$$

In the case of nonpolymeric substances, molecules in monolayers can exist in different states, roughly analogous to three dimensional solid, liquids, and gases. The gaseous state of monolayers is the simplest. The molecules in such films float about in the surface layer far enough apart so that they exert relatively little force on one another - Fig. 2.4(a). Such monolayers are characterized experimentally by a surface pressure which approaches zero asymptotically, as the area available to the film is increased. the surface viscosity of gaseous monolayers is also very low. In principle, any monolayer-forming substance will exist as a gaseous film if the molecules are sufficiently widely separated. The surface vapor pressure for many substances, however, are extremely low ($< 0.1 dyne/cm$) at room temperature, and the investigation of the gaseous state for such materials is experimentally very difficult.

At the opposite extreme from gaseous monolayers, in which the isolated molecules are far apart, are the condensed films in which the molecules are arranged in nearly their closest possible packing. This type of film can be thought of as much like a two-dimensional crystal. The molecules stand nearly upright with their terminal polar groups in the water and their long chains closely packed - Fig. 2.4(c). The pressure-area plots are nearly straight and very steep, indicating low compressibility in the condensed monolayers. This reflects the presence of strong chain-chain interaction which holds the molecules in their closest-packed arrangement, with little dependence on surface pressure. Condensed films often exhibit considerable surface viscosity.

Intermediate in molecular area between gaseous and condensed films of simple molecules are the expanded monolayers - Fig. 2.4(b). The pressure-area diagrams of these films show considerable curvature, although they approach the $\pi = 0$ axis at a fairly steep angle, rather than asymptotically as in the case of gaseous monolayers. The films are coherent down to low surface pressure, with little tendency for the film-forming molecules to become widely separated on the surface. The hydrophobic portions of the molecules in an expanded film are in a random orientation only, the polar groups are constrained to be in contact with the subphase. The surface viscosity is low, compared to that of the expanded state.

For monolayers of polymers, the pressure-area diagrams are rather featureless by comparison with the variety of curves which have been obtained for monolayers of small molecules. In general, the polymer monolayers can be divided into "condensed" and "expanded" classes.[20] Monolayers of expanded type are fluid and exhibit a gradual rise in surface pressure on compression and a well-defined and complete collapse. The "condensed" polymer films are perhaps best identified by their high viscosity or rigidity, together with a much steeper pressure-area curve. In analogy with the scaling theory in three dimensions, the scaling behavior for surface isotherms can also be predicted and will be presented in Appendix B.

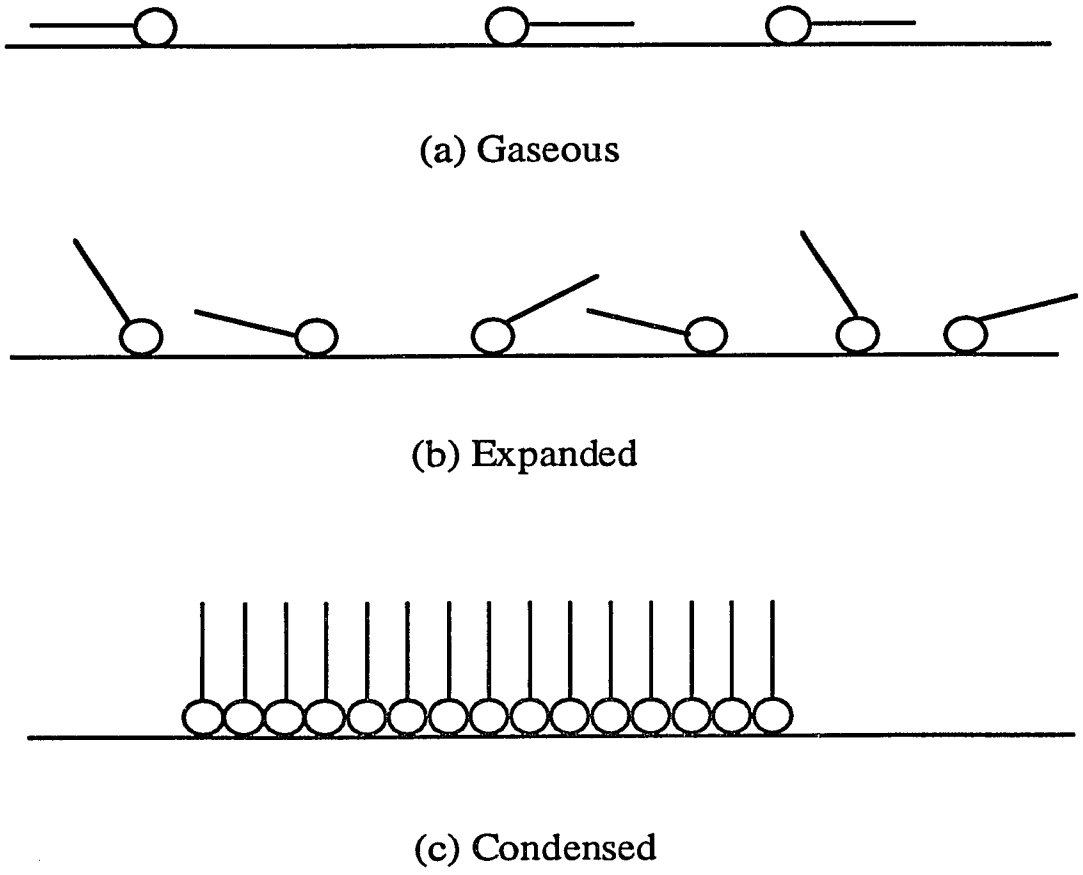

Fig. 2.4. Insoluble monomolecular monolayers at an air/water interface.

B. Definition of Rheological Parameters

Surface phases frequently display a viscoelastic behavior as many materials do in the bulk. For two-dimensional monolayers, their viscoelastic properties are different than those in a homogeneous bulk state. Due to the axial symmetry of monolayers, there are three moduli which are illustrated with the corresponding dynamic modes in Fig. 2.5 after Goodrich as[12]

(1) the transverse modulus σ^*,

(2) the compressional modulus ε^*,

(3) the shear modulus S^*.

The cylinder in this figure represents a cross section of the monolayer with the thickness of the monolayer given by the height of the cylinder. Those complex moduli are analogous to the layer bending modulus, the compressional modulus, and shear modulus of a three-dimensional smectic A liquid crystal phase.

The motions normal to the interface in Fig. 2.5 are the transverse elasticity known as the surface tension, σ, and the transverse viscosity, μ. In practice, these two viscoelastic constants is described by Eq. (2.55) which defines the complex surface tension σ^*.

$$\sigma^* = \sigma - i\omega\mu. \tag{2.55}$$

Two other elastic moduli are the surface dilational and the surface shear moduli in the longitudinal direction. Both of these are allowed to become complex to account for viscous contributions.

$$\varepsilon^* = \varepsilon - i\omega\kappa \tag{2.56}$$

$$S^* = S - i\omega S' \tag{2.57}$$

where ε is the surface compressional elasticity, κ is the surface dilational viscosity, S is the surface shear elasticity, and S' is the surface shear viscosity. The motions at the interface leading to these longitudinal viscoelastic parameters are illustrated in Fig. 2.5 (b) and (c). It is evident that both ε and κ are elastic and viscous measures of the surface against change in surface area, hence the term dilational (or

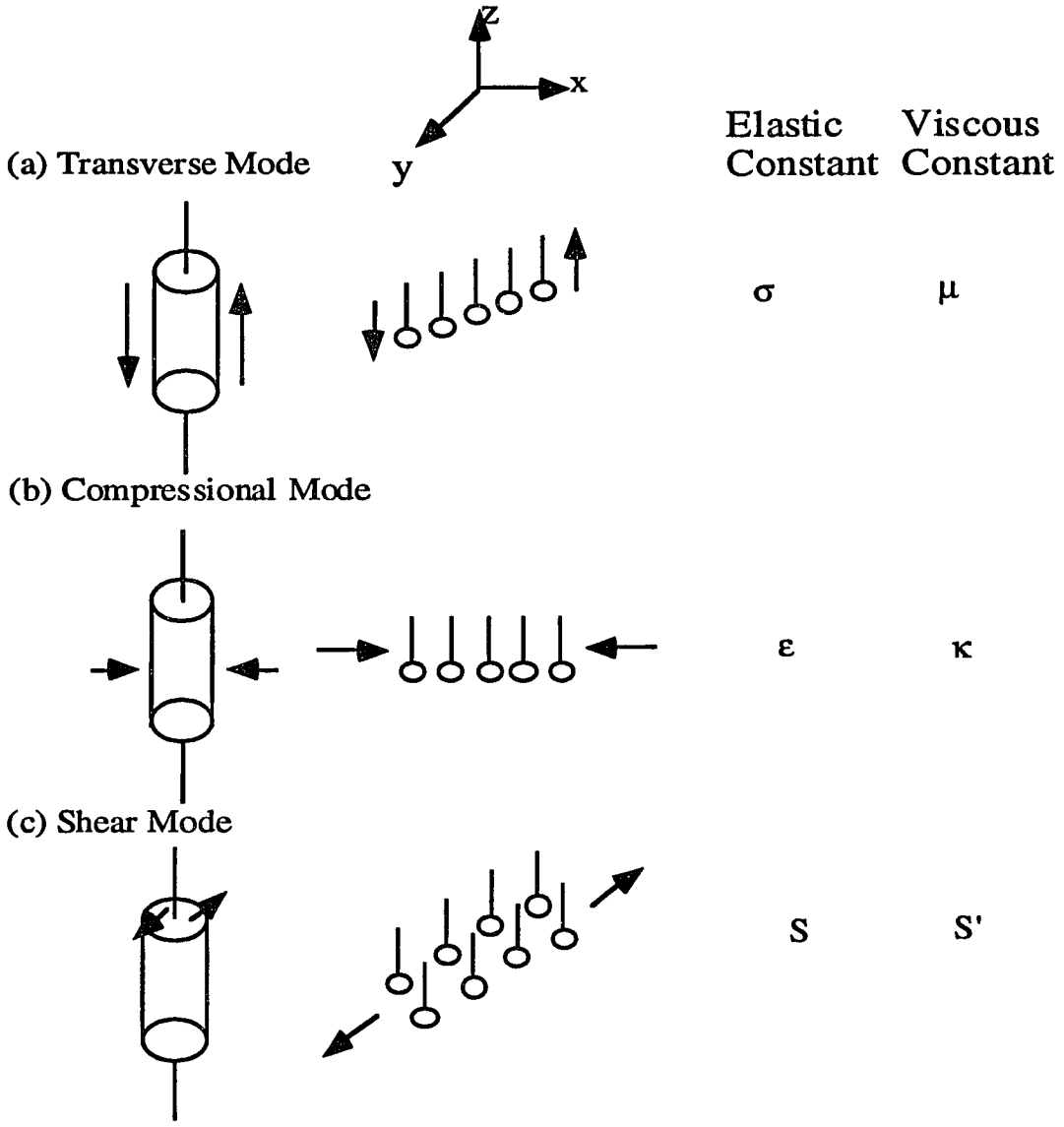

Fig.2.5. Possible motions at the interfacial plane. The interface is in the x-y plane and the cylinders represent cross sections of the monolayer.

compressional). The shear viscoelastic constants S and S' describe the resistance against changes in shape of a surface element. Experimentally, surface light scattering cannot separate ε and S or κ and S'. The static surface dilational elasticity, ε_S, from Eq. (2.54) can be used to compare with its dynamic analog which is a sum of ε and S.

C. Linear Stress-Strain Relation for Viscoelastic Interfaces

The perturbations at interfaces are thermal fluctuations or small external perturbations, with $\mathbf{k} \ll d^{-1}$ and $\mathbf{k} \ll a^{-1}$, where $\mathbf{k}$ is the scattering wave vector, d is the monolayer thickness, and a is the dimension of its largest structural units in the x-y plane. The monolayer is treated as a thin homogeneous anisotropic interface separating two isotropic fluids. The equilibrium monolayer in the x-y plane is assumed to have hexagonal symmetry or to be isotropic in the x-y plane. In analogy with the mechanics of the three-dimensional hexagonal crystal system, the elastic free energy has the form[21]

$$\begin{aligned} F =& \frac{1}{2}\lambda_1(u_{xx}^2 + u_{yy}^2) + \frac{1}{2}\lambda_2 u_{zz}^2 + \lambda_3 u_{xx}u_{yy} + \\ & \lambda_4(u_{xx} + u_{yy})u_{zz} + (\lambda_1 - \lambda_3)u_{xy}^2 + 2\lambda_5(u_{xz}^2 + u_{yz}^2) \end{aligned} \tag{2.58}$$

where $u_{ij} = 1/2(\partial u_i/\partial x_j + \partial u_j/\partial x_i)$ is the symmetric strain conjugate to the stress $\partial F/\partial(\partial u_i/\partial x_j)$ and $\mathbf{u}$ is the displacement field. Assuming the monolayer thickness, d, is small compared to the ripple wavelength, all z dependence may be neglected and the free energy of the monolayer per unit area has the form

$$F = \frac{1}{2}\varepsilon^*(u_{xx} + u_{yy})^2 + 2S^*(u_{xy}^2 - u_{xx}u_{yy}) + \frac{1}{2}\sigma^*[(\partial u_z/\partial x)^2 + (\partial u_z/\partial y)^2] \tag{2.59}$$

where the quantities $\varepsilon^* = \lambda_1 d$, and $S^* = \frac{1}{2}(\lambda_1 - \lambda_2)d$ are, respectively, the compression and shear modulus and $\sigma^* = \lambda_5 d$ is the transverse modulus. The reversible stress tensor T_{ij} of the monolayer is given by

$$T_{ij} = \begin{pmatrix} (\varepsilon^* + S^*)(u_{xx} + u_{yy}) - 2S^* u_{yy} & 2S^* u_{xy} & 0 \\ 2S^* u_{xy} & (\varepsilon^* + S^*)(u_{xx} + u_{yy}) - 2S^* u_{xx} & 0 \\ \sigma^*(\partial u_z/\partial x) & \sigma^*(\partial u_z/\partial y) & 0 \end{pmatrix} \tag{2.60}$$

The velocity of the fluids adjacent to the monolayer is defined by

$$\mathbf{v}(x,y,u_z) = \frac{\partial \mathbf{u}(x,y)}{\partial t} \tag{2.61}$$

The pressure exerted on the monolayer is given by

$$P_i(x,y,u_z) = \frac{\partial T_{ij}(x,y)}{\partial x_j} \tag{2.62}$$

(sum over repeated indices). In the linear approximation, u_z is set to zero on the left-hand sides of Eq. (2.61). and the area element belonging to P_i is taken to lie in the x-y plane. P_i can be calculated using Eq. (2.60), Eq. (2.61) and Eq. (2.62) and taking the Fourier transform defined by

$$\mathbf{u}(x,y,t) = \int_{-\infty}^{+\infty} \frac{d^2k}{(2\pi)^2} \int_{-\infty}^{+\infty} \frac{d\omega}{2\pi} exp(i\mathbf{k}\cdot\mathbf{r} - i\omega t)\mathbf{u}(\mathbf{k},\omega) \tag{2.63}$$

where $\mathbf{k} = (k_x, k_y, 0)$ and $\mathbf{r} = (x, y, 0)$. The Fourier transformed pressures become

$$P_x(\mathbf{k},\omega) = -(1/i\omega)[(\varepsilon^*)\mathbf{k}\cdot\mathbf{v}k_x + S^*k^2v_x] \tag{2.64}$$

$$P_y(\mathbf{k},\omega) = -(1/i\omega)[(\varepsilon^*)\mathbf{k}\cdot\mathbf{v}k_y + S^*k^2v_y] \tag{2.65}$$

$$P_z(\mathbf{k},\omega) = -(1/i\omega)\sigma^*k^2v_z. \tag{2.66}$$

D. The Hydrodynamic Equations

Let the density and viscosity of the fluid in the half space $z > 0$ be, respectively, ρ_1 and η_1. Taking the fluids to be incompressible, the linearized hydrodynamic equations are

$$\rho_\nu(\partial v_i/\partial t) = (\partial/\partial x_j)\sigma_{ij}^{(\nu)} \tag{2.67}$$

$$\nabla\cdot\mathbf{v} = 0 \tag{2.68}$$

and the hydrodynamic stress tensor is given by

$$\sigma_{ij}^{(\nu)} = \eta_\nu[(\partial v_i/\partial x_j) + (\partial v_j/\partial x_i)] - p\delta_{ij} \tag{2.69}$$

where $\nu = 1$ corresponds to $z > 0$, $\nu = 2$ to $z < 0$, and p is the pressure of the fluid. Inserting Eq. (2.67) and Eq. (2.69) into Eq. (2.68) gives the Navier-Stokes equation in the usual form

$$\rho_\nu(\partial \mathbf{v}/\partial t) = \eta_\nu \nabla^2 \mathbf{v} - \nabla p. \tag{2.70}$$

Taking the Fourier transform of Eq. (2.70) using Eq. (2.63) gives for the three orthogonal components of v:

$$[-i\omega\rho_\nu + \eta_\nu(k^2 - \partial^2/\partial z^2)]v_\perp = 0 \tag{2.71}$$

$$[-i\omega\rho_\nu + \eta_\nu(k^2 - \partial^2/\partial z^2)]v_z = -\partial p/\partial z \tag{2.72}$$

$$[-i\omega\rho_\nu + \eta_\nu(k^2 - \partial^2/\partial z^2)]v_\parallel = -ikp \tag{2.73}$$

where

$$v_\perp = (\hat{z} \times \hat{k})\cdot\mathbf{v}, \quad v_z = \hat{z}\cdot\mathbf{v}, \quad v_\parallel = \hat{k}\cdot\mathbf{v}. \tag{2.74}$$

The equation of continuity Eq. (2.68) can now be written as

$$ikv_\parallel + (\partial v_z/\partial z) = 0. \tag{2.75}$$

Combining Eq. (2.72), Eq. (2.73) and Eq. (2.75) gives the simple equation for the pressure

$$\partial^2 p/\partial z^2 = k^2 p. \tag{2.76}$$

E. The boundary Conditions

In the geometry considered here, all quantities must vanish for $z \to \pm\infty$ and have to be regular except at the interface where $u_z \approx 0$. The general solutions of Eq. (2.71)-Eq. (2.76) satisfying these conditions are

$$\begin{aligned} v_\perp = & C_1(\mathbf{k},\omega)exp(-m_1 z), \quad z > 0 \\ & C_1(\mathbf{k},\omega)exp(m_2 z), \quad z < 0 \end{aligned} \tag{2.77}$$

$$\begin{aligned} p &= -(i\omega\rho_1/k)A_1(\mathbf{k},\omega)exp(-kz), \quad z > 0 \\ p &= (i\omega\rho_2/k)A_2(\mathbf{k},\omega)exp(kz), \quad z < 0 \end{aligned} \tag{2.78}$$

$$v_z = A_1(\mathbf{k},\omega)exp(-kz) + B_1(\mathbf{k},\omega)exp(-m_1 z), \quad z > 0$$
$$v_z = A_2(\mathbf{k},\omega)exp(kz) + B_2(\mathbf{k},\omega)exp(m_2 z), \quad z < 0 \tag{2.79}$$

where

$$m_\nu = [k^2 - (i\omega\rho_\nu/\eta_\nu)]^{1/2}, \quad Re(m_\nu) > 0. \tag{2.80}$$

At $z = 0$, the boundary conditions require that $\mathbf{v}$ be continuous and that the discontinuity in the hydrodynamic stress be equal to the force exerted by the monolayer

$$\sigma_{iz}^{(1)}(z = +0) - \sigma_{iz}^{(2)} = P_i. \tag{2.81}$$

Using Eqs. (2.64)-(2.66), (2.75) and (2.69) gives

$$v_\perp|_{z=-0}^{z=+0} = \partial v_z/\partial z|_{z=-0}^{z=+0} = v_z|_{z=-0}^{z=+0} = 0 \tag{2.82}$$

$$\eta_1(\partial v_\perp/\partial z)(z = +0) - \eta_2(\partial v_\perp/\partial z)(z = -0) = -(S^*/i\omega)k^2 v_\perp(z = 0) \tag{2.83}$$

$$(\eta_1 - \eta_2)(\partial v_z/\partial z)(z = 0) - p|_{z=-0}^{z=+0} = -(\sigma^*/i\omega)k^2 v_z(z = 0) \tag{2.84}$$

$$\eta_1[k^2 + (\partial^2 v_z/\partial z^2)]v_z(z = +0) - \eta_2[k^2 + (\partial^2 v_z/\partial z^2)]v_z(z = -0) = $$
$$- [(\varepsilon^* + S^*)/i\omega]k^2(\partial v_z/\partial z)(z = 0). \tag{2.85}$$

F. The General Dispersion Equation at a Monolayer-Covered Liquid/liquid Interface

Combining Eqs. (2.77), (2.79) with Eq. (2.83) gives

$$C_1 = C_2 = C \tag{2.86}$$

$$A_1 + (m_1/k)B_1 = -[A_2 + (m_2/k)B_2] = D \tag{2.87}$$

$$A_1 + B_1 = A_2 + B_2 = E. \tag{2.88}$$

The other conditions lead to

$$\{i\omega - [S^* k^2/(\eta_1 m_1 + \eta_2 m_2)]\}C = 0 \tag{2.89}$$

$$[\eta_1(k+m_1)+\eta_2(k+m_2)-(\varepsilon^*+S^*)(k^2/i\omega)]D+$$
$$[\eta_1(k-m_1)-\eta_2(k-m_2)]E=0 \tag{2.90}$$

$$[\eta_1(k-m_1)-\eta_2(k-m_2)]D+[\eta_1 m_1(k+M_1)/k+$$
$$\eta_2 m_2(k+m_2)/k-(\sigma^*)(k^2/i\omega)]E=0. \tag{2.91}$$

By eliminating the ratio of D/E from Eqs. (2.90) and (2.91), the general dispersion equation for a monolayer covered liquid/liquid interface is obtained

$$0=[\eta_1(k+m_1)+\eta_2(k+m_2)-(\varepsilon^*+S^*)(k^2/i\omega)][\eta_1 m_1(k+m_1)/k+$$
$$\eta_2 m_2(k+m_2)/k-(\sigma^*)(k^2/i\omega)]-[\eta_1(k-m_1)-\eta_1(k-m_2)]^2 \tag{2.92}$$

where m_ν is given by Eq. (2.80).

Experimentally, since surface light scattering cannot separate ε^* and S^* because of the coupling between the longitudinal motions and the transverse motions , we may reset this dispersion equation as $\varepsilon^*=\varepsilon^*+S^*$.

By setting the appropriate parameters equal to zero, Eq. (2.92) can be reduced to describe monolayer-free surfaces, interfaces and monolayer-covered air/liquid interfaces.

G. Dispersion Equations at Other Interfaces

At a monolayer-free interface, the longitudinal modulus $\varepsilon^*=S^*=0$ and the transverse viscosity $\mu=0$, that $\sigma^*=\sigma$. In this case, the surface wave motion is completely determined by the bulk liquid viscosity and density along with the interfacial tension. By setting $\varepsilon^*=S^*=0$ and $\sigma^*=\sigma$, Eq. (2.92) reduces to

$$0=[\eta_1(k+m_1)+\eta_2(k+m_2)][\eta_1 m_1(k+m_1)/k+$$
$$\eta_2 m_2(k+m_2)/k-(\sigma)(k^2/i\omega)]-[\eta_1(k-m_1)-\eta_1(k-m_2)]^2. \tag{2.93}$$

By rearranging Eq. (2.93), one can prove that Eq. (2.93) is equivalent to the dispersion equation given by Herpin and Meunier.[22] The special case in Eq. (2.93)

is the monolayer-free surface, where $\rho_1 = 0$ and $\eta_1 = 0$ for air, we have the dispersion equation

$$D(s) = Y + (1+s)^2 - \sqrt{1+2s} = 0 \tag{2.94}$$

where $s = i\omega\rho_2/2\eta_2 k^2$, $Y = \sigma\rho_2/4\eta_2{}^2 k$. The dispersion equation, Eq. (2.94), is also derived by Levich[10] and used by many researchers for the simple air/liquid interface.[23–27] If the dimensionless quantity $y > 0.145$, corresponding to a low viscosity fluid, then Eq. (2.94) can be solved to the first order to give:

$$\omega_k = 2\pi f_k = \left(\frac{\sigma k^3}{\rho}\right)^{1/2} \tag{2.95}$$

i.e. the surface wave is the standard capillary wave. The power spectrum in this case has the Lorentzian profile which peaks at ω_k, with full-width at half-maximum of:

$$\nabla f_{s,c} = \frac{2\eta k^2}{\pi\rho}. \tag{2.96}$$

For a monolayer-covered air/liquid interface, taking $\rho_1 = 0$ and $\eta_1 = 0$ and defining $\varepsilon^* = \varepsilon^* + S^*$, Eq. (2.92) reduces to

$$0 = [\eta_2(k+m_2) - (\varepsilon^*)(k^2/i\omega)][\eta_2 m_2(k+m_2)/k - (\sigma^*)(k^2/i\omega)] - [\eta_1(k-m_2)]^2 \tag{2.97}$$

where $m_2 = [k^2 - (i\omega\rho_2/\eta_2)]^{1/2}$. This form of the dispersion equation is used to calculate monolayer viscoelastic parameters at air/liquid interfaces.[28,29]

2.32 Theoretical Power Spectrum for a Monolayer-Covered Surface

To obtain the spectrum for the vertical displacement u_z of a monolayer-covered surface ($\eta_1 = 0$ and $\rho_1 = 0$), we look for a v_z solution of Eqs. (2.67) - (2.69) satisfying the boundary conditions Eqs. (2.81) - (2.85) at the interface and also satisfying an appropriate set of initial conditions. We can choose these initial conditions using statistical mechanics considerations applied to a system at thermal equilibrium. It also suffices to consider horizontal motion restricted to the x direction and vertical motion to the z direction.

The vertical displacement u_z is related to the velocity $\mathbf{v}$ by

$$\dot{u}_z(x,t) = v_z(x, z=0, t) \tag{2.98}$$

The Fourier transforms with respected to x of v_z and u_z are $v_z(k,z,t)$ and $u_z(k,t)$.

It can be shown that the mean square of a thermodynamic fluctuation, calculated from the minimum work necessary to create a fluctuation[30], is

$$\overline{|u_z(k,0)|^2} = \frac{k_B T}{\sigma k^2}. \tag{2.99}$$

where k_B is Boltzmann's constant, and T is the absolute temperature.

The Laplace transforms of $v_z(k,z,t)$ and $u_z(k,t)$ with respect to time are introduced to take account of the initial condition. Thus,

$$\tilde{v}_z(k,z,s) = \int_0^\infty dt e^{-st} v_z(k,z,t) \tag{2.100}$$

$$\tilde{u}_z(k,s) = \int_0^\infty dt e^{-st} u_z(k,t) \tag{2.101}$$

where

$$\tilde{v}_z(k, z=0, s) = -u_z(k,0) + s u_z(k,s). \tag{2.102}$$

The power spectrum of the surface waves is given by[30]

$$P_k(\omega) = \frac{1}{\pi} Re[\overline{\tilde{u}_z(k,s)\tilde{u}_z^*(k,0)}]_{s=-i\omega}. \tag{2.103}$$

The power spectrum $P_k(\omega)$ can be written as[16]

$$\begin{aligned} P_k(\omega) = &- k_B T \tau_0^2 k/(\pi\omega\rho) Im\{-\omega^2\tau_0^2/D(\omega) + [\varepsilon\rho/(4\eta^2 k) + \\ &ik\kappa\omega\tau_0/(2\eta)][(1+i2\omega\tau_0)^{1/2} - 1]/D(\omega)\} \end{aligned} \tag{2.104}$$

where

$$\begin{aligned} D(\omega) = &- \omega^2\tau_0^2[(1+i\omega\tau_0)^2 + \sigma\rho/(4\eta^2 k) - (1+i2\omega\tau_0)^{1/2}] + \\ &(\varepsilon + i\omega\kappa)\rho/(4\eta^2 k)\{-\omega^2\tau_0^2(1+i2\omega\tau_0)^{1/2} + \\ &\rho(\sigma + i\omega\mu)/(4\eta^2 k)[(1+i2\omega\tau_0)^{1/2} - 1]\} - i\mu k\omega^3\tau_0^3/(2\eta) \end{aligned} \tag{2.105}$$

and where $\tau_0 = \rho/2\eta k^2$, with ρ and η the density and viscosity of the liquid (phase 2).

For a monolayer-free air/liquid interface where $\varepsilon = 0$ and $\kappa = \mu = 0$, the power spectrum Eq. (2.105) can be written as[30]

$$P_k(\omega) = \frac{k_B T}{\pi\omega}\frac{\tau_0^2 k}{\rho}\left\{\frac{ImD(i\omega\tau_0)}{|D(i\omega\tau_0)|^2}\right\} \tag{2.106}$$

where $D(s) = Y + (1+s)^2 - \sqrt{1+2s}$ is the dispersion equation for a simple liquid surface, with $Y = \sigma\rho/4\eta^2 k$ and $\tau_0 = \rho/2\eta k^2$.

2.33 Dispersion Equation for Surface Waves of Concentrated Polymer Solutions

Polymer solutions change from being viscous fluids to viscoelastic fluids when polymer concentration is increased. Harden *et al.*[18] made detailed calculations of the dynamics of surfaces of polymer solutions. We will review their treatments of the surface modes on the air/polymer solution interface.

A. Assumptions of the Theory

The unperturbed material occupies the semi-infinite half space, $z > 0$, and the dilute vapor occupies the rest of space. At the boundary of the medium, $z = 0$, thermal fluctuations or weak externally applied perturbations are assumed to induce small amplitude surface modes. The concentration of polymer in the solvent is spatially uniform through the medium. In particular, this implies that there are no gradients of polymer concentration near the interface. Thus, the boundary between material and vapor may be characterized by a step function density profile and a single surface tension.

The entangled polymer network is treated as a viscoelastic continuum with complex shear and compressional moduli G^* and K^* respectively, and with density ρ_p; the solvent is treated as a Newtonian fluid with viscosity η_s and density ρ_s. The

interaction between polymer and solvent can be represented by an effective local frictional force, $\mathbf{f}_I(\mathbf{v}, \dot{\mathbf{u}})$, proportional to the difference between polymer network and solvent velocities.[32] The proportionality factor scales as η_s/ξ^2, where η_s is the solvent viscosity and ξ is the characteristic mesh size of the polymer network.

B. The Effective Equations of Motion for Polymer Solutions and Gels

Under these assumptions, the linearized coupled equations of motion have the form

$$\rho_s \frac{\partial \mathbf{v}}{\partial t} = \nabla \cdot \sigma^{(s)} + \mathbf{f}_I(\mathbf{v}, \dot{\mathbf{u}}) \tag{2.107}$$

$$\rho_p \frac{\partial^2 \mathbf{u}}{\partial^2 t} = \nabla \cdot \sigma^{(p)} - \mathbf{f}_I(\mathbf{v}, \dot{\mathbf{u}}) \tag{2.108}$$

where $\mathbf{v}$ is the solvent velocity field, $\mathbf{u}$ is the polymer displacement field, ρ_s and ρ_p are the solvent and polymer density in the medium, $\sigma^{(s)}$ and $\sigma^{(p)}$ are the local solvent and polymer stress tensors, and $\mathbf{f}_I(\mathbf{v}, \dot{\mathbf{u}}) = \chi(\dot{\mathbf{u}} - \mathbf{v})$ with $\chi \sim \eta_s/\xi^2$. In analogy with the mechanics of Newtonian fluids and linear elastic solids, $\sigma^{(s)}$ and $\sigma^{(p)}$ have the form[21,31]

$$\sigma_{ij}^{(s)} = \eta_s \left(\frac{\partial v_i}{\partial x_j} + \frac{\partial v_j}{\partial x_i} \right) - p\delta_{ij} \tag{2.109}$$

$$\sigma_{ij}^{(p)} = G^* \left(\frac{\partial u_i}{\partial x_j} + \frac{\partial u_j}{\partial x_i} \right) + \left(K^* - \frac{2}{3} G^* \right) [\nabla \cdot \mathbf{u}] \delta_{ij} \tag{2.110}$$

where η_s is the solvent viscosity, p is the solvent hydrostatic pressure, v_i is the ith component of the solvent velocity field, G^* and K^* are the complex shear and compressional moduli of the polymer network, and u_i is the ith component of the polymer network displacement field. In the limit of a perfect coupling between polymer and solvent, χ becomes arbitrarily large and the local solvent velocity approaches the local polymer network velocity: $\mathbf{v} \rightarrow \dot{\mathbf{u}}$. Then, the coupled equations of motion reduce to a single equation of motion of mixture. We have its form in frequency space

$$i\omega\rho\mathbf{v} = \nabla \cdot \sigma(\omega) \tag{2.111}$$

where $v_i = v_i(\mathbf{r},\omega)$ is the time Fourier transform of the velocity field, $\rho = \rho_s + \rho_p$, and $\sigma(\omega)$ is the frequency space representation of the effective stress tensor of the medium

$$\sigma_{ij}(\omega) = \eta(\omega)\left(\frac{\partial v_i}{\partial x_j} + \frac{\partial v_j}{\partial x_i}\right) - p_{eff}(\omega)\delta_{ij} \tag{2.112}$$

where $\eta(\omega) = \eta_0 + G^*(\omega)/i\omega$, and $p_{eff}(\omega) = p(\omega) - [K^*(\omega) - (2/3)G^*(\omega)]\nabla\cdot\mathbf{v}(\omega)/i\omega$.

In the incompressible limit, $p_{eff}(\omega) \approx p(\omega)$ and $\nabla\cdot\mathbf{v} = 0$, we have the effective equation of motion

$$i\omega\rho\mathbf{v} = \nabla\cdot\sigma(\omega)$$

$$\nabla\cdot\mathbf{v} = 0 \tag{2.113}$$

where $\sigma_{ij}(\omega)$ is given by

$$\sigma_{ij}(\omega) = \eta(\omega)\left(\frac{\partial v_i}{\partial x_j} + \frac{\partial v_j}{\partial x_i}\right) - p(\omega)\delta_{ij}. \tag{2.114}$$

C. The Boundary Conditions

The boundary conditions can be specified:
(1) mode amplitude decays into the medium, $v_i \to 0$ as $z \to \infty$,
(2) at the free surface of the medium,

$$\sigma_{zz}(\omega) = \sigma\nabla_t^2\zeta(\mathbf{x},\omega) \quad on \quad z = 0 \tag{2.115}$$

$$\sigma_{xz}(\omega) = \sigma_{yz}(\omega) = 0 \quad on \quad z = 0 \tag{2.116}$$

where σ is the surface tension of the medium, $\zeta(\mathbf{x},\omega)$ is the z component of the time Fourier transformed local surface displacement from equilibrium, $\mathbf{x}$ is the transverse coordinate vector (x, y), and ∇_t^2 is the transverse Laplacian operator.

D. The Surface Mode Dispersion Relation

The surface mode dispersion equation can obtained by solving Eq. (2.113) with the boundary conditions.

The velocity field $\mathbf{v}$ is considered to have the form $\mathbf{v} = \mathbf{v}_0 + \mathbf{v}_t$, where $\mathbf{v}_0 = \nabla\varphi$ is the velocity of potential flow and $\mathbf{v}_t$ is the rotational part of the velocity field. For two-dimensional waves on a surface, it suffices to assume that all dynamic quantities are functions of position only in the x and z directions and are independent of y. We look for solutions of the following type: $\zeta(\mathbf{x},\omega) \sim exp(ikx)$, $v(\mathbf{r},\omega) \sim exp(ikx)$, and $p(\mathbf{r},\omega) \sim exp(ikx)$. The vertical displacement of the interface is

$$\dot{\zeta}(\mathbf{x},t) = -v_z(\mathbf{x},0,t). \tag{2.117}$$

The incompressibility condition in Eq. (2.113) yields, $\nabla^2\varphi = 0$, thus φ has the form $\varphi = \varphi_0 exp(ikx - kz)$. Eq. (2.113) may then be written

$$i\omega\rho\nabla\varphi + i\omega\rho\mathbf{v}_t = -\nabla p + \eta(\omega)\nabla^2\mathbf{v}_t$$

$$\nabla \cdot \mathbf{v}_t = 0. \tag{2.118}$$

Together these imply $p = -i\omega\rho\varphi + p_0$. By choosing the constant $p_0 = 0$, we have

$$p = -i\omega\rho\varphi. \tag{2.119}$$

Furthermore, taking the curl of Eq. (2.118), gives

$$i\omega\rho\nabla \times \mathbf{v}_t = \eta(\omega)\nabla^2(\nabla \times \mathbf{v}_t). \tag{2.120}$$

Substituting the form $(v_t)_i = \alpha_i exp(ikx - qz)$, where $q = q(k,\omega)$, into Eq. (2.120) gives

$$q(k,\omega) = \left(k^2 + \frac{i\omega}{\nu(\omega)}\right)^{1/2} \tag{2.121}$$

where $\nu(\omega) = \eta(\omega)/\rho$. From Eq. (2.118), we also have

$$\alpha_x = -(iq/k)\alpha_z. \tag{2.122}$$

Using Eq. (2.117), Eq. (2.119), and Eq. (2.122), the normal stress boundary condition, Eq. (2.115), and the shear stress boundary condition, Eq. (2.116), may be written

$$(2\eta(\omega)k^2 + \sigma k^3/i\omega + i\omega\rho)\varphi_0 - (2\eta(\omega)q + \sigma k^2/i\omega)\alpha_z = 0 \tag{2.123}$$

$$2k^3\varphi_0 - (q^2 + k^2)\alpha_z = 0. \tag{2.124}$$

By eliminating the ratio φ_0/α_z from Eqs. (2.123) and (2.124) and using Eq. (2.121), the surface mode dispersion equation is obtained

$$D(k,\omega) = \left(i\omega + 2\nu(\omega)k^2\right)^2 - 4\nu(\omega)^2k^4\left(1 + \frac{i\omega}{\nu(\omega)k^2}\right)^{1/2} + \sigma k^3/\rho. \tag{2.125}$$

The surface modes frequencies $\omega(k)$ are given implicitly by the solutions of $D(k,\omega) = 0$ with $D(k,\omega)$ from Eq. (2.125).

E. Discussion of the Surface Mode Dispersion Relation

For polymer solutions within the Maxwell model, the complex shear modulus $G^*(\omega)$ is:[33]

$$G^*(\omega) = \frac{iG_0\omega\tau}{(1 + i\omega\tau)} \tag{2.126}$$

where G_0 is the transient modulus of the polymer network, and τ is the stress relaxation time of the medium. Note that G_0 and τ increase as the polymer concentration is increased in the polymer solution, indicating a stronger viscoelastic behavior of the solution.

Three types of modes may be obtained from Eq. (2.125): capillary modes ($\omega_k \sim k^{3/2}$), elastic modes ($\omega_k \sim k$) and overdamped modes ($\omega_k \sim ik^2$). (Capillary modes appear when $\sigma k^3 \gg \eta(\omega)^2k^4$. In the opposite limit, $\sigma k^3 \ll \eta(\omega)^2k^4$, elastic modes appear when $\eta_0 \ll G_0/\omega$, while overdamped liquid modes appear when $\eta_0 \gg G_0/\omega$.) The overdamped modes only exist at very high wave vector, and they are not observable in the present experiments. The three surface mode regimes are illustrated in Fig. 2.6 in a diagram of mode structure as a function of wave vector and shear modulus, G_0.

For pure simple liquid systems and very low concentration polymer solutions, the transient modulus is zero or very small, $G^*(\omega) \sim 0$ and chain relaxation times are short; the dominant term in Eq. (2.125) on the right hand side is the last term. Then the dispersion equation $D(k,\omega)$ from Eq. (2.125) has the simple form $D(s)$:

$$D(s) = Y + (1 + s)^2 - \sqrt{1 + 2s} \tag{2.127}$$

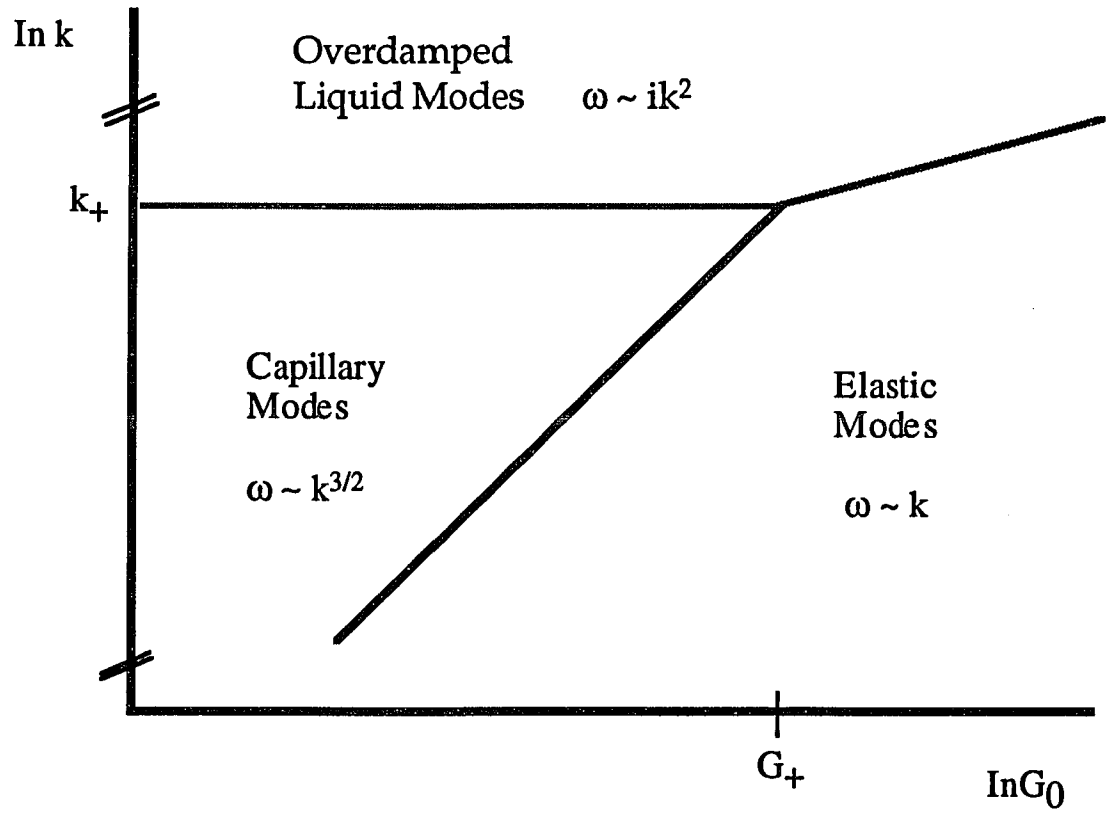

Fig. 2.6. Surface mode diagram for polymer solutions showing regions of capillary, Rayleigh elastic, and overdamped liquid modes as a function of wave vector, k, and elastic modulus, G_0. Axes are scaled logarithmically, and mode regime boundaries are indicated by a characteristic wave vector $k_+ = \rho\sigma/\eta_s^2$ a characteristic modulus $G_+ = \rho\ (\sigma/\eta_s)^2$, where ρ and σ are, respectively, the density and the surface tension of the polymer solutions, and where η_s is the viscosity of the solvent. The cuts along the k axis schematically indicate the existence of upper and lower bounds on the allowed wave vectors.

where $s = i\omega\rho/2\eta k^2$, $Y = \sigma\rho/4\eta^2 k$, and η is the viscosity of system. We recover the dispersion relation for simple liquid given by Eq. (2.94).

For high concentration polymer solutions, the transient elastic modulus is large and the chain relaxation time is long; the dominant term in Eq. (2.125) is the second term. Similar considerations as above yield the dispersion relation in this case as:

$$\omega_k = (0.91 G_0/\rho)^{1/2} k \tag{2.128}$$

i.e. the surface mode is an elastic mode. The power spectrum has a Lorentzian profile which peaks at ω_k and a full-width at half-maximum of:

$$\nabla f_{s,c} \approx \frac{0.14\eta_s k^2}{\rho}. \tag{2.129}$$

For intermediate polymer concentrations, the behavior of the polymer solutions is quite complicated, and the surface modes transform from elastic modes to capillary modes as wave vector is increased.

2.34 Theoretical Power Spectrum of Thermal Fluctuation on an Air/solution Interface

To obtain the surface mode power spectrum $S(k,\omega)$, we must solve linearized equations of motion and boundary conditions for an incompressible fluid in which the effective stress tensor of the medium has additional random sources of the stress due to the thermal fluctuations in the medium. The inhomogeneous equation of motion is given as

$$i\omega\rho\mathbf{v} = \nabla \cdot [\sigma(\omega) + \mathbf{S}(\omega)]$$

$$\nabla \cdot \mathbf{v} = 0 \tag{2.130}$$

where $\mathbf{S}(\omega)$ is the random sources of stress in the medium, and $\sigma(\omega)$ is the effective stress tensor of the medium given by Eq. (2.114). The boundary conditions state $v_i \to 0$ as $z \to \infty$ and for normal and shear stress at $z = 0$

$$\sigma_{zz}(\omega) + S_{zz}(\omega) = \sigma\nabla_t^2\zeta(\mathbf{x},\omega) \quad at \quad z = 0 \tag{2.131}$$

$$\sigma_{xz}(\omega) + S_{xz}(\omega) = 0 \quad at \quad z = 0$$

$$\sigma_{yz}(\omega) + S_{yz}(\omega) = 0 \quad at \quad z = 0. \tag{2.132}$$

The components of the random stress tensor S_{ij} are related to the generalized viscosity $\eta(\omega)$ through the generalized fluctuation-dissipation theorem for classical fluids:[31,34]

$$\begin{aligned}\langle S_{ik}(\mathbf{x}, z, \omega) S^*_{ji}(\mathbf{x}', z', \omega')\rangle =& 4\pi k_B T Re[\eta(\omega)]\delta(\mathbf{x} - \mathbf{x}')\delta(z - z') \\ & \delta(\omega - \omega')[\delta_{ij}\delta_{kl} + \delta_{il}\delta_{jk}]\end{aligned} \tag{2.133}$$

where k_B is Boltzmann's constant and T is the absolute temperature.

Introduce the one-dimensional spatial Fourier transform defined by

$$f(k) = \int_{-\infty}^{+\infty} f(x, z, \omega) exp(ikx) dx. \tag{2.134}$$

The inhomogeneous equation of motion, Eq. (2.130) for the Fourier transformed velocities and pressure are given by

$$\begin{aligned}i\omega\rho v_x(k) =& - ikp(k) + \eta(\omega)\hat{D}v_x(k) \\ & + ikS_{xx}(k) + \frac{\partial}{\partial z}S_{xz}(k)\end{aligned} \tag{2.135}$$

$$\begin{aligned}i\omega\rho v_z(k) =& \frac{\partial}{\partial z}p(k) + \eta(\omega)\hat{D}v_z(k) \\ & + ikS_{xz}(k) + \frac{\partial}{\partial z}S_{zz}(k)\end{aligned} \tag{2.136}$$

$$ikv_x(k) + \frac{\partial}{\partial z}v_z(k) = 0 \tag{2.137}$$

where $v_i(k) = v_i(k, z, \omega)$, $p(k) = p(k, z, \omega)$, $S_{ij}(k) = S_{ij}(k, z, \omega)$ are the Fourier transformed velocity components, pressure, and the random stress tensor components, respectively, and where $\hat{D}$ is the Fourier transformed Laplacian operator: $\hat{D} = (\partial^2/\partial z^2) - k^2$. The corresponding Fourier transformed boundary conditions are given by

$$2\eta(\omega)\frac{\partial}{\partial z}v_z(k) + S_{zz}(k) - p(k) = -i\sigma k^2 v_z(k)/\omega \quad at \quad z = 0 \tag{2.138}$$

$$\eta(\omega)\left(\frac{\partial}{\partial z}v_x(k)+ikv_z(k)\right)+S_{xz}(k)=0 \quad at \quad z=0. \tag{2.139}$$

The general solution for v_z can be found from the equations of motion Eqs. (2.135)-(2.137) with boundary conditions Eqs. (2.138) and (2.139). Using $\zeta(k,\omega) = v_z(k,0,\omega)/i\omega$ gives the Fourier transformed surface mode amplitude $\zeta(k,\omega)$ in terms of integrals of the S_{ij} over the normal coordinate z

$$\zeta(k,\omega)=2\nu(\omega)k^2[(1+\alpha(\omega)^2)I_1(k,\omega)-2\alpha(\omega)I_\alpha(k,\omega)]/D(k,\omega)\rho \tag{2.140}$$

where

$$I_1=\frac{k^2}{2i\omega}\int_0^{+\infty} exp(-kz')[S_{xx}(z')-S_{zz}(z')-2iS_{xz}(z')]dz' \tag{2.141}$$

$$I_\alpha=\frac{k^2}{2i\omega}\int_0^{+\infty} exp(-\alpha kz')[S_{xx}(z')-S_{zz}(z')-i\frac{(1+\alpha^2)}{\alpha}S_{xz}(z')]dz' \tag{2.142}$$

and

$$\alpha(k,\omega)=\left(1+\frac{i\omega}{\nu(\omega)k^2}\right)^{1/2} \tag{2.143}$$

and $D(k,\omega)$ is given by Eq. (2.125). The power spectrum is obtained from Eq. (2.140)

$$\langle|\zeta(k,\omega)|^2\rangle=\frac{4\nu(\omega)^2k^4\Lambda(k,\omega)}{|D(k,\omega)|^2} \tag{2.144}$$

where $|\zeta|$ denotes the modulus of ζ, and where $\Lambda(k,\omega)$ is given in terms of thermal averages of I_1 and I_α and has the form

$$\begin{aligned}\Lambda(k,\omega) =&\{|1+\alpha(\omega)^2|^2\langle I_1I_1^*\rangle+4|\alpha(\omega)|^2\langle I_\alpha I_\alpha^*\rangle\\ &-4Re(\alpha^*(\omega)(1+\alpha(\omega)^2)\langle I_1I_\alpha^*\rangle)\}/\rho^2.\end{aligned} \tag{2.145}$$

The thermal averages $\langle I_1I_1^*\rangle$, $\langle I_\alpha I_\alpha\rangle$, and $\langle I_1I_\alpha\rangle$ are readily evaluated using the definitions of I_1 and I_α from Eqs. (2.141) and (2.142) and the fluctuation-dissipation relation given by Eq. (2.133)

$$\langle I_1I_1^*\rangle=(2\pi)^3 2k_BTRe[\eta(\omega)]k^3/\omega^2$$

$$\langle I_\alpha I_\alpha\rangle=\frac{1}{[\alpha(\omega)+\alpha^*(\omega)]}\left[1+\frac{1}{4}\frac{|1+\alpha(\omega)^2|^2}{|\alpha(\omega)|^2}\right]\langle I_1I_1^*\rangle$$

$$\langle I_1 I_\alpha \rangle = \frac{1}{[1+\alpha^*(\omega)]}\left[1+\frac{1}{2\alpha^*(\omega)}(1+\alpha^2)^*\right]\langle I_1 I_1^* \rangle. \tag{2.146}$$

Inserting of these expressions into Eqs. (2.140) gives the power spectrum

$$S(k,\omega) = \frac{8k_B T Re[\eta(\omega)]k^3}{\left|D(k,\omega)\right|^2}\left\{1+\frac{1}{2Re[\alpha(k,\omega)]}-2Re\left(\frac{1}{1+\alpha(k,\omega)}\right)\right\} \tag{2.147}$$

where $D(k,\omega)$ is given by Eq. (2.125), and where $S(k,\omega) = (2\pi)^3\langle|\zeta(k,\omega)|^2\rangle$.

For a low viscosity Newtonian liquid, $\eta(\omega) = \eta$ and $|i\omega/\nu(\omega)k^4| \gg 1$. In this limit, Eq. (2.147) can be written as

$$S(k,\omega) \doteq \frac{k_B T}{\pi\omega}\frac{\tau_0^2 k}{\rho}\left\{\frac{ImD(i\omega\tau_0)}{|D(i\omega\tau_0)|^2}\right\} \tag{2.148}$$

where $D(s) = Y + (1+s)^2 - \sqrt{1+2s}$ is the dispersion equation for a simple liquid surface, $Y = \sigma\rho/4\eta^2 k$, $\tau_0 = \rho/2\eta k^2$, ρ and η, respectively, are the density and viscosity of system. The form of Eq. (2.148) is the well known theoretical power spectrum derived by Bouchiat and Meunier.[30]

References

1. F. W. Billmeyer, JR., *Textbook of Polymer Sciences* (John Wiley & Sons, Inc., N.Y. 1984).

2. P.-G. de Gennes, *Scaling Concepts in Polymer Physics* (Cornell Univ. Press, Ithaca, N.Y. 1979).

3. P. Flory, *Principles of Polymer Chemistry* (Cornell University Press, Ithaca, N.Y. 1971).

4. J. D. Ferry, *Viscoelastic Properties of Polymers* (John Wiley & Sons, Inc., N.Y. 1980).

5. B. J. Berne and R. Pecora, *Dynamic Light Scattering* (Wiley-Interscience, N.Y. 1976).

6. H. Z. Cummins and E. R. Pike, *Photon Correlation and Light Beating Spectroscopy* (Plenum Press, N.Y. 1974).

7. H. Z. Cummins and E. R. Pike, *Photon Correlation Spectroscopy and Velocimetry* (Plenum Press, N.Y. 1977). 1977.

8. B. Chu, *Laser Light Scattering* (Academic Press, N.Y. 1974) Ch. IV.

9. H. Z. Cummins and H. L. Swinney, *Prog. Opt.* **8**, 133 (1970).

10. V. Levich, *Physiochemical Hydrodynamics* (Prentice Hall, Englewood Cliffs, N.J. 1962).

11. R. Dorrestein, *Koninkl. Ned. Akad. Wetenshap. Proc.* **B54**, 260 (1951).

12. F. C. Goodrich, *J. Phys. Chem.* **66**, 1858 (1962).

13. R. S. Hansen and J. A. Mann, *J. Appl. Phys.* **35**, 152 (1964).

14. M. van den Tempel and R. P. van de Riet, *J. Chem. Phys.* **42**, 2769 (1965).

15. L. Kramer, *J. Chem. Phys.* **55**, 2097 (1971).

16. D. Langevin, *J. Colloid Interface Sci.* **80**, 412 (1981).

17. J. A. Mann, in *Surface and Colloid Science* edited by E. Matijevic and R. J. Good (Plenum Press, N.Y. 1984; Vol 13, P145).

18. J. L. Harden, H. Pleiner, and P. A. Pincus, *J. Chem. Phy.* **94**, 5208 (1991).

19. G. L. Gaines, *Insoluble Monolayers at the Liquid Gas Interface*, (Wiley, N.Y, 1966).

20. D. J. Crisp, *J. Colloid Sci.* **1**, 49 (1946).

21. L. D. Landau and E. M. Lifshitz, *The Theory of Elasticity* (Pergamon Press, N.Y. 1959).

22. J. C. Herpin and J. Meunier, *J. Phys. (Paris)* **35**, 847 (1974).

23. S. Hård, Y. Hamnerius, and O. Nilsson, *J. Appl. Phys.* **47**, 2433 (1976).

24. M. Sano, M. Kawaguchi, Y-L. Chen, R.L. Skarlupka, T. Chang, G. Zografi, and H. Yu, *Rev. Sci. Instrum.* **57**(6), 1158 (1986).

25. R.B. Dorshow, A. Hajiloo, and R.L. Swofford, *J. Appl. Phys.* **63**, 1265 (1988).

26. R.H. Katyl and U. Ingard, *Phys. Rev. Lett.* **19**, 64 (1967).

27. D. Langevin, *J. Chem. Soc. Faraday Trans.1* **70**, 95 (1974).

28. D. Langevin and M. A. Bouchiat, *C. R. Acad. Sci. Paris* **272B**, 1422 (1971).

29. S. Hård and R. D. Neuman, *J. Colloid Interface Sci.* **83**, 315 (1981).

30. M. A. Bouchiat and J. Meunier, *J. Physique* **32**, 561 (1971).

31. L. D. Landau and E. M. Lifshitz, *Fluid Mechanics* (Pergamon Press, N.Y. 1959).

32. P. -G. de Gennes, *Macromolecules* **9**, 594 (1976).

33. H. Pleiner, J. L. Harden, and P.A. Pincus, *Europhys. Lett.* **7**(5), 383 (1988).

34. L. D. Landau and E. M. Lifshitz, *Statistical Mechanics* (Pergamon Press, N.Y. 1980).

Chapter 3

EXPERIMENTAL METHODS

In this chapter, three experimental techniques will be presented. For each technique, the experimental details including instrumentation and measurement methods will be given. The first is the technique for the measurement of static surface tension. The second is the technique of surface heterodyne light technique. The third technique is used to measure the rheological properties of polymer solutions. There are two other experimental techniques involved in my thesis work, ellipsometry and atomic force microscopy (AFM). Their breif descriptions will be given in the appendices.

3.1 Surface Tension Measurements

In the condensed liquid, the intermolecular attraction forces are enormously high in magnitude due to the dipolar and dispersion interaction. These short-range forces suggest an explanation of the phenomena of surface tension.

Molecules in the bulk phase of liquid are, on the average, subjected to the attractive force of the other liquid molecules in all directions so that the resultant force is very small on average. However, molecules in the interfacial phase are subjected to asymmetric fields of force because of the net attraction by molecules in the bulk of the liquid. As a result of these asymmetric fields, the energy of molecules in the interfacial phase become greater than these in the bulk phase, and the surface of a liquid contracts until it contains the minimum number of molecules possible. Thus, the surface layer is in a state of tension compared with the condition in the bulk phase.

The methods of measuring the surface tension are based on two principles: (1) measurement of downward forces exerted by surface tension on a vertical plate which is allowed to dip into the liquid, or measurement of the force required to pull

a ring normally from the liquid surface.

(2) measurement of the dimensions of sessile drops or bubbles which are molded by the combined effects of surface tension and gravity.

In this thesis, the measurement of surface tension is by Wilhelmy plate[1,2] and du Nouy methods founded on (1) above.[2–6] A short description of these two methods will be presented.

A. Wilhelmy Plate Method

In the common form of Wilhelmy balance, a thin plate, usually platinum, is suspended in the liquid surface (Fig. 3.1).[1,2] The forces acting on the plate then consist of the gravitational and surface tension effects, downward, partially offset by the buoyant effect due to the weight of the liquid displaced. For a rectangular plate of dimension l, w, and t, of material of density ρ_p, immersed to a depth h in a liquid of density ρ_l, we have for the net downward force

$$F = \rho_p glwt + 2\sigma(t + w)cos\theta - \rho_l gtwh \tag{3.1}$$

where σ is the liquid surface tension, θ is the contact angle of the liquid on the solid plate, and g is the gravitational constant.

The usual procedure for the use of a Wilhelmy plate involves maintaining the plate completely wetted by the liquid ($cos\theta = 1$) and measuring the change in F for a stationary plate when the surface tension is applied. If the plate is thin enough so that t is negligible compared to w, the surface tension is given by

$$\sigma = \Delta F/2w \tag{3.2}$$

where ΔF is the change in F. The buoyancy effect is very small when the plate slightly touches the liquid.

The method gives very good result if a sand-blasted roughened platinum plated is used. A $1.0cm \times 2.5cm$ thin, sand-blasted platinum plate attaches to an electronic

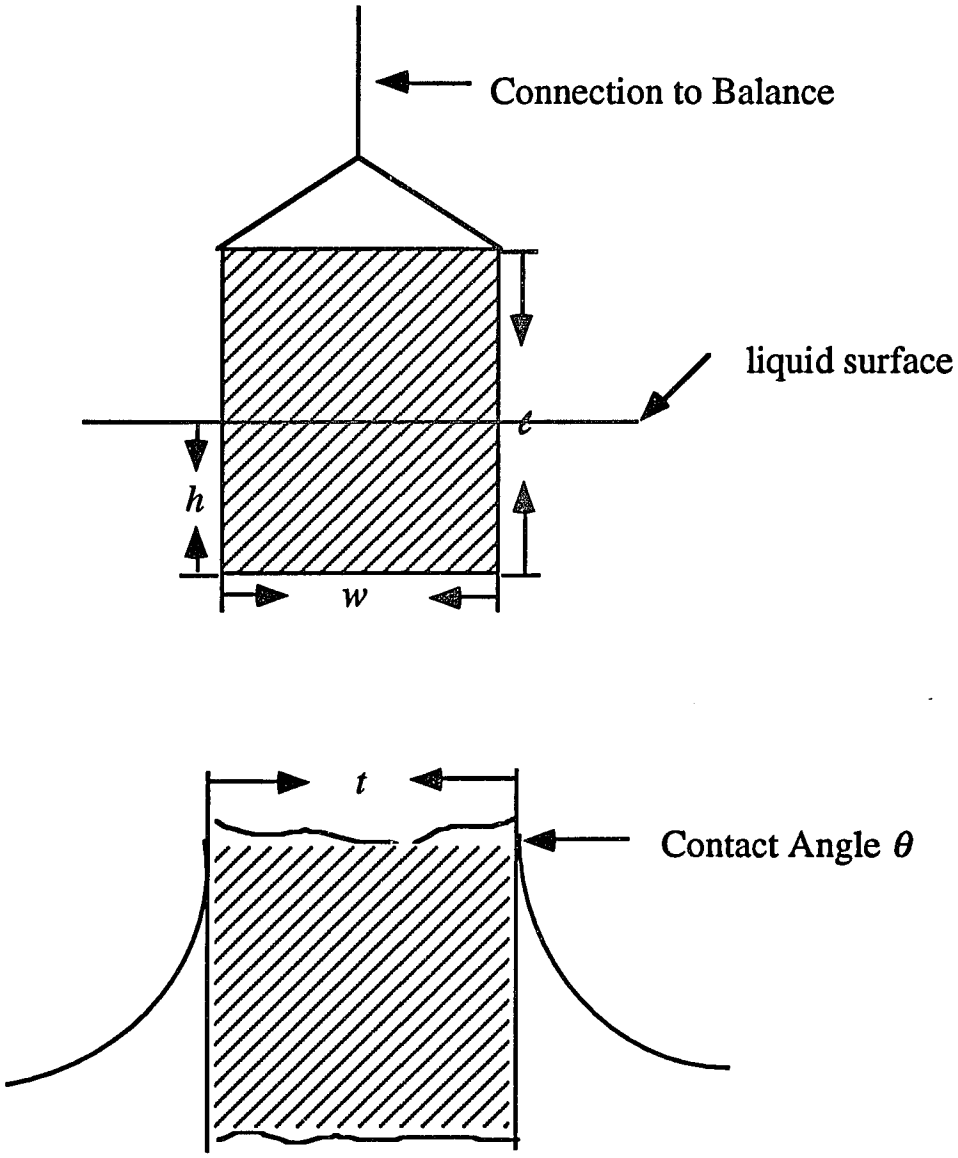

Fig. 3.1. A Wilhelmy plate partially immersed in a water surface. The lower diagram shows the detailed side view of the plate.

balance (Mettler, AE240 with 013 data interface) is used in our experiment. The calibration is done at an air/water interface before the measurement.

B. du Nouy Ring Method

This method is based on the procedure to determine surface tension from the maximum force required to pull a platinum ring from the surface of a liquid. The surface tension is calculated from the relation

$$\sigma = \frac{F_{max}}{4\pi R} \tag{3.3}$$

where F_{max} is the maximum upward pull of ring which is measured experimentally and $4\pi R\sigma$ the downward pull. R stands for the radius of the ring.

Small corrections have to be introduced on the right-hand side of the Eq. (3.3) for the estimation of σ accurately.[3,4] The extent of this correction will depend on the size of the ring, the diameter of the wire, the densities of the phases and the curvature of the detached liquid interface. The tables for the corrections are available in reference 3.

3.2 The Technique of Surface Heterodyne Light Scattering

Surface heterodyne light scattering from thermally excited surface waves is a powerful method for investigating both interfacial and bulk properties of liquid.[8–13] Surface light scattering also provides an alternative method of measuring the surface tension.

A. The Experimental Setup Description

The experimental setup is shown in Fig. 3.2. This setup is similar to the one described by Dorshow, Hajiloo and Swofford.[9] A laser beam (Spectra Physics, $35mW$ He-Ne, $\lambda = 6328$ Å, with vertical polarization) is expanded by a telescope

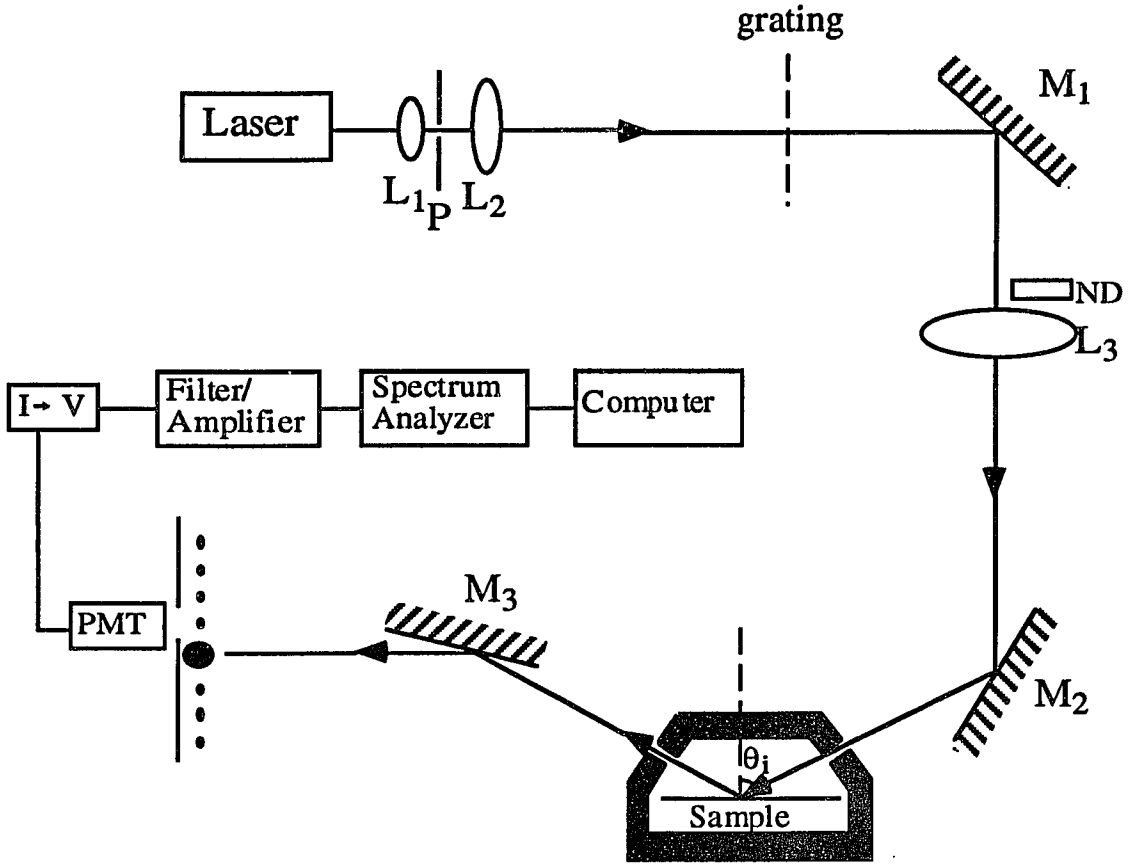

Fig. 3.2. The experimental setup for the technique of surface heterodyne light scattering.

which consists of an input lens L1, a spatial filter and an output lens L2. The input lens L1 (Newport, Model M-10X, 14.8mm focal length) focuses the laser to produce the point sources necessary for Fraunhofer diffraction. A spatial filter P (Newport, Model 900) is located at the focused spot to transmit only the Gaussian fundamental mode of the laser beam. It is mounted in a x-y translational holder to ensure correct alignment. The output lens L2 (Melles-Griot, 2.45cm diameter, 8cm fl) is placed 8.45cm from the spatial filter P and forms an image 150cm away. The expanded beam then illuminates the transmission diffraction grating (10μm lines spaced 500μm on a glass substrate) 690.5cm away from lens L2. The grating is used to generate a diffraction pattern and the desired local oscillators. The imaging lens L3 (Melles-Griot, 15cm diameter, 100cm fl) is located 200cm from the grating. The primary beam was centered on the lens to minimize aberrations in the transmitted light. Lens L3 forms a 1:1 image of the grating on the sample interface. The imaging assures that the heterodyne local oscillator beam at the detector aperture is correctly aligned with the surface scattered light. The fundamental wave vector k_I at the interface is determined by the grating spacing a, incident angle θ_i at diffraction order n=1.

$$k_I = \frac{2\pi cos\theta_i}{a} \tag{3.4}$$

The typical k_I is $50cm^{-1}$ in our experiment. This allows 9-10 diffraction orders could be detected in most measurements. The alternative way to measure surface scattering at smaller or larger wave vector could have been to increased or decreased the image magnification. For optimization, the incident angle is $\theta_i = 64^0$ which was suggested by Hård, Hamnerius and Nilsson.[7]

The sample cell, located 200cm from the imaging lens L3, is placed in a closed system on a vibration-isolation table (Newport, EVIS Electronic Vibration Isolation System) to avoid contamination and to avoid picking up vibrations from environment. The detector is positioned 354cm from the sample interface in the plane of the diffraction dot image produced by lens L3. The placement of the grating and the image lens to produce a 1:1 image of the grating at the sample interface results in a magnified diffraction dot size in the detector plane compared to the dot size in the

focal plane of lens L2. The long distance between the liquid surface and the detector, $354cm$, ensures the Fraunhofer diffraction condition. The mirror M3 is rotated to place a desired diffraction spot on the PMT detector which has a large enough hole to pass entire portion of one chosen spot. The intensity of the diffraction spots on the PMT detector is reduced by guiding them through the neutral density filter (ND) (Newport, filter set #90) in order to optimize heterodyne. Also for our experiment setup, the incident light is polarized perpendicular to the plane of incident. The detector is a photomultiplier tube (ITT Electro-optical, model FW130) chosen for its high current rating ($I_{max} = 300\mu A$), The PMT is biased at $-1800V$ by a high voltage power supply (Hewlett-Packard, model 6110A). The fluctuating PMT current passes through a voltage divider to convert to a fluctuating voltage which is sent to a low noise preamplifier (ITHACO Inc., model 1201). The output signal from the amplifier is processed by a dynamic signal analyzer (Hewlett-Packard, model 35660A). The signal analyzer is connected via a GPIB-PC interface to an IBM computer.

The theoretical expressions to optimize of the surface light scattering were given by Hård *et al.*[7] Two of the more important concerns are the beam size and the incident angle. The laser power and wavelength should also be considered. A large beam diameter or oblique incident angle give a narrow instrumental width. But in order to maximize the signal-to-noise ratio, it is desirable to keep the diameter of the beam incident on the liquid surface to a minimum and the incident angle not too close to 90^0. If the beam width is too narrow, then the image of the grating on the surface will be too small to give the proper resolution of ripple wave vector k. It was found that all conditions were best fulfilled using an incident angle of around 60^0, and a laser beam width on the surface greater than about $0.6mm$. In our experiments, the incident angle was about 60^0 and the laser beam width was $\simeq 4mm$.

B. The Selection of the Scattering Wave Vector.

In the surface light scattering studies, a series of wave vectors corresponding to a sequence of grating orders is selected by using a transmission grating. This grating provides the local oscillator for heterodyne detection and also provides defined wave vectors. Fig. 3.3 illustrates the role of the diffraction grating in heterodyne detection of light scattered by a liquid surface. In Fig. 3.3, the 3rd order diffraction spot is guided through the PMT aperture. The zeroth order or the main beam is represented by the larger circle.

The scattering angle described by k causes the surface waves with appropriate wavelengths to contribution to the scattering intensity, even through capillary waves with a wide range of wavelength are presented simultaneously at the surface. This wavelength selection is determined by a simple momentum balance equation,

$$\mathbf{k}_{inc} = \mathbf{k}_{scatt} \pm \mathbf{k} \tag{3.5}$$

where $\mathbf{k}$, $\mathbf{k}_{int}$, $\mathbf{k}_{scatt}$ are the wave vector for ripplons, incident photon and the scattered photon, respectively. Conservation of momentum parallel with the surface lead to

$$k = \frac{2\pi}{\lambda_{ripplon}} = \frac{2\pi sin\varphi cos\theta_i}{\lambda}. \tag{3.6}$$

Phase coherence of the grating with spacing a requires

$$n\lambda = asin\varphi. \tag{3.7}$$

Combining Eq. (3.6) and Eq. (3.7) gives

$$k = n\frac{2\pi cos\theta_i}{a}. \tag{3.8}$$

Thus, only ripplons with the wavelength $\lambda_{ripplon}$ contribute to the scattering at the given value k corresponding to a diffraction order.

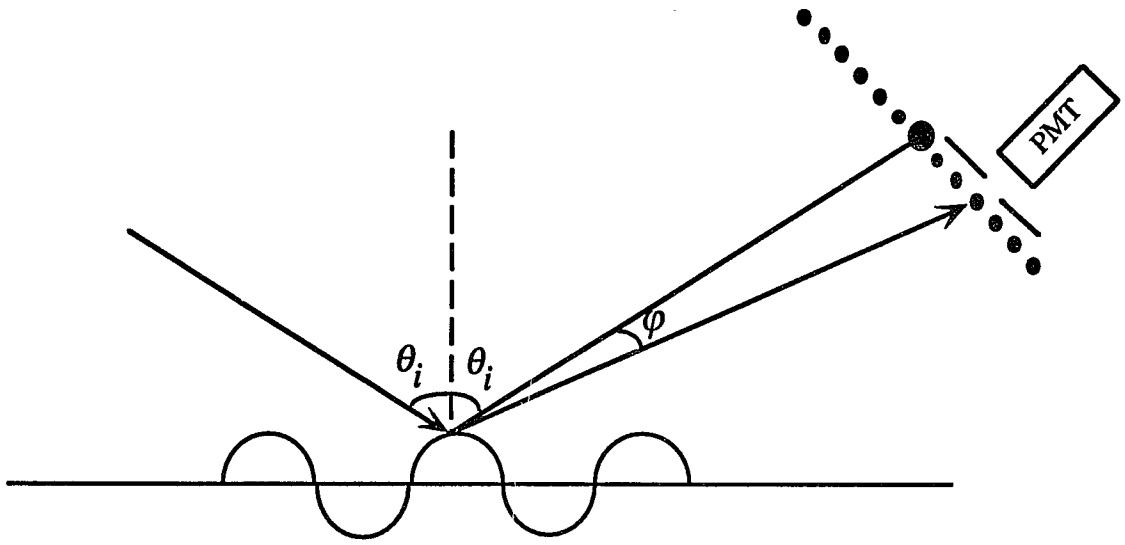

Fig. 3.3. A schematic drawing of the scattering process at the liquid surface. The laser light is incident on the surface with an angle $\theta_i \sim 60^0$. Scattered light from the incident beam is optically mixed with a diffracted beam. In this example, the PMT is centered on the third order diffraction spot from the transmission grating, and the scattering angle is defined by φ.

C. Calibration of the Wave Vector and Instrumental Broadening

Although the grating is used to select a k, an exact value of k can not be determined. The measurements contain the wave vectors Δk in the neighborhood of the desired k. This causes the experimental spectrum broader than what is expected from the relevant bulk viscosity value. The calibration of k and instrumental broadening can be obtained by the use of a liquid in which the surface tension and bulk viscosity are known. In our experiments, the solvent is used for calibration since its surface tension and viscosity are known.

For a simple fluid, the experimental power spectrum $P(\omega)$ is a convolution of a wave vector dependent instrumental function and the theoretical power spectrum of capillary waves $P_k(\omega)$ of Eq. (2.106).[14]

$$P(\omega) = \sum_{\Delta k=-N}^{N} F(\Delta k/\delta_d) \cdot P_k(\omega, k + \Delta k) \tag{3.9}$$

where $P_k(\omega, k + \Delta k)$ is the theoretical power spectrum of Eq. (2.106), N is the spread of wave vectors, δ_d is the width of instrumental function F, and k is the wave vector. Both δ_d and k are to be optimized.

The instrumental response function can be estimated by comparing the power spectrum predicted by Eq. (3.9) with various trial functions F with an experimentally obtained power spectrum of a liquid whose properties are well known.[9–11] For systems studied in this work, we found that the instrumental response was best represented by a Lorentzian squared function and 150 summation steps, $N = 75$, were sufficient for computing a smooth spectral profile,

$$P(\omega) = \sum_{\Delta k=-75}^{75} (1/[(\Delta k/\delta_d)^2 + 1]^2) \cdot P_k(\omega, k + \Delta k). \tag{3.10}$$

Fig. 3.4 shows a calibration spectrum of air/water at the diffraction order $n = 3$ at room temperature. The best fit of the power spectrum was obtained at $k = 137.87 cm^{-1}$ and $\delta_d = 9.94$ by using non-linear least squares fitting procedure.

For the spectral analysis of polymer solutions, the instrumental broadening was first determined with power spectra of solvents via air. A series of spectra was

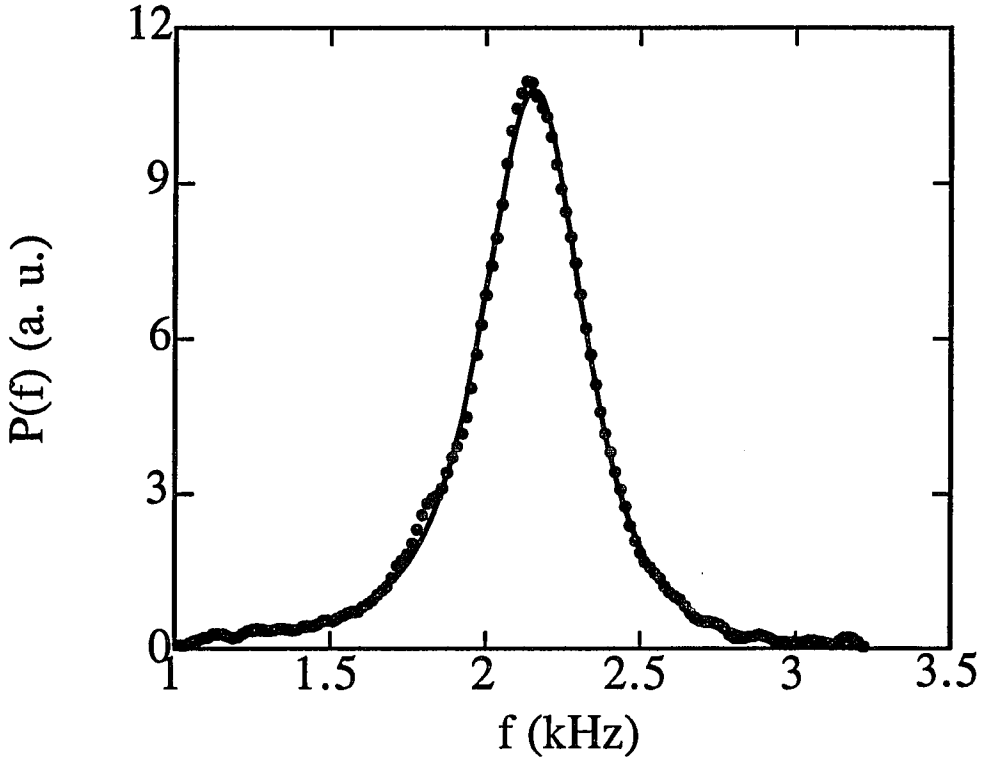

Fig. 3.4. Power spectrum of water at the diffraction order n = 3. The solid line is the fit using Eq. (3.1) with k = 137.87 cm^{-1} and δ_d = 9.94.

obtained for each diffraction order under the same optical conditions to the spectra obtained from the air/polymer solution system. Using Eq. (3.10), with $N = 75$ for each diffraction order, k and δ_d was optimized. Then, these values of k and δ_d were subsequently applied to the spectral analysis of polymer solutions.

3.3 Rheological Measurements

The rheological properties of polymer solutions were measured by the rotational viscometers. For low concentration polymer solutions, their viscosities are low and independent of shear rate. Their viscosities are measured by the low shear Couette viscometer (Contraves, low-shear 30) associated with a steady shear rate. For high concentration polymer solutions, in addition to frequency-dependent viscosities, they have nonzero, frequency-dependent shear moduli. Their viscoelastic properties are measured by the Rheometrics Fluids Mechanical Spectrometer II (Rheometrics, Inc.) associated with oscillatory strains. We have chosen the cone and plate rotational geometry due to its uniform shear rate.

A. Couette Viscometer

The geometry of the Couette viscometer (Contraves, low-shear 30) is shown in Fig. 3.5. The sample is placed between two concentric cylinders. The inner cylinder of radius R_1 is regarded as stationary which connects to the measuring system (torsion wire). The outer cylinder of radius R_2 rotates with a constant angular velocity ω. The resulting steady torque measured by the inner cylinder determines the viscosity.

For a Newtonian fluid, the magnitude of the torque G acting per unit length of the cylinder on a cylindrical surface is given by

$$G = 4\pi\eta\omega\frac{R_1^2 R_2^2}{R_2^2 - R_1^2} \tag{3.11}$$

where η is the shear viscosity of the sample. The shear rates at the inner and outer

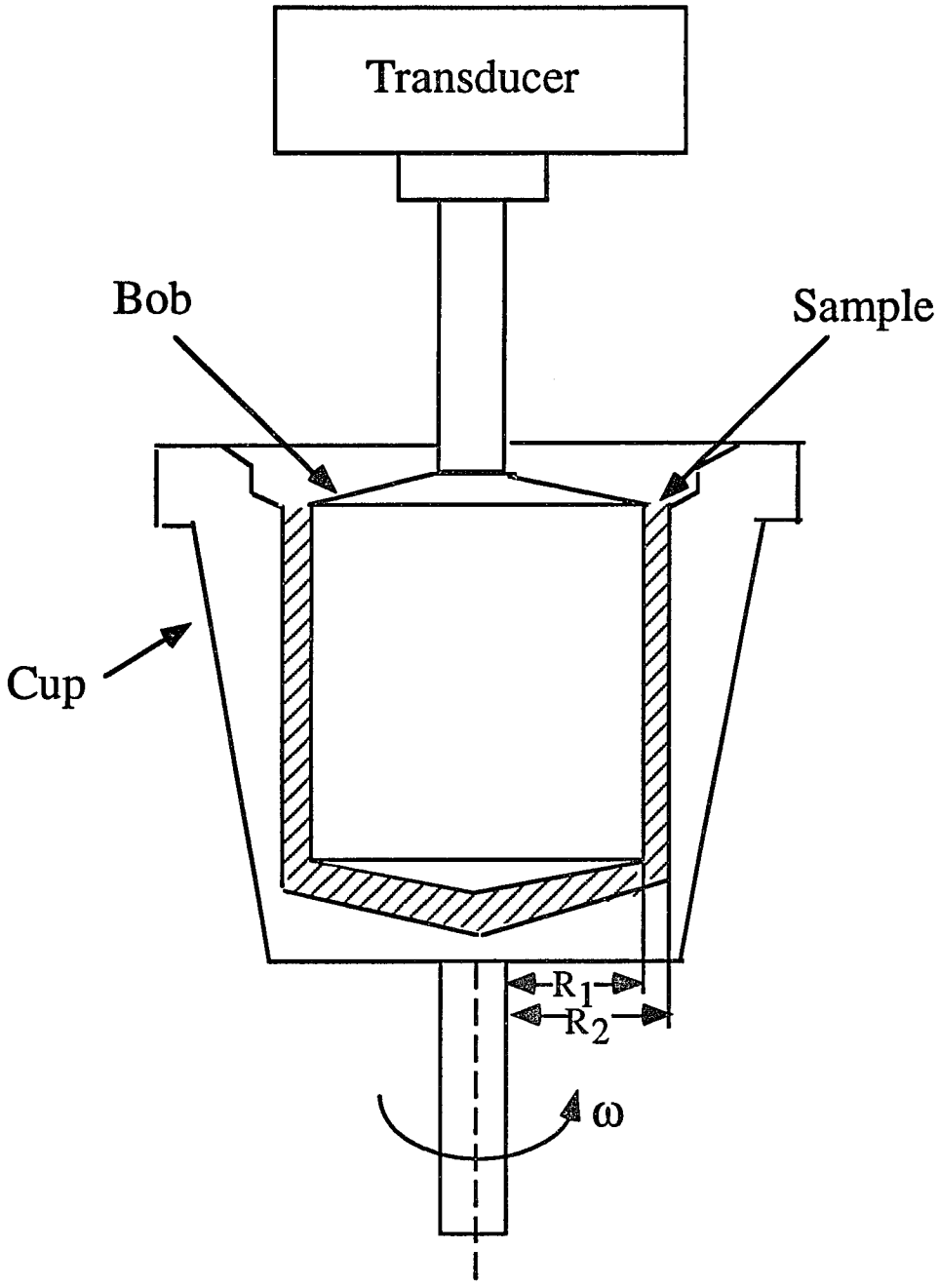

Fig. 3.5. A Couette viscometer with sample loaded.

cylinder surfaces, respectively, are:

$$\dot{\gamma}_1 = \frac{2R_2^2}{R_2^2 - R_1^2}\omega \tag{3.12}$$

$$\dot{\gamma}_2 = \frac{2R_1^2}{R_2^2 - R_1^2}\omega. \tag{3.13}$$

Usually the annular gap $(R_2 - R_1)$ is very small compared with R_1, then $\dot{\gamma}_1 \approx \dot{\gamma}_2$. The shear rate range for this instrument is 0.017 to 128 s^{-1}. The transducer measures the torque G as a function of $\dot{\gamma}$ which can be converted into the shear viscosity η via Eqs. (3.11)-(3.13).

B. Cone and Plate Rheometer

The linear viscoelastic properties of polymer solutions were measured by the Rheometrics Fluids Mechanical Spectrometer II (Rheometrics, Inc.) in the dynamic testing mode. Linear viscoelastic parameters may be obtained by measuring the steady response of polymer solution samples to a small sinusoidal deformation as a function of frequency. The strain amplitude of the oscillations is maintained sufficiently small so that the response remains linear with strain:

$$\gamma = \gamma_0 sin\omega t \tag{3.14}$$

where γ_0 is the strain amplitude, ω is the frequency and t is the time. Since polymeric materials exhibit viscoelastic response, the resulting shear stress may be resolved into an in-phase and out-of-phase components,

$$\sigma(t) = \gamma_0(G'(\omega)sin\omega t + G''(\omega)cos\omega t) \tag{3.15}$$

where $G'(\omega)$ is the dynamic storage modulus and $G''(\omega)$ is the dynamic loss modulus.

There are five concentric geometries available for this instrument. These geometries are the parallel plate, cone and plate, Couette, double wall Couette, and conical cylinder. The dynamic moduli of high concentration polymer solutions in

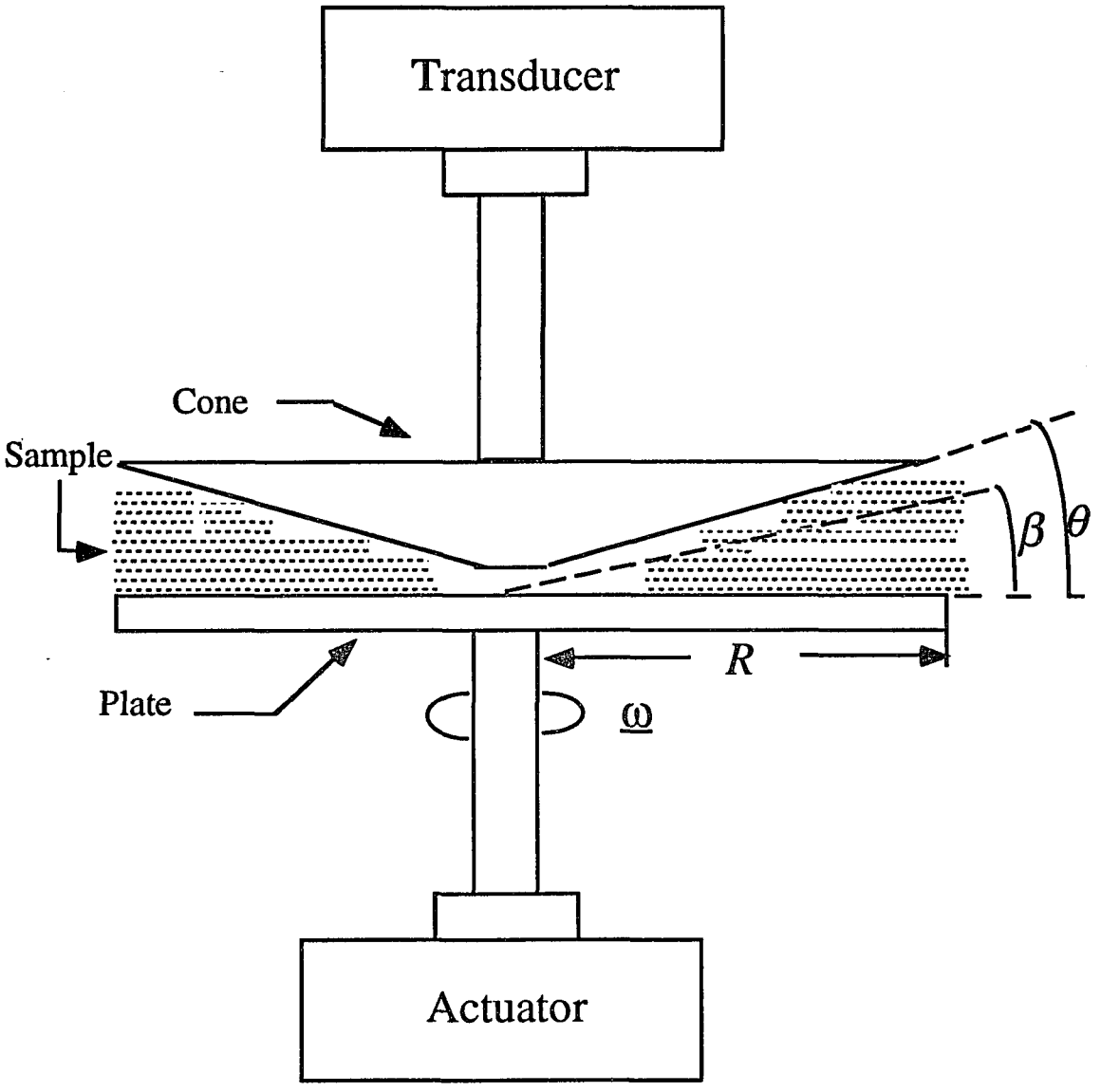

Fig. 3.6. Cone and plate geometry with sample loaded.

this thesis work were measured with the cone and plate geometry - Fig. 3.6. In this experiment, the sample is placed between the cone and plate. The plate is driven sinusoidally by the actuator. The cone, which rotates freely on an air bearing, is connected to the transducer which measures the sample response to the applied strain.

The shear strain γ is

$$\gamma = K_r * \theta \tag{3.16}$$

where K_r is the strain constant ($K_r = 1/\beta$, where β is the cone angle in radians which is usually less than 0.087 rad) and θ is the actuator angular displacement in radians, $\theta = \theta_0 sin\omega t$. The shear rate $\dot{\gamma}$ is

$$\dot{\gamma} = K_r * \dot{\theta}. \tag{3.17}$$

We can see that the shear rate is independent of the position in the gap.

The shear stress $\sigma(t)$ is related to the total torque, G_T, on the cone by

$$\sigma(t) = \frac{3G_T}{2\pi R^2} \tag{3.18}$$

where $R = 12.5mm$ is the radius of the plate. The transducer system measures the magnitude and phase shift of torque G_T as a function of shear strain. Using Eqs. (3.15) - (3.18), we obtain G' and G''. Fig. 3.7 shows a typical G' and G'' measurements for polyethyleneoxide (PEO) in water at bulk concentration $= 7.4g/dl$ and $M_w = 1000K$.

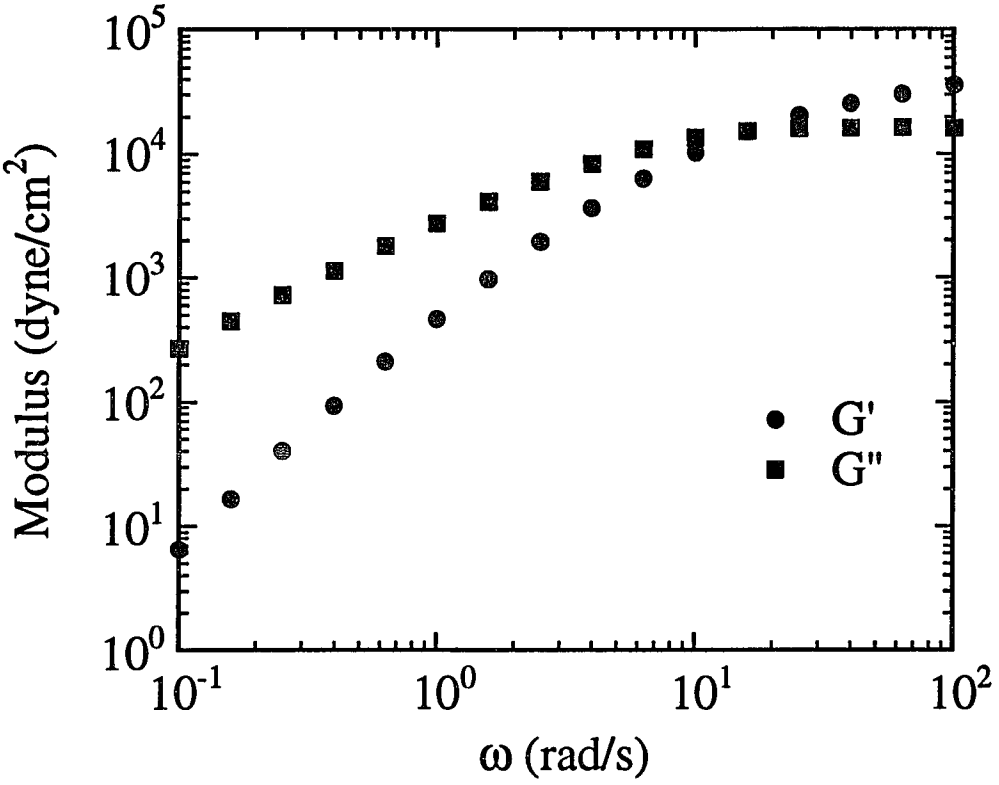

Fig. 3.7. Rheological measurements as a function of frequency, ω, for the 7.4 g/dl PEO/water solution with M_w = 1000K. The symbols correspond to: ● storage modulus, G', and ■ loss modulus, G''.

References

1. G. L. Gaines, *Insoluble Monolayers at the Liquid Gas Interface* (Wiley, N.Y. 1966).

2. D. K. Chattoraj and K. S. Birdi, *Adsorption and the Gibbs Surface Excess* (Plenum, N.Y. 1984).

3. W. D. Harkins and H. F. Jordan, *J. of Am. Chem. Soc.* **52**, 1751 (1930).

4. H. H. Zuidema and G. W. Walters, *ASTM Bull* **13**, 312 (1941).

5. X. Z. Wu, B. M. Ocko, E. B. Sirota, S. K. Sinha, M. Deutsch, B. H. Cao and M. W. Kim, *Science* **261**, 1018 (1993).

6. M. W. Kim and B. H. Cao, *Europhys. Lett* **24** (3), 229 (1993).

7. S. Hård, Y. Hamnerius, and O. Nilsson, *J. Appl. Phys.* **47**, 2433 (1976).

8. M. Sano, M. Kawaguchi, Y-L. Chen, R. L. Skarlupka, T. Chang, G. Zografi, and H. Yu, *Rev. Sci. Instrum.* **57** (6), 1158 (1986).

9. R. B. Dorshow, A. Hajiloo, and R. L. Swofford, *J. Appl. Phys.* **63**, 1265 (1988).

10. D. Langevin, *J. Chem. Soc. Faraday Trans.1* **70**, 95 (1974).

11. D. I. Jon, H. L. Rosano and H. Z. Cummins, *J. Colloid Interface Sci.* **114**, 330 (1986).

12. Y. L. Chen, M. Kawaguchi, H. Yu, and G. Zografi, *Langmuir* **3**, 31 (1987).

13. B. B. Sauer, M. kawaguchi, and H. Yu, *Macromolecules* **20**, 2732 (1987).

14. M. A. Bouchiat and J. Meunier, *J. Phys.* **32**, 561 (1971).

Chapter 4

SURFACE WAVE STUDIES OF POLYMER SOLUTIONS

4.1 Introduction

We employed the technique of surface heterodyne light scattering to study thermally-excited waves on the surfaces of polymers solutions. For a given polymer solution, depending on the interaction between the polymers and the solvent, the polymer concentration near the interface can be different from that in the bulk. In principle, three different cases can occur: polymers can be attracted equally to the interface and the bulk; polymers can be repelled from the interface to form a depletion layer; and polymers can be attracted to the interface, forming an adsorbed layer with a polymer concentration at the surface that is higher than that in the bulk.

We have chosen three specific polymer solution systems to study surface waves under each of the above conditions. The first one is polyisobutylene (PIB)/decane, which shows no depletion or adsorption at the interface; the second one is polybromostyrene (PBrS)/toluene for which the polymer solutions have depletion layers near the interface; and the third one is polyethyleneoxide (PEO)/water, which is a system of polymers that are surface active and their solutions have adsorption layers near the interface. The thickness of the depletion and adsorption layers depends on both molecular weight and concentration. The chemical structures of the polymers are shown in Fig. 4.1.

Polyisobutylene (PIB) was purchased from American Polymer Standards Corporation and used without further purification. The molecular weight was $81,600 g/mole$ and M_w/M_n was about 1.2. Decane (Aldrich, 99+%) was used as the solvent for PIB. From the chemical structure of PIB, we expect that the concentration near the surface is equal to the bulk concentration.

Polybromostyrene (PBrS) was provided by the group of Prof. J. Sokolov and

(a)

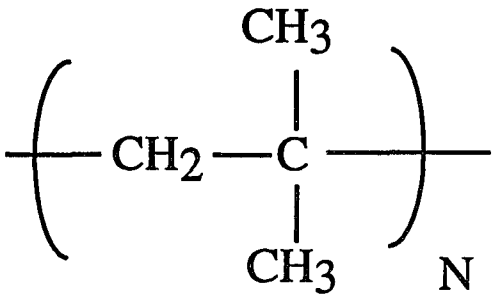

polyisobutylene (PIB), Mw = 81,600

(b)

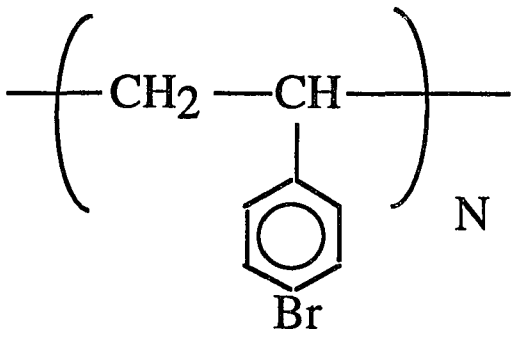

polybromostyrene (PBrS), Mw = 90,000 and Mw = 900,000

(c)

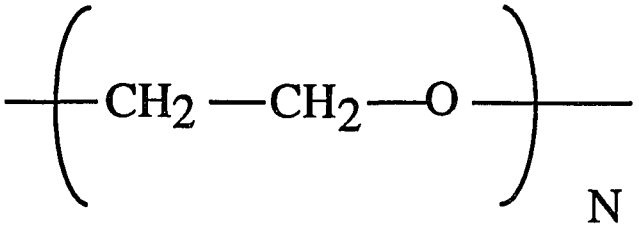

polyethyleneoxide (PEO), Mw = 85,000 and Mw = 1000,000

Fig. 4.1. The chemical structures of the polymers used in this thesis.

M. H. Rafailovich at Queens College of New York. PBrS was prepared by solution bromination of parent batches of polystyrene with narrow distributions ($90K$, $M_w/M_n = 1.04$ and $900K$, $M_w/M_n \leq 1.10$, purchased from Polymer Labs).[1,2] Bromination levels were typically 0.9 Br atoms per styrene monomer, and were determined by mass microanalysis. The toluene (J. T. Baker, A.C.S. reagent grade) is a good solvent for PBrS. Because the surface tension of pure PBrS, which is $39.5 dyne/cm$, is higher than the surface tension of pure toluene, which is $27.5 dyne/cm$, the near surface region is expected to be partially depleted of the polymer component.

Samples of polyethyleneoxide (PEO) with $M_w = 85K$ and $M_w = 1000K$, and both with $M_w/M_n \leq 1.05$, were purchased from American Polymer Standards Corporation and were used without further purification. The water used as the solvent for PEO was house distilled water further purified with a Milli-Q filtering system (Millipore) with one carbon and two ion-exchange filters. Since PEO is surface active, the surface tension for PEO/water is reduced compared to the surface tension of water ($\sim 71.6 dyne/cm$ at room temperature). We find that the surface tension reduction of PEO/water depends on the bulk concentration as well as the molecular weight of the PEO.

By selecting different diffraction spots (orders), we measured the power spectra of a given sample at different wave vectors, k. All the experiments were done at room temperature ($21.3 \pm 0.5^0 C$). We used as many diffraction orders n as possible to ensure good statistics. In our experiments, for the solvents and the low concentration polymer solutions, we were able to measure power spectra with 6-9 different diffraction orders ($100.0 \leq k \leq 600.0 cm^{-1}$). For the high concentration polymer solutions, we found that the scattered intensity from the surface was weak and we could only collect power spectra with 3-4 diffraction orders even with long accumulation times.

Although it can be calculated, the wave vector for different diffraction orders is determined experimentally. Surface waves on the pure solvents are capillary waves, and the experimental power spectra $P(\omega)$ are a convolution of a wave vector

dependent instrumental function and the theoretical spectrum of capillary waves $P_k(\omega)$, as given in Eq. (3.10) and Eq. (2.106). The power spectra of decane ($\sigma = 24.0 dyne/cm$, $\eta_s = 0.83 cp$) and water ($\sigma = 71.6 dyne/cm$, $\eta_s = 1.0 cp$) were fit to Eq. (3.10). Thus, by measuring the power spectra of the pure solvents, we determined the wave vector, k, and the width of the instrumental function, δ_d, in our experiments. These values of k and δ_d were used in the spectral analysis of the polymer solutions since they were measured under the same optical conditions as the pure solvent.

In the first two sections, we present the experimental results for the PIB/decane and PBrS/toluene solution systems. Two theoretical models were used to analyze the power spectra for these two polymer solutions. The first model is the capillary wave theory at the air/liquid interface. The theoretical power spectrum is given by Eq. (2.106) [3] which is a function of surface tension, σ, and the shear viscosity of the bulk, η,

$$P_k(\omega) = \frac{k_B T}{\pi \omega} \frac{\tau_0^2 k}{\rho} \left\{ \frac{Im D(i\omega\tau_0)}{|D(i\omega\tau_0)|^2} \right\} \tag{2.106}$$

where $\tau_0 = \rho/2\eta k^2$. Here, $D(s) = Y + (1+s)^2 - \sqrt{1+2s}$ is the dispersion equation for a simple liquid surface, with $Y = \sigma\rho/4\eta^2 k$. The experimental power spectrum is

$$P(\omega) = \sum_{\Delta k=-75}^{75} (1/[(\Delta k/\delta_d)^2 + 1]^2) \cdot P_k(\omega, k + \Delta k) \tag{4.1}$$

where $P_k(\omega)$ is given by Eq. (2.106). The physical parameters obtained from the fits using Eq. (4.1) were the surface tension, σ, and the viscosity of the bulk, η. In this case, the polymer solutions are treated as Newtonian fluids. Since the polymer solutions change from being viscous fluids to viscoelastic fluids when the polymer concentration is increased, we expect that the capillary wave theory is not sophisticated enough to describe their surface wave behavior in a broad concentration range.

The second model is the theory proposed by Harden *et al.* [4] for polymer solutions, which treats polymer solutions as viscoelastic fluids. The theoretical

power spectrum is given by Eq. (2.147),

$$P_k(\omega) = \frac{8k_BTRe[\eta(\omega)]k^3}{|D(k,\omega)|^2}\left\{1 + \frac{1}{2Re[\alpha(k,\omega)]} - 2Re\left(\frac{1}{1+\alpha(k,\omega)}\right)\right\} \quad (2.147)$$

where $D(k,\omega)$ is given by Eq. (2.125),

$$D(k,\omega) = \left(i\omega + 2\nu(\omega)k^2\right)^2 - 4\nu(\omega)^2k^4\left(1 + \frac{i\omega}{\nu(\omega)k^2}\right)^{1/2} + \sigma k^3/\rho \quad (2.125)$$

The important physical parameters in Eq. (2.147) are the surface tension, σ, and the complex modulus, $G^*(\omega)$. The experimental power spectrum is

$$P(\omega) = \sum_{\Delta k=-75}^{75} (1/[(\Delta k/\delta_d)^2 + 1]^2) \cdot P_k(\omega, k + \Delta k) \quad (4.2)$$

where $P_k(\omega)$ is given by Eq. (2.125) and Eq. (2.147). For polymer solutions within the Maxwell model,[5] the complex shear modulus, $G^*(\omega)$, is

$$G^*(\omega) = \frac{iG_0\omega\tau}{(1 + i\omega\tau)} \quad (2.126)$$

where G_0 is the transient modulus of the polymer network and τ is the stress relaxation time of the medium. Note that G_0 and τ increase as the polymer concentration is increased in the polymer solution, indicating a stronger viscoelastic behavior of the solution. The power spectrum is a function of the surface tension, σ, the transient modulus, G_0, and the relaxation time, τ. If $\tau \ll 1/\omega$, we have

$$\eta \approx \eta_s + G_0 * \tau \quad (4.3)$$

The physical parameters obtained from the fits using Eq. (4.2) are the surface tension, σ, the transient modulus, G_0, and the relaxation time, τ.

As discussed in Chapter 2, the theory is consistent with the capillary wave theory for simple liquids, as given in Eq. (2.106), when the polymer concentration is low. Thus, we expect that the surface waves for low concentration polymer solutions are well described by both theories.

The experimental power spectra for the PIB/decane and PBrS/toluene solution systems were fit to both Eq. (4.1) and Eq. (4.2). We found that for these polymer

solution systems, both Eq. (4.1) and Eq. (4.2) gave good fits to the experimental power spectra over the entire range of polymer concentrations. The fits to the power spectra using both theories have very similar shapes. However, the physical parameters obtained from the spectral analysis using these two theories are different at high polymer concentrations. The theoretical model proposed by Harden *et al.* [4] for polymer solutions extracts more accurate physical parameters when compared to those obtained from independent measurements at high concentrations.

In the last section, we present the experimental results for the PEO/water solutions with molecular weights $85K$ and $1000K$. Two theoretical models were used for the spectral analysis. The first model is the theory for polymer solutions[4], Eq. (4.2). Three physical parameters are involved in this theory with the Maxwell model. They are the surface tension, σ, the transient modulus, G_0, and the relaxation time, τ. The use of this theory for the spectral analysis for PEO/water solutions implies that the adsorption layers have no effect on the surface waves of the PEO/water solutions.

The proper model for the PEO/water solutions is to treat the polymer solutions as bulk fluids with monolayer-covered interfaces. At low polymer concentrations, the bulk solutions behave as simple Newtonian fluids. In this case, we can treat the PEO/water interface as a monolayer-covered interface between air and a simple liquid. Thus, the second theoretical model is the capillary wave theory for monolayer-covered interfaces. The theoretical power spectrum is given by Eqs. (2.104) and (2.105):[6]

$$P_k(\omega) = -k_B T\tau_0^2 k/(\pi\omega\rho) Im\{-\omega^2\tau_0^2/D(\omega) + [\varepsilon\rho/(4\eta^2 k) + ik\kappa\omega\tau_0/(2\eta)][(1+i2\omega\tau_0)^{1/2} - 1]/D(\omega)\} \tag{2.104}$$

where

$$D(\omega) = -\omega^2\tau_0^2[(1+i\omega\tau_0)^2 + \sigma\rho/(4\eta^2 k) - (1+i2\omega\tau_0)^{1/2}] + (\varepsilon + i\omega\kappa)\eta/(4\eta^2 k)\{-\omega^2\tau_0^2(1+i2\omega\tau_0)^{1/2} + \rho(\sigma + i\omega\mu)/(4\eta^2 k)[(1+i2\omega\tau_0)^{1/2} - 1]\} - i\mu k\omega^3\tau_0^3/(2\eta) \tag{2.105}$$

and where $\tau_0 = \rho/2\eta k^2$, and where ρ and η are the density and viscosity of the bulk solutions, respectively.

The experimental power spectrum is,

$$P(\omega) = \sum_{\Delta k=-75}^{75} (1/[(\Delta k/\delta_d)^2 + 1]^2) \cdot P_k(\omega, k + \Delta k) \tag{4.4}$$

where $P_k(\omega)$ is given by Eqs. (2.104) and (2.105). The physical parameters in Eq. (4.4) are the surface tension, σ, the transverse viscosity, μ, the surface longitudinal elasticity, ε, and the surface longitudinal viscosity, κ. As in earlier studies, the transverse viscosity, μ, was assumed to be negligible.[7-10] By fixing the surface tension to the value measured with the du Nouy ring method, we can estimated the surface longitudinal elasticity, ε, and the surface longitudinal viscosity, κ, from the spectral analysis. This model is applied to the $85K$ PEO solutions.

In the next three sections, we present the experimental results for each polymer solution system and discuss the parameters obtained from the fits using these theories. All the experimental power spectra are shown with the fits to the theory for polymer solutions, Eq. (4.2). For the $85K$ PEO solutions at high concentrations, the experimental power spectra are shown with both the fits to Eq. (4.2) and the fits to Eq. (4.4).

4.2 Surface Waves at Air/solution Interfaces of Polyisobutylene (PIB)/decane

The first polymer solution system we studied[11a] was polyisobutylene (PIB)/decane. A master polymer solution of concentration $10.3g/dl$ was prepared by dissolving $1.03g$ of PIB in $10cc$ decane. The concentration of the polymer solutions was then diluted by adding pure decane.

Figures 4.2 - 4.3 show the experimental power spectra of PIB/decane solutions at bulk concentrations of $8.0g/dl$ and $0.5g/dl$ for the diffraction orders 2-4, along with the fits to Eq. (4.2). Figures 4.4(a) and 4.4(b) show the experimental power spectra of a PIB/decane solution at a concentration of $4.0g/dl$ for the diffraction

orders 2-8 along with the fits to Eq. (4.2). As we can see, the experimental power spectra are well described by Eq. (4.2). From the figures, one can see that the peak positions of the power spectra move faster with increasing wave vector, k, when the concentration of the PIB/decane solutions is decreased. For samples with concentrations higher than $8.0g/dl$, we found that only three or fewer power spectra, of diffraction orders 2-4, could be measured.

Starting from a concentration of $8.0g/dl$, we measured the power spectra for eight different concentrations of PIB/decane solutions, $8.0g/dl$, $5.5g/dl$, $4.5g/dl$, $4.0g/dl$, $2.6g/dl$, $1.2g/dl$, $0.8g/dl$ and $0.5g/dl$. The surface tensions of all the polymer solutions were measured with the du Nouy ring method and were found to have the same value: $\sigma = 24.0 \pm 0.12 dyne/cm$. This indicates that there is no preferential absorption of the polymer at the surface.[12] Their viscosities of the bulk were also measured with a Couette viscometer (Contraves).

The peak frequency, f_p, and the full-width at half-maximum, Δf_{exp}, can be determined from the fit to the power spectrum for a given sample at each wave vector. In Figs. 4.5(a) and 4.5(b), we plot the peak frequency, f_p, and the full-width at half-maximum, Δf_{exp}, as functions of the bulk concentration in order to show how the two variables scale with bulk concentration at the diffraction orders $n = 2 - 5$. It is noticeable that Δf_{exp} increases as the concentration is increased, indicating an increase in the viscosity of the polymer solution. We can also see that f_p decreases as the bulk concentration is increased, even though the surface tension is constant in this concentration range. This is partially due to the damping effect, since Y changes from ~ 220 to ~ 1.4 for $\rho = 0.73g/cm^3$ and $k = 200cm^{-1}$ when the bulk concentration is changed from $0.5g/dl$ to $8.0g/dl$.

We can find the exponent of the wave vector scaling, $f_p \sim k^\alpha$. For all samples, α is obtained from the slope of the fit of $ln(f_p)$ vs $ln(k)$. If we treat the PIB/decane solutions as simple liquids in this concentration range, we can simulate the capillary wave power spectra using Eq. (2.106). In this expression, we use the surface tension measured with the du Nouy ring method and the viscosity measured with a Couette viscometer to determine the parameter α. Our results are plotted in Fig. 4.6. We

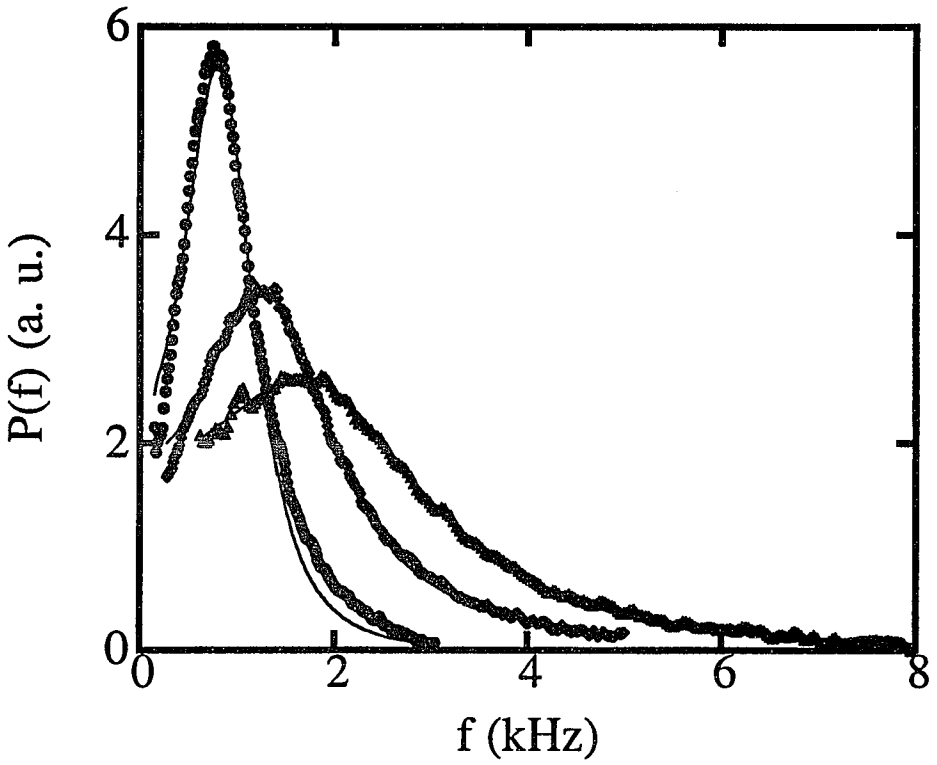

Fig. 4.2. Power spectra of the 8.0 g/dl concentration PIB/decane at the diffraction orders 2-4, corresponding to k = 105.1, 160.7, and 218.2 cm^{-1}. They are rescaled to have the same baseline. The solids lines are the fits using Eq. (4.2). The symbols correspond to: ● n=2; ◆ n=3; and ▲ n=4.

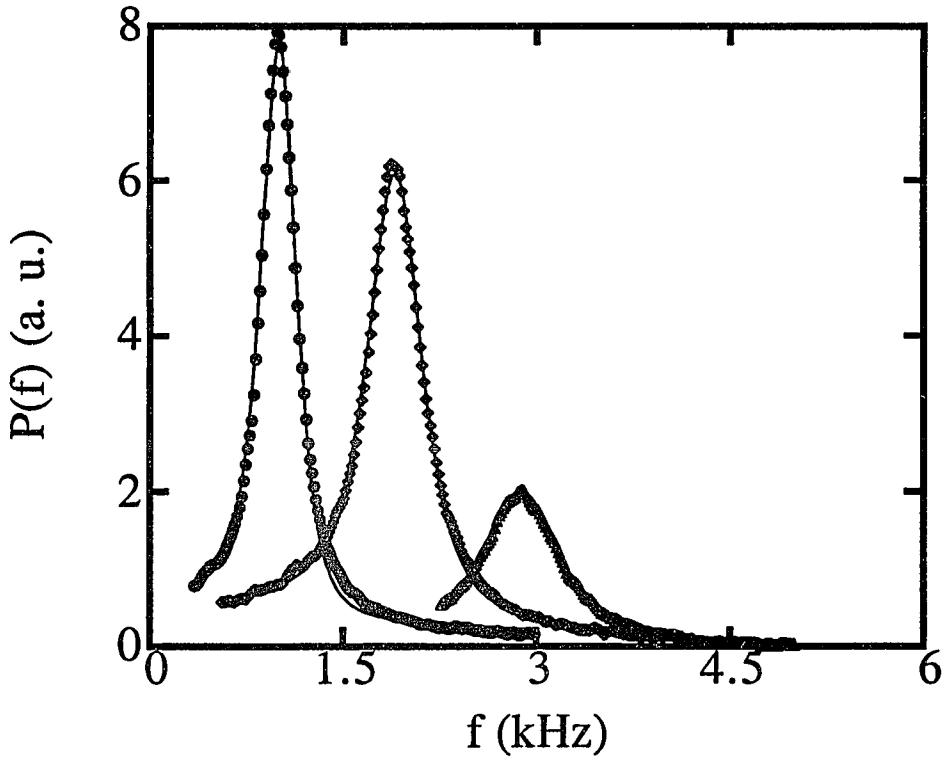

Fig. 4.3. Power spectra of the 0.5 g/dl concentration PIB/decane at the diffraction orders 2-4, corresponding to k = 105.1, 160.7, and 218.2 cm^{-1}. They are rescaled to have the same baseline. The solids lines are the fits using Eq. (4.2). The symbols correspond to: ● n=2; ◆ n=3; and ▲ n=4.

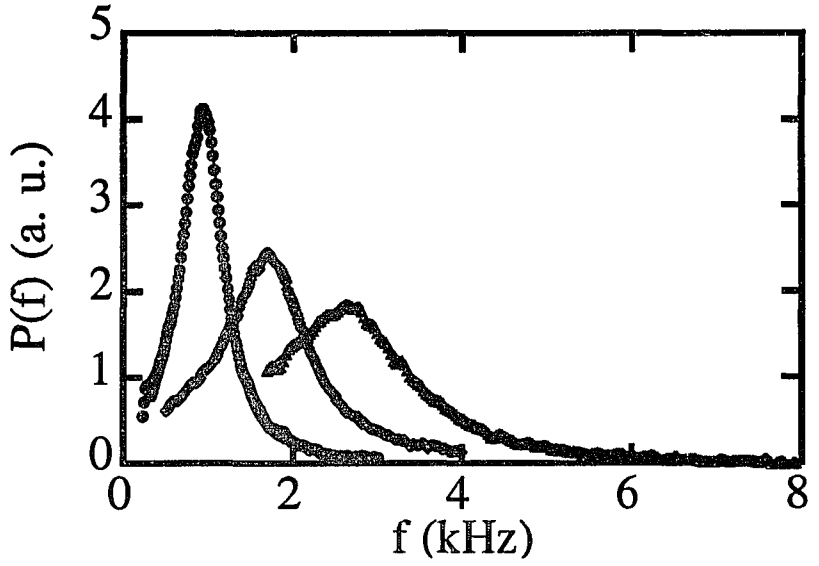

Fig. 4.4(a). Power spectra of the 4.0 g/dl concentration PIB/decane at the diffraction orders 2-4, corresponding to k = 105.1, 160.7, and 218.2 cm^{-1}. They are rescaled to have the same baseline. The solids lines are the fits using Eq. (4.2). The symbols correspond to: ● n=2; ◆ n=3; and ▲ n=4.

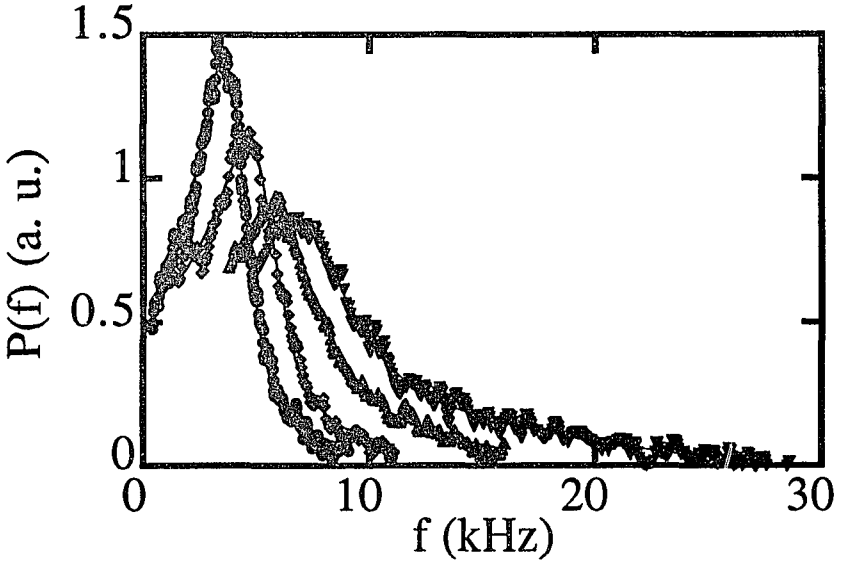

Fig. 4.4(b). Power spectra of the 4.0 g/dl concentration PIB/decane at the diffraction orders 5-8, corresponding to k = 276.3, 332.3, 388.4, and 442.0 cm^{-1}. They are rescaled to have the same baseline. The solids lines are the fits using Eq. (4.2). The symbols correspond to: ● n=5; ◆ n=6; ▲ n=7; and ▼ n=8.

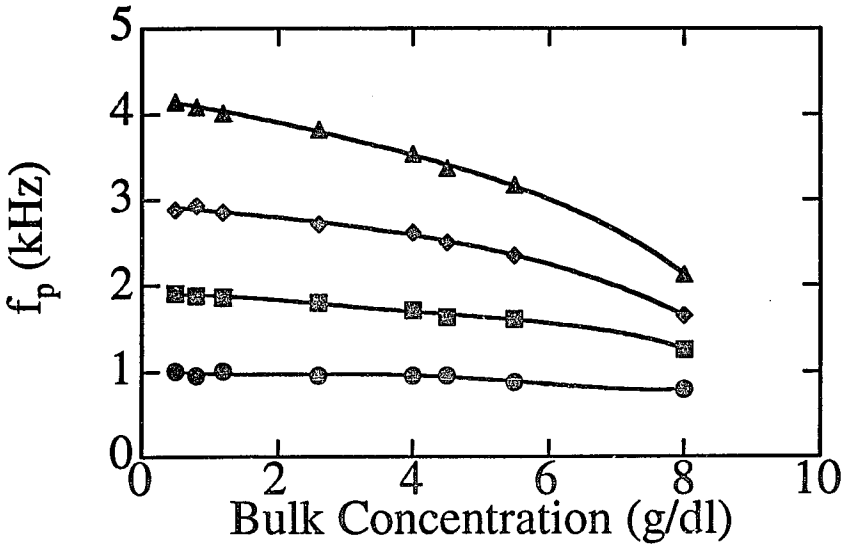

Fig. 4.5(a). Peak frequency, f_p, *vs.* bulk concentration for PIB/decane at the diffraction orders 2-5. The smooth curves are drawn through the data points for clarity. The symbols correspond to: ● n=2; ■ n=3; ◆ n=4; and ▲ n=5.

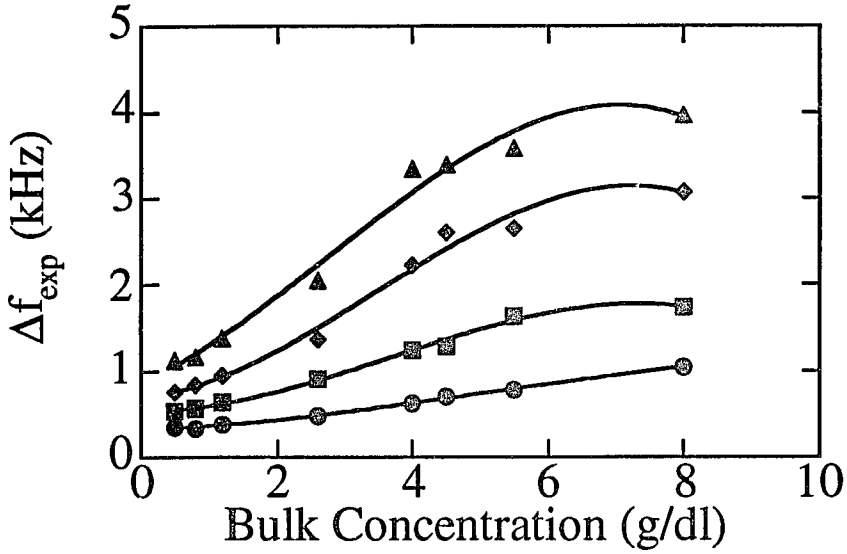

Fig. 4.5(b). Experimental frequency width, Δf_{exp}, *vs.* bulk concentration for PIB/decane at the diffraction orders 2-5. The smooth curves are drawn through the data points for clarity. The symbols correspond to: ● n=2; ■ n=3; ◆ n=4; and ▲ n=5.

can clearly see that the behavior of α predicted by the capillary wave theory is different from that observed experimentally. For the highest polymer concentration (8.0 g/dl), α is found to be 1.27 by the capillary wave description, while α is found to be 1.0 from the experiment. Thus, we can see that by treating the polymer solution as a simple liquid, it is not possible to fully explain the experimental results. For comparison, we have also calculated α using Eq. (2.125) in the limit that the storage modulus for a polymer solution is zero, and $\eta(\omega) = \eta$, the measured viscosity of the solution. We find that α calculated in this manner is the same as that calculated using the capillary wave theory for a simple liquid, as shown in Fig. 4.6. Figure 4.6 gives some indication that the viscoelasticity of PIB/decane solutions is important to analyze our experimental data properly.

The experimental power spectra of PIB/decane solutions can also be well described by a Lorentzian function.[11a] We find that the peak frequencies determined from the fits to the Lorentzian function are very close to those determined from the fits to Eq. (4.2). Therefore, the values of α can be calculated using the fit to the Lorentzian function.[11a] However, the fact that α changes from 1.5 to 1.0 with increasing bulk concentration is not sufficient to conclude that the surface waves cross over from capillary waves to elastic waves.[11b] Instead, this change is partially due to the deviation of the peak frequencies of the power spectra from the resonant frequencies for high viscosity fluids.

To pursue further the surface light scattering results, in Figs. 4.7(a) and 4.7(b), we plot the surface tension, σ, and the viscosity, η, from the spectral fits using the capillary wave theory, Eq. (4.1), and the theory for polymer solutions, Eq. (4.2), as functions of the bulk concentration. We also compare the values obtained from the fits with those obtained from the independent measurements. The values of the viscosities obtained from the fits to Eq. (4.2) are calculated using Eq. (4.3), $\eta \approx \eta_s + G_0 * \tau$, since the relaxation time τ is $\sim 1 - 3 \times 10^{-5} \ll 1/\omega$. The values of the surface tension and the viscosity are obtained by averaging the values obtained from the individual fits of 4 to 6 power spectra, using the diffraction orders $n = 2 - 7$. At low concentrations ($< 4.0 g/dl$), both theories give good results for

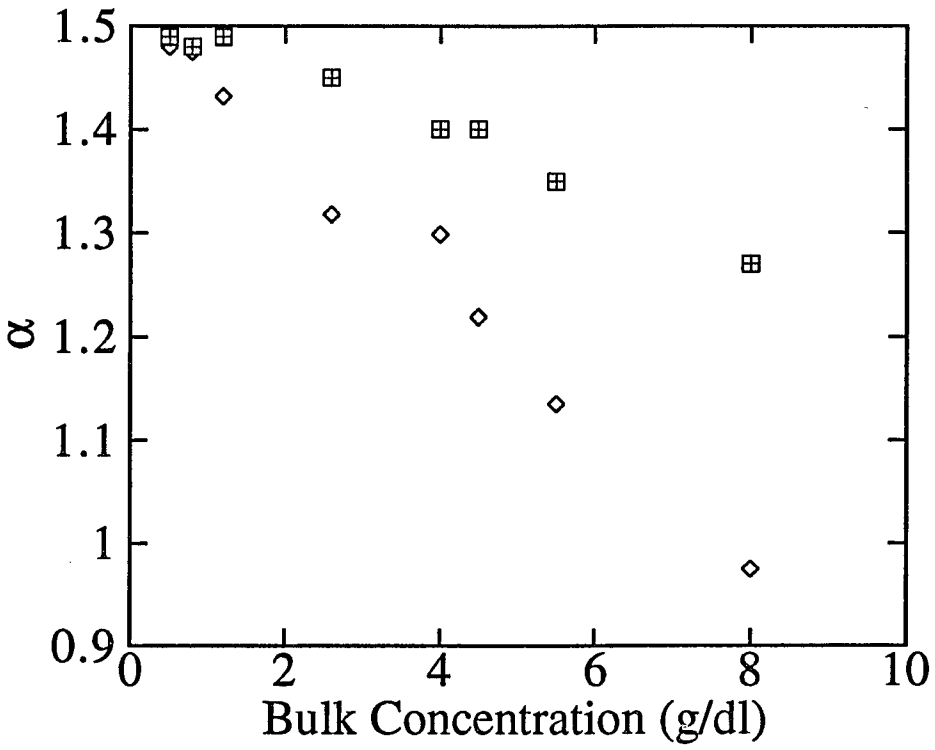

Fig. 4.6. Plot showing the relationship between α, obtained from the fits of $\ln(f_p)$ *vs.* $\ln(k)$, and the bulk concentration of PIB/decane. The symbols correspond to: □ the theory for polymer solutions; + the capillary wave theory; and ◇ experimental.

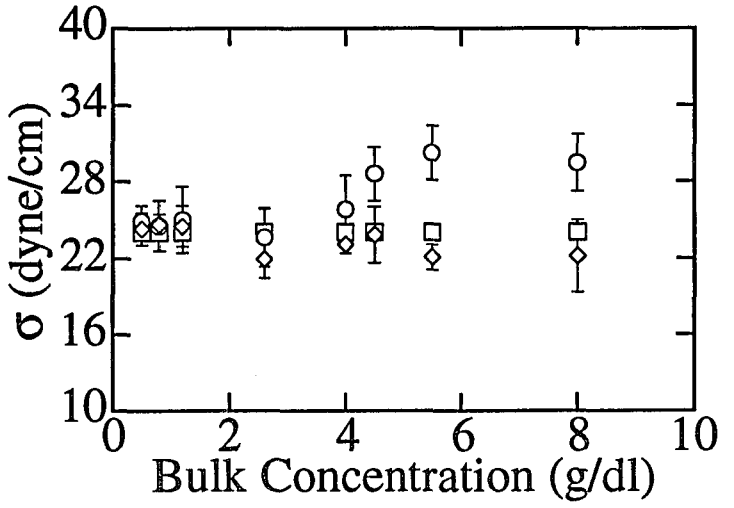

Fig. 4.7(a). Surface tension, σ, *vs.* bulk concentration of PIB/decane. The symbols correspond to: □ data obtained from the du Nouy ring method; o data obtained from the spectral fits using the capillary wave theory, Eq. (4.1); and ◇ data obtained from the spectral fits using the theory for polymer solutions, Eq. (4.2).

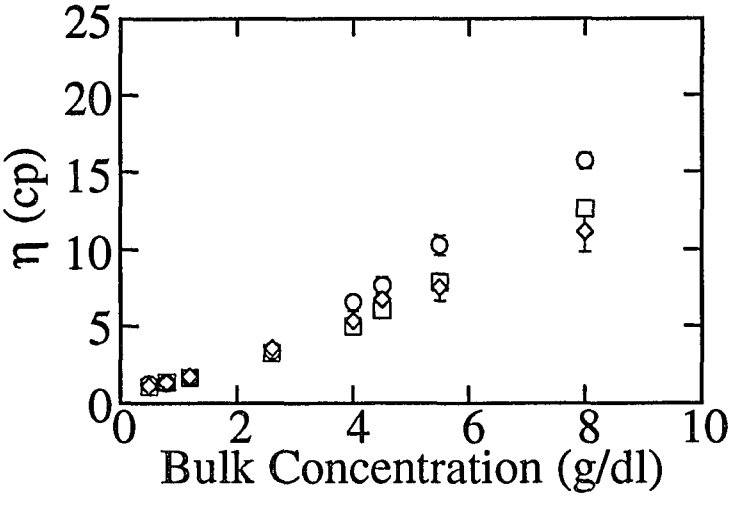

Fig. 4.7(b). Viscosity, η, *vs.* bulk concentration of PIB/decane. The symbols correspond to: □ data obtained from a Couette viscometer; o data obtained from the spectral fits using the capillary wave theory, Eq. (4.1); and ◇ data obtained from the spectral fits using the theory for polymer solutions, Eq. (4.2).

the surface tension, σ, and the viscosity, η. However, it can be seen that, at high bulk concentrations ($> 4.0g/dl$), the results obtained from the theory for polymer solutions are better than those obtained from the capillary wave theory.

To conclude, we have demonstrated that the technique of surface heterodyne light scattering can be used to probe the surface properties of polymer solutions. We have found that the capillary wave theory can not fully describe our experimental results for the PIB/decane solutions over the entire concentration range. The theory for polymer solutions[4] which treats the polymer solutions as viscoelastic fluids is a more adequate model for the PIB/decane solution system at relatively high concentrations and gives better results for the surface tensions and viscosities. The values of the surface tensions and the viscosities obtained from the fits using both theories agree with each other only for the low concentration polymer solutions.

4.3 Molecular Weight Dependence of Surface Waves at Air/solution Interfaces of Polybromostyrene (PBrS)/toluene

In the last section, we studied the polymer solution system, PIB/decane with $M_w = 81K$, for which the concentration near the air/solution interface is equal to the bulk concentration. In this section, the polymer solution system for our studies is the depletion layer type.[13] Thus, the polymer concentration near the solution interface is expected to be less than the bulk concentration due to the interaction between the polymers and the solvent. We also study the effects of the molecular weight on surface waves of polymer solutions. For these two reasons, we have chosen polybromostyrene (PBrS)/toluene solutions with $M_w = 90K$ and $M_w = 900K$ as the systems to study. This polymer solution system has been studied by the technique of x-ray scattering.[2] Here, we use the technique of the surface heterodyne light scattering to probe the surface waves at the PBrS/toluene interfaces for low molecular weight ($M_w = 90K$) and high molecular weight ($M_w = 900K$). The effects of the depletion layers on the surface waves of the PBrS/toluene solutions will be addressed in this section.

4.3.1 Polybromostyrene (PBrS) with Molecular Weight 90K

For the PBrS/toluene solutions with $M_w = 90K$, we studied the surface waves at the air/solution interface in the bulk concentration range from $20.0g/dl$ to $0.5g/dl$. Figures 4.8 - 4.10 show the experimental power spectra of PBrS/toluene solutions at bulk concentrations of $20.0g/dl$, $11.0g/dl$, and $3.0g/dl$ for the diffraction orders 2-4, along with the fits to Eq. (4.2). All the experimental power spectra are well fit with Eq. (4.2). We could only measure the power spectra up to $20.0g/dl$ bulk concentration of the PBrS/toluene solutions with $M_w = 90K$; at higher concentrations, we found that the surface waves are overdamped so that their power spectra have no defined peaks.

The surface tensions of all of the PBrS/toluene solutions with $M_w = 90K$ were obtained with the du Nouy ring method and were: $\sigma = 27.5 \pm 0.25 dyne/cm$. Their viscosities of the bulk were measured with a Couette viscometer (Contraves). From the viscosity results, we found that the chain overlap concentration, c^*, as defined in Eq. (2.20), is about $3.4g/dl$. Below c^*, the surface waves of the polymer solutions are expected to be well into the capillary wave regime.

We determined the peak frequency, f_p, and the full-width at half-maximum, Δf_{exp}, from the fits to the power spectra for all samples using diffraction orders $n = 2 - 5$; the concentration dependences are summarized in Figs. 4.11(a) and 4.11(b). These results are similar to those of the PIB/decane solutions, as shown in Figs. 4.5(a) and 4.5(b). The peak frequency decreases as the bulk concentration is increased, while the frequency width increases.

The more important results are the surface tension, σ, and the viscosity, η, obtained from the spectral analysis, since we can compare them with those obtained from the independent measurements. In Figs. 4.12(a) and 4.12(b), we plot the surface tension, σ, and the viscosity, η, obtained from the spectral fits using both the capillary wave theory, Eq. (4.1), and the theory for polymer solutions, Eq. (4.2), as functions of the bulk concentration. For comparison, we also plot the surface tension measured with the du Nouy ring method and the viscosity measured with a

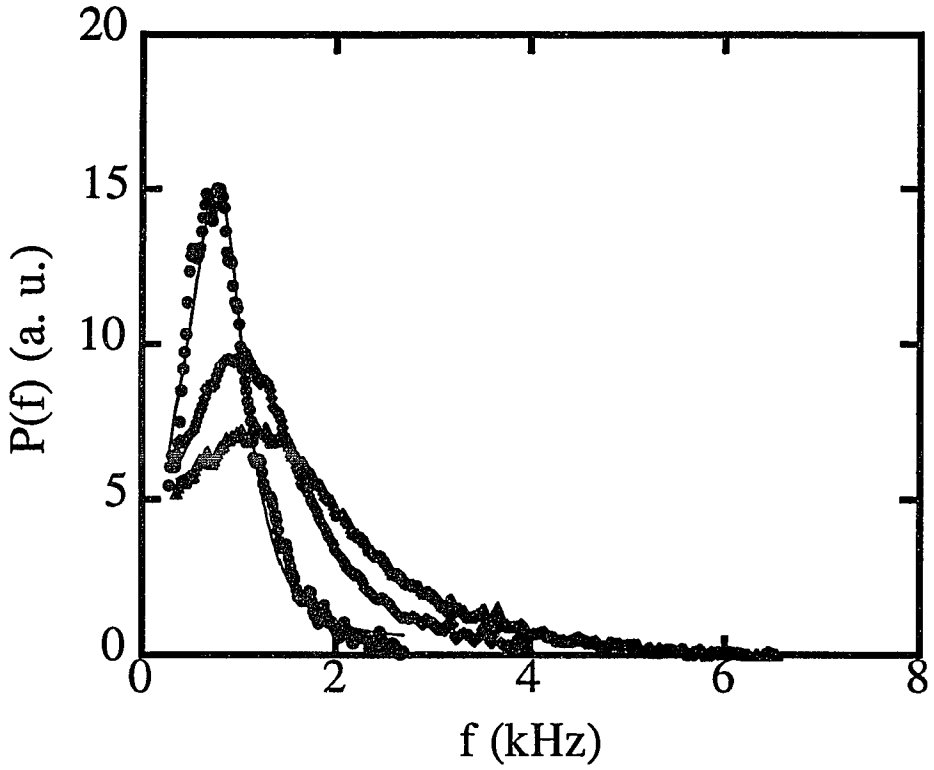

Fig. 4.8. Power spectra of the 20.0 g/dl concentration PBrS/toluene with M_W = 90K at the diffraction orders 2-4, corresponding to = 94.1, 144.8, and 193.9 cm^{-1}. They are rescaled to have the same baseline. The solids lines are the fits using Eq. (4.2). The symbols correspond to: ● n=2; ◆ n=3; and ▲ n=4.

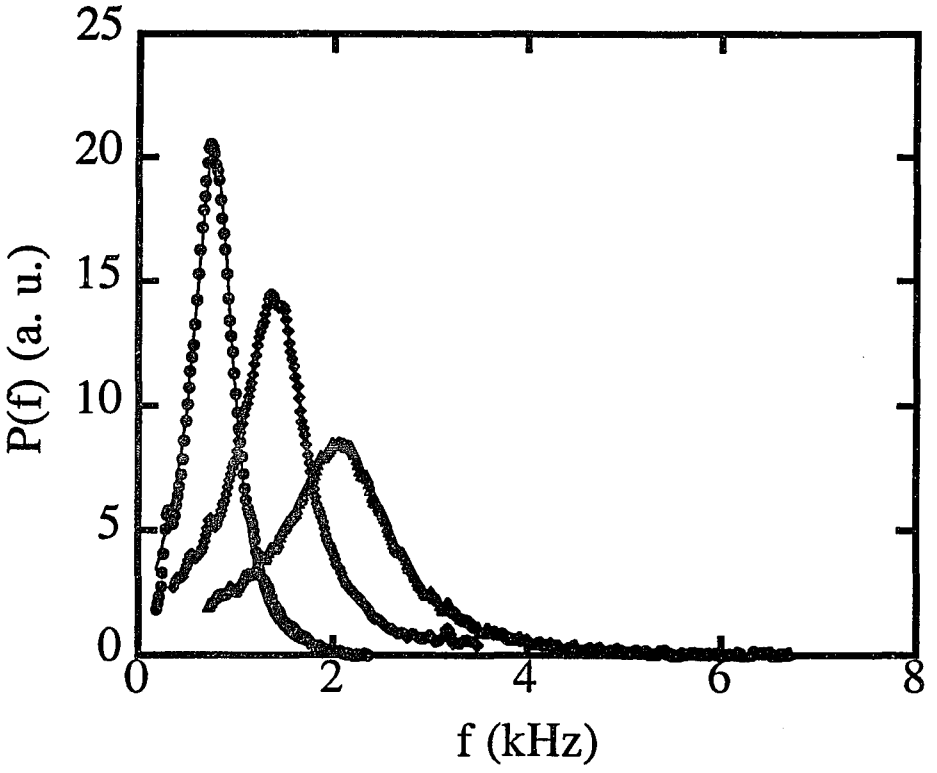

Fig. 4.9. Power spectra of the 11.0 g/dl concentration PBrS/toluene with M_W = 90K at the diffraction orders 2-4, corresponding to k = 94.1, 144.8, and 193.9 cm^{-1}. They are rescaled to have the same baseline. The solids lines are the fits using Eq. (4.2). The symbols correspond to: ● n=2; ◆ n=3; and ▲ n=4.

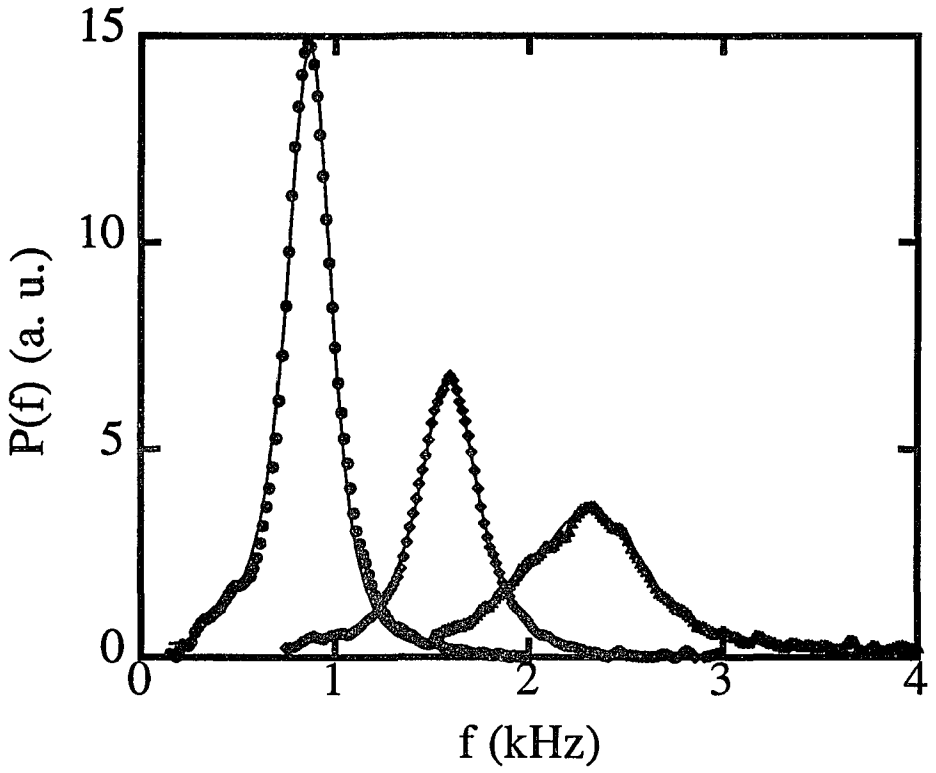

Fig. 4.10. Power spectra of the 3.0 g/dl concentration PBrS/toluene with M_W = 90K at the diffraction orders 2-4, corresponding to k = 94.1, 144.8, and 193.9 cm^{-1}. They are rescaled to have the same baseline. The solids lines are the fits using Eq. (4.2). The symbols correspond to: ● n=2; ◆ n=3; and ▲ n=4.

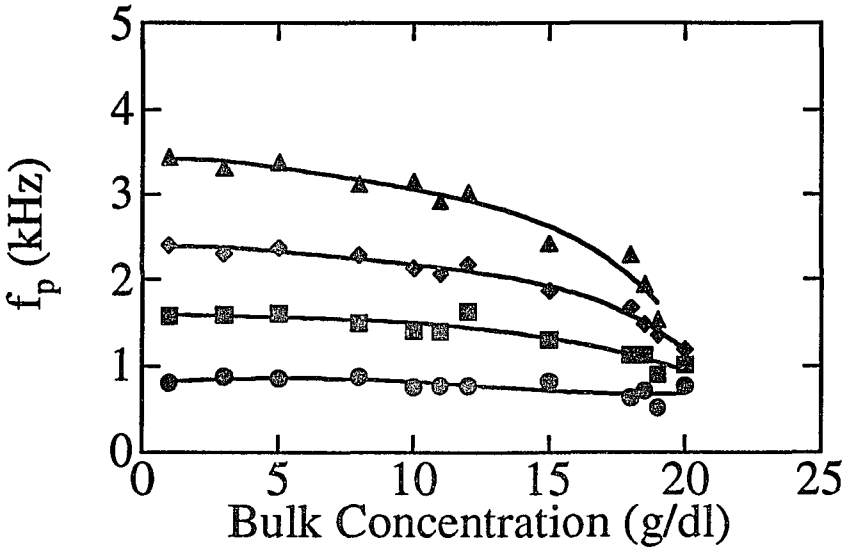

Fig. 4.11(a). Peak frequency, f_p, *vs.* bulk concentration of PBrS/toluene with M_W = 90K at the diffraction orders 2-5. The smooth curves are drawn through the data points for clarity. The symbols correspond to: ● n=2; ■ n=3; ◆ n=4; and ▼ n=5.

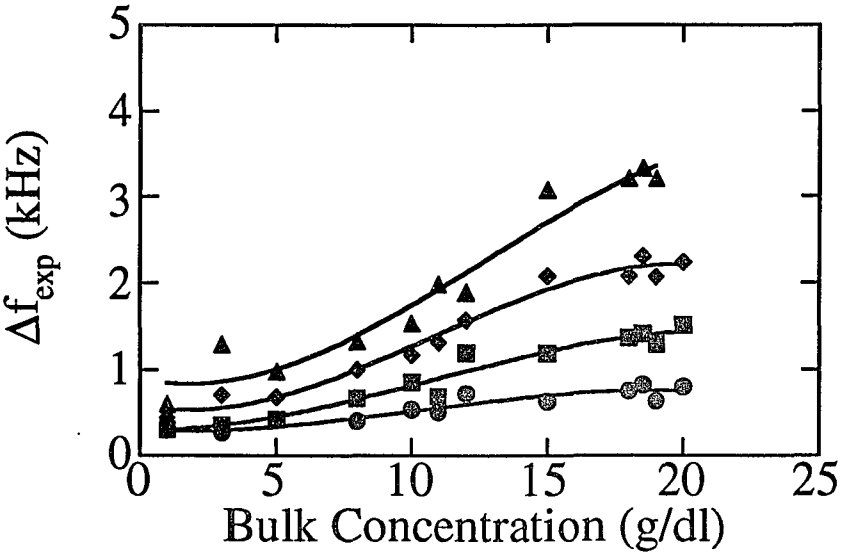

Fig. 4.11(b). Experimental frequency width, Δf_{exp}, *vs.* bulk concentration of PBrS/toluene with M_W = 90K at the diffraction orders 2-5. The smooth curves are drawn over the data points for clarity. The symbols correspond to: ● n=2; ■ n=3; ◆ n=4; and ▲ n=5.

Couette viscometer. The values of the viscosities obtained from the fits to Eq. (4.2) are calculated using Eq. (4.3) since the relaxation time, τ, is $\sim 1 - 3 \times 10^{-5} \ll 1/\omega$ over the entire concentration range. The values of the surface tension and the viscosity are obtained by averaging the values obtained from the individual fits of 4 to 6 power spectra, using the diffraction orders $n = 2 - 7$. It is evident that, within the experimental error, the values of the surface tension and the viscosity obtained from the spectral analysis using both theories agree well with those obtained from the independent measurements over the entire concentration range. Thus, for the PBrS/toluene solutions with $M_w = 90K$, the surface wave behavior at the solution interfaces is well described by both the capillary wave theory and the theory for the polymer solutions. Therefore, the surface waves of these polymer solutions are still in the capillary wave regime.

One of the assumptions in the theory for polymer solutions is that there are no gradients of polymer concentration near the interface. Consistent with this assumption, the spectral results indicate that the depletion layers of the polymer solutions have no effect on the surface waves at the solution interface. This is understandable in terms of the thickness of the depletion layer for the PBrS/toluene solutions with $M_w = 90K$. At the highest polymer concentration, $20.0g/dl$, this can be estimated using Eq. (2.22) and is found to be 20 Å, assuming the monomer size is ~ 2 Å. Since the typical wavelength of the waves probed by surface light scattering is about hundred μm, this very small depletion layer is probably not large enough to affect the hydrodynamic behavior at the interface of these polymer solutions.

To conclude, the surface waves at the PBrS/toluene solutions with $M_w = 90K$ can be interpreted by both the capillary wave theory and the theory for polymer solutions over the entire concentration range. The depletion layers of the PBrS/toluene solutions have no effect on the surface waves at the solution interface.

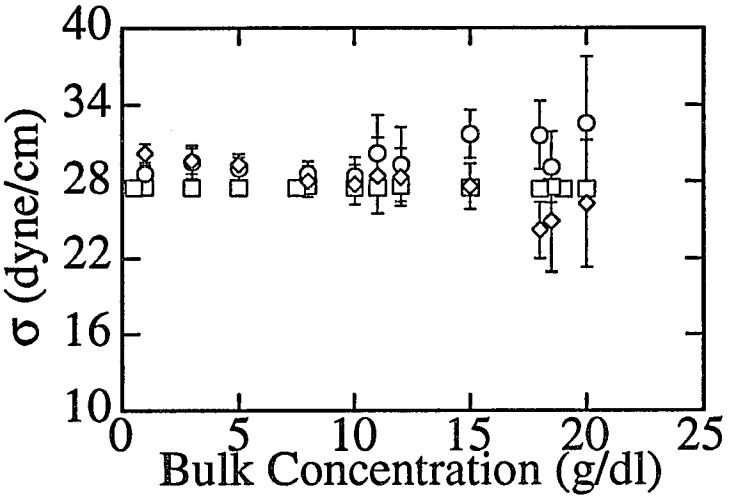

Fig. 4.12(a). Surface tension, σ, *vs.* bulk concentration of PBrS/toluene with $M_W = 90K$. The symbols correspond to: □ data obtained from the du Nouy ring method; o data obtained from the spectral fits using the capillary wave theory, Eq. (4.1); and ◇ data obtained from the spectral fits using the theory for polymer solutions, Eq. (4.2).

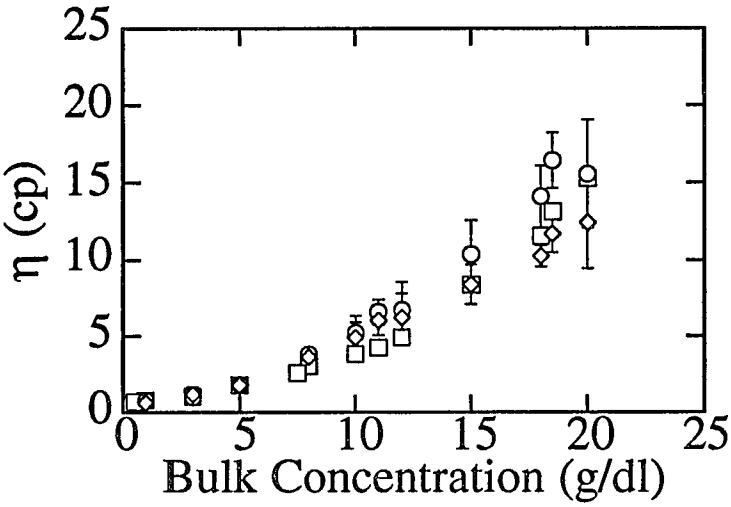

Fig. 4.12(b). Viscosity, η, *vs.* bulk concentration of PBrS/toluene with $M_W = 90K$. The symbols correspond to: □ data obtained from a Couette viscometer; o data obtained from the spectral fits using the capillary wave theory, Eq. (4.1); and ◇ data obtained from the spectral fits using the theory for polymer solutions, Eq. (4.2).

4.3.2 Polybromostyrene (PBrS) with Molecular Weight 900K

For the PBrS/toluene solutions with $M_w = 900K$, the highest concentration accessible to our surface light scattering experiments was found to be $7.0g/dl$. We also measured the viscosities for the PBrS/toluene solutions with $M_w = 900K$ using a Couette viscometer; from this, we found the chain overlap concentration c^* to be $1.11g/dl$. Therefore, the concentration range for our surface wave studies for this polymer system was chosen to be from $7.0g/dl$ to $0.5g/dl$; this covers the regime from high concentration to dilute concentration. Figures 4.13 - 4.15 show the experimental power spectra of PBrS/toluene solutions at bulk concentrations of $7.0g/dl$, $4.0g/dl$, and $0.5g/dl$ for the diffraction orders 2-4, along with the fits to Eq. (4.2). As we can see, the experimental power spectra are well described by Eq. (4.2). We can also see that the power spectra at a bulk concentration of $7.0g/dl$ are very broad; this is due to the high viscosity, $\eta = 43.28cp$. If we treat the $7.0g/dl$ PBrS/toluene solution as a simple Newtonian fluid, we can generate the power spectrum for capillary waves using Eq. (4.1) with $\sigma = 27.5dyne/cm$ and $\eta = 43.28cp$. Figure 4.16 compares the theoretical power spectrum, using Eq. (4.1) at $k = 97.4cm^{-1}$ and $\delta_d = 12.1$, with the experimental power spectrum for the $7.0g/dl$ concentration PBrS/toluene solution with $M_w = 900K$. We can see that the theoretical power spectrum is overdamped, while the experimental one indicates that the surface waves still propagate at this high concentration. Similar results were also seen by other workers.[14] These results are presumably due to the viscoelastic properties of the sample; we cannot simply treat high concentration PBrS/toluene solutions with $M_w = 900K$ as simple Newtonian fluids.

To clearly show the effect of the bulk viscoelasticity on the surface waves of the PBrS/toluene solutions with $M_w = 900K$, in Figs. 4.17(a) and 4.17(b), we plot the bulk concentration dependence of the surface tension, σ, and the viscosity, η, obtained from the spectral fits using the capillary wave theory, Eq. (4.1), and the theory for polymer solutions, Eq. (4.2). The values of the viscosities obtained from the fits using Eq. (4.2) are calculated using Eq. (4.3), $\eta \approx \eta_s + G_0 * \tau$, since

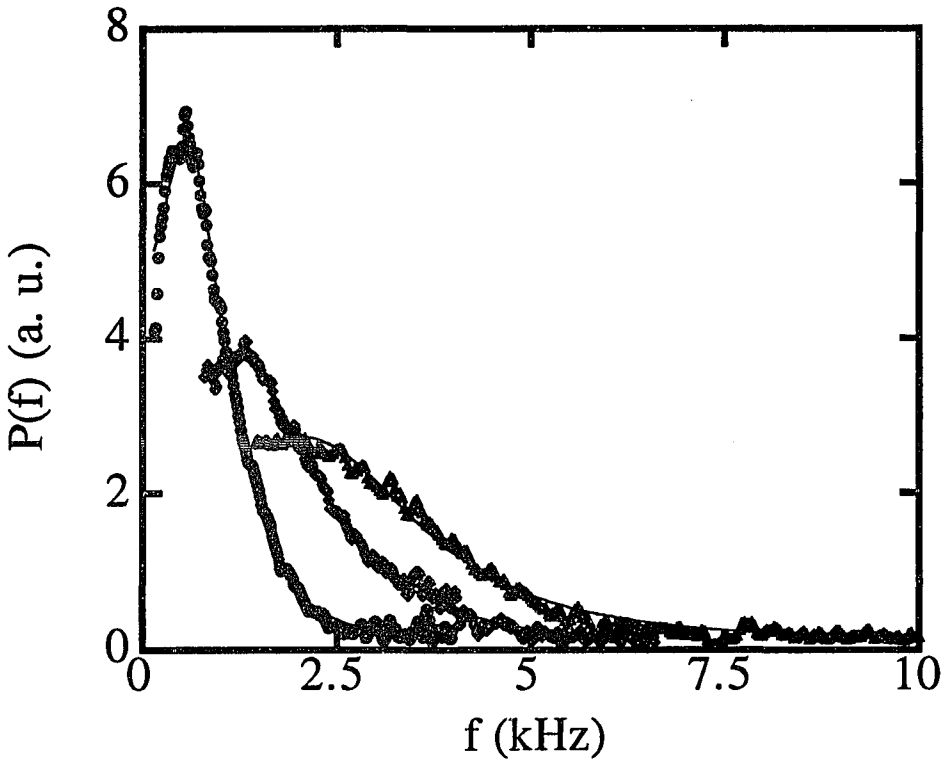

Fig. 4.13. Power spectra of the 7.0 g/dl concentration PBrS/toluene with M_W = 900K at the diffraction orders 2-4, corresponding to k = 97.4, 146.1, and 194.5 cm^{-1}. They are rescaled to have the same baseline. The solids lines are the fits using Eq. (4.2). The symbols correspond to: ● n=2; ◆ n=3; and ▲ n=4.

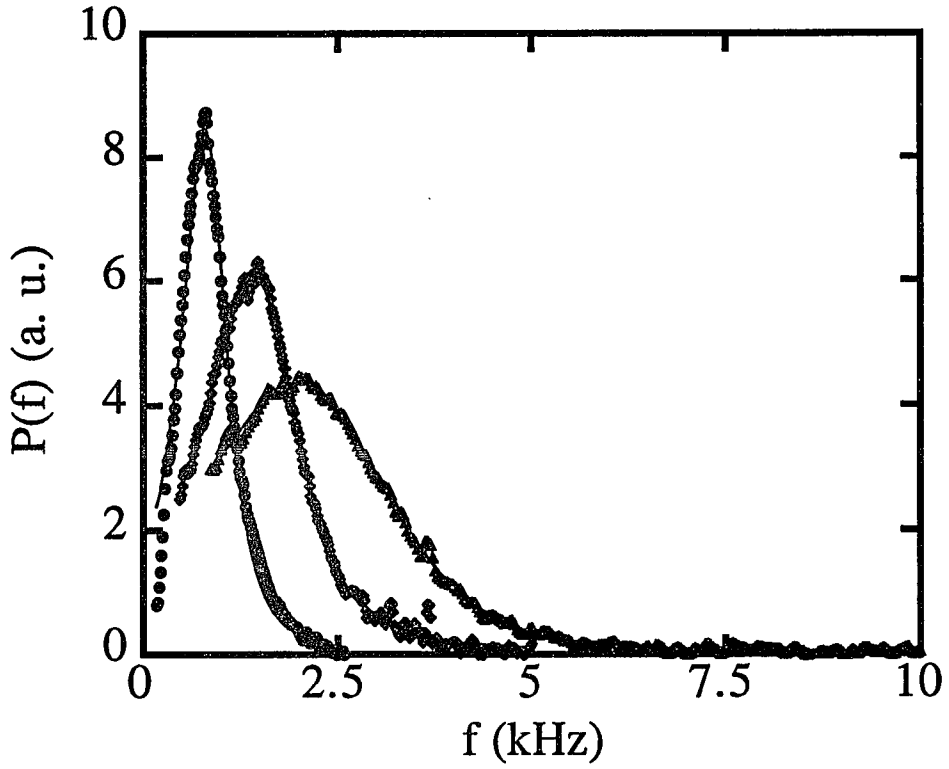

Fig. 4.14. Power spectra of the 4.0 g/dl concentration PBrS/toluene with M_W = 900K at the diffraction orders 2-4, corresponding to k = 97.4, 146.1, and 194.5 cm^{-1}. They are rescaled to have the same baseline. The solids lines are the fits using Eq. (4.2). The symbols correspond to: ● n=2; ◆ n=3; and ▲ n=4.

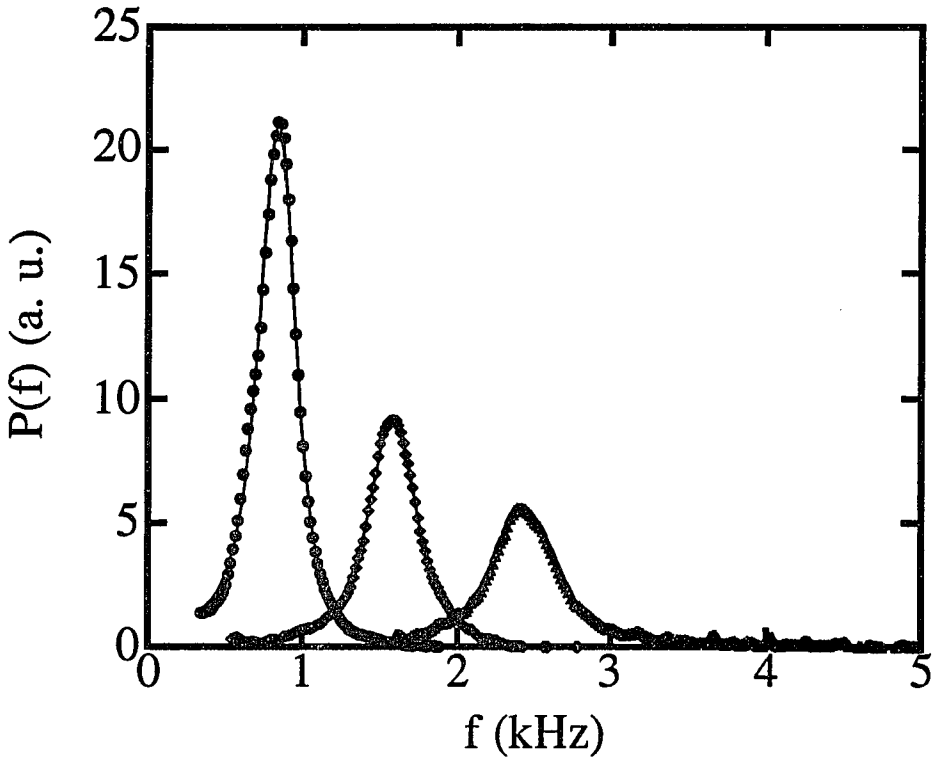

Fig. 4.15. Power spectra of the 0.5 g/dl concentration PBrS/toluene with M_W = 900K at the diffraction orders 2-4, corresponding to k = 97.4, 146.1, and 194.5 cm^{-1}. They are rescaled to have the same baseline. The solids lines are the fits using Eq. (4.2). The symbols correspond to: ● n=2; ◆ n=3; and ▲ n=4.

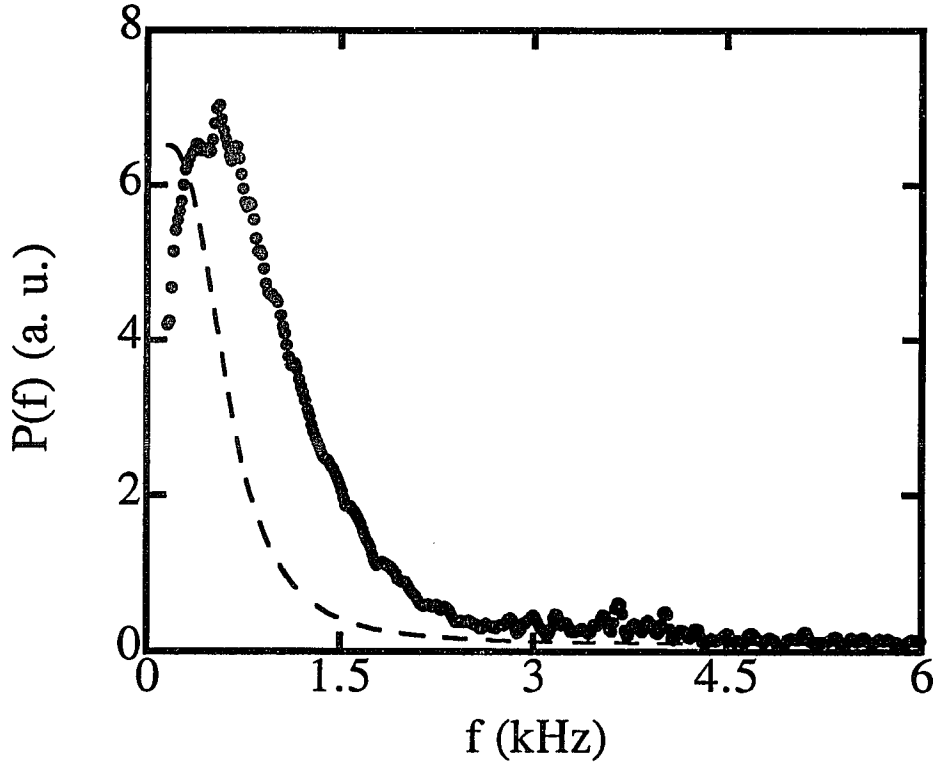

Fig. 4.16. Experimental power spectrum of the 7.0 g/dl concentration PBrS/toluene for $k = 97.4$ cm^{-1}. The dashed line shows the power spectrum for the same k, using Eq. (4.1) with $\sigma = 27.5$ dyne/cm, $\eta = 43.8$ cp, and $\delta_d = 12.1$.

the relaxation time, τ, is found to be $\sim 1 - 3 \times 10^{-5} \ll 1/\omega$ over the entire concentration range. The values of the surface tension and the viscosity are obtained by averaging the values obtained from the individual fits of 4 to 6 power spectra, using the diffraction orders $n = 2 - 7$. The surface tensions measured with the du Nouy ring method remain constant over this concentration range. At bulk concentrations $< 3.0g/dl$, the values of the surface tensions obtained from both light scattering theories are all in good agreement with those measured with the du Nouy ring method. The values of the viscosities from both theories also agree with those measured with a Couette viscometer. However, at higher concentrations, the surface tensions obtained from the fits using the capillary wave theory show large deviations from those measured with the du Nouy ring method. Since the capillary wave theory is only appropriate for simple Newtonian fluids, we attribute this large deviation to the viscoelastic properties of the polymer solutions. By contrast, the theory for viscoelastic polymer solutions yields surface tensions that are significantly improved, as shown in Fig. 4.17(a). This is the direct evidence that the PBrS/toluene solutions at the high concentrations are viscoelastic fluids and that their surface waves are strongly modified by the viscoelasticity of the bulk. The values of viscosities obtained from the fits using both theories at high concentrations are still in reasonable agreement with those measured with the Couette viscometer.

We should note that both theories are derived for fluids with equal concentrations in the bulk and near the surface. The theory for polymer solutions gives consistent results for both the surface tensions and the viscosities over the entire concentration range. By contrast, the capillary wave theory describes the experimental data only at low polymer concentrations. This implies that the depletion layers have no effect on the surface waves of the PBrS/toluene solutions with $M_w = 900K$. Since there is a depletion layer, the concentration very near the surface is always low, regardless of the bulk concentration; thus if the surface waves were affected by the depletion layer, the capillary wave theory would apply at all concentrations. Instead, since the theory for polymer solutions describes the experimental data at all concentrations, the bulk viscoelastic properties must play a dominant role in

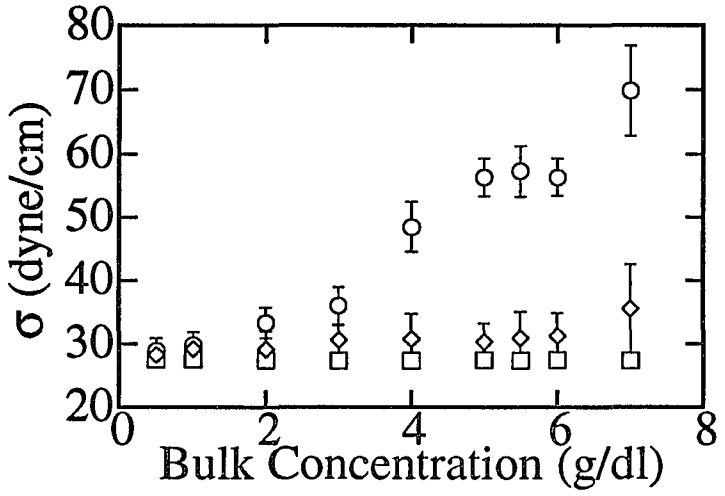

Fig. 4.17(a). Surface tension, σ, *vs.* bulk concentration of PBrS/toluene with $M_W = 900$K. The symbols correspond to: □ data obtained from the du Nouy ring method; o data obtained from the spectral fits using the capillary wave theory, Eq. (4.1); and ◇ data obtained from the spectral fits using the theory for polymer solutions, Eq. (4.2).

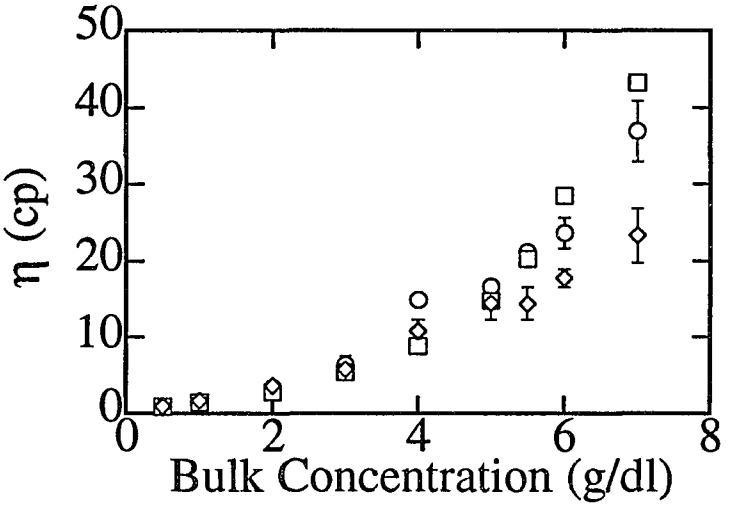

Fig. 4.17(b). Viscosity, η, *vs.* bulk concentration for PBrS/toluene with $M_W = 900$K. The symbols correspond to: □ data obtained from a Couette viscometer; o data obtained from the spectral fits using the capillary wave theory, Eq. (4.1); and ◇ data obtained from the spectral fits using the theory for polymer solutions, Eq. (4.2).

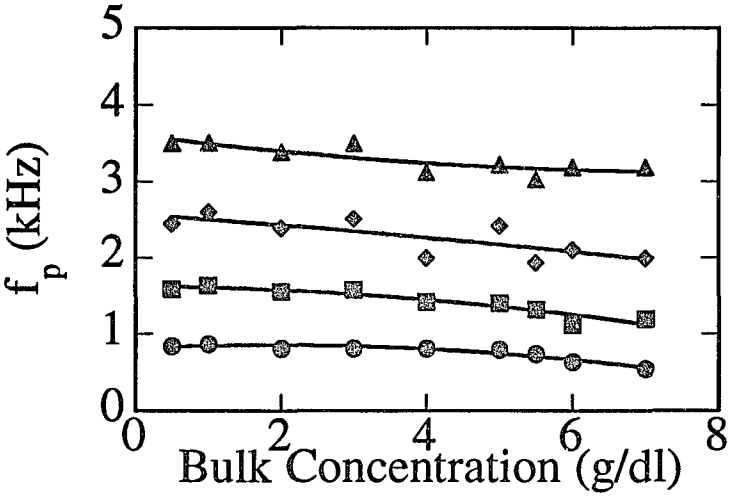

Fig. 4.18(a). Peak frequency, f_p, *vs.* bulk concentration of PBrS/toluene with M_W = 900K at the diffraction orders 2-5. The smooth curves are drawn through the data points for clarity. The symbols correspond to: ● n=2; ■ n=3; ◆ n=4; and ▲ n=5.

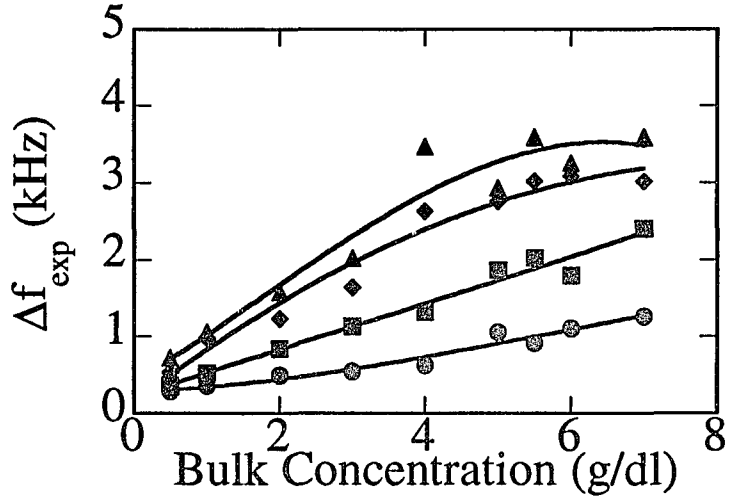

Fig. 4.18(b). Experimental frequency width, Δf_{exp}, *vs.* bulk concentration of PBrS/toluene with M_W = 900K at the diffraction orders 2-5. The smooth curves are drawn through the data points for clarity. The symbols correspond to: ● n=2; ■ n=3; ◆ n=4; and ▲ n=5.

determining the properties of the surface waves. Consistent with this, the depletion layers are still very thin, even for the high molecular weight polymers. For example, we calculate $\xi = 80$ Å as the thickness for the depletion layer at $7.0g/dl$, using Eq. (2.22) and assuming a monomer size of $a \sim 2$ Å.

We also plot the peak frequency, f_p, and the full-width at half-maximum, Δf_{exp}, determined from the fits to the power spectra as functions of the bulk concentration of the PBrS/toluene solutions with $M_w = 900K$, using diffraction orders $n = 2 - 5$. The results are shown in Figs. 4.18(a) and 4.18(b). The peak frequency, f_p, increases with increasing bulk concentration, while Δf_{exp} decreases with increasing bulk concentration as seen in the previous samples.

In conclusion, the surface waves of the PBrS/toluene solutions with $M_w = 900K$ can be well described by the theory for polymer solutions[4] over the entire concentration range. For the low concentration polymer solutions, the surface waves are capillary waves. By contrast, for the high concentration polymer solutions, the surface waves are strongly affected by the viscoelastic behavior of the bulk solutions. In all cases, the depletion layers at the interfaces of the PBrS/toluene solutions have no effect on the surface waves.

4.4 Adsorption effects on Surface Waves at Air/solution Interfaces of Polyethyleneoxide (PEO)/water

Polyethyleneoxide (PEO) is a nonionic water-soluble polymer with wide technical usage. Since PEO is surface active in water, it forms a self-assembled film at the air/solution interface. This results in the reduction of the surface tension at the air/solution interface. We study the surface activity of PEO solutions using surface tension and ellipsometry measurements.[15,16] We find that PEO with $M_w = 85K$ can form very thick adsorption layers due to the hydrogen bond between PEO and water. Furthermore, the surface activity of PEO is strongly molecular weight dependent at higher concentrations. For $M_w > 400K$, there is no additional surface reduction at higher polymer concentrations. The detailed results of the surface activity of

PEO measured by surface tension and ellipsometry are presented in Appendix A. In this section, we present the results of surface wave studies of PEO/water solutions with M_w = 85K and $M_w = 1000K$ by the technique of surface heterodyne light scattering.[17]

In the last two sections, we have shown that the theory for polymer solutions[4] is more appropriate to describe their surface waves over a broad range of concentrations, since it treats the polymer solutions as viscoelastic fluids. At low polymer concentrations, the capillary wave theory[3] can be recovered from this general model.[4] In this section, we will only use the theory for polymer solutions, Eq. (4.2), to fit our experimental power spectra when we assume that there are no effect of adsorption layers at the interfaces of the PEO/water solutions. By contrast, to treat PEO/water solutions with adsorption layers, we use the capillary wave theory for monolayer-covered interfaces, Eq. (4.4), to fit the experimental power spectra.

In the previous two sections, we have also shown that the values of the surface tensions obtained from the spectral fits using the theory for polymer solutions are consistent with those measured with the du Nouy ring method. For the PEO/water solutions, we fit the experimental power spectra to Eq. (4.2) by fixing the surface tension to the value measured with the du Nouy ring method, σ, and only adjusting the transient modulus, G_0, and the relaxation time, τ; this reduces the number of the fitting parameters. The physical parameters G_0 and τ, or their product, will be compared with those obtained from the rheological measurements.

We will also show that the surface waves of the PEO/water solutions at low concentrations can only be properly described by the capillary wave theory for monolayer-covered interfaces; this is due to the PEO adsorption layers near interface. For the PEO/water solutions at high concentrations, we need a new and more complicated theory which treats the polymer solutions as viscoelastic fluids and includes the effects of a monolayer-covered interface between the air and the solutions.

4.4.1 Polyethyleneoxide (PEO) with Molecular Weight 85K

In Fig. 4.19, we plot the values of the surface tension, σ, and the viscosity, η, as functions of the polymer concentration. The surface tensions were measured with the du Nouy ring method and the viscosities were measured with a Couette viscometer. Based on the viscosity measurements, we found that c^* for the PEO/water solutions with $M_w = 85K$ was $1.19g/dl$. In the very dilute regime, the surface tension decreases as the polymer concentration is increased. At higher concentrations, the surface tension reaches a plateau, with $\sigma \sim 62.0 dyne/cm$. Finally, at concentrations higher than c^*, the surface tension is further reduced.

The concentration range for our surface wave studies is from $0.5g/dl$ to $10.0g/dl$. Figures 4.20 - 4.22 show the experimental power spectra of PEO/water solutions with $M_w = 85K$ and with bulk concentrations of $10.0g/dl$, $5.5g/dl$, and $0.5g/dl$ for the diffraction orders $n = 2 - 4$. For comparison, we also plot the fits to Eq. (4.2). Equation (4.2) gives good fits to the experimental power spectra. The values of the peak frequencies and frequency widths determined from the fits to the power spectra are plotted in Figs. 4.23(a) and 4.23(b) as functions of the bulk concentration, using diffraction orders $n = 2 - 5$. From Fig. 4.23(a), one can see that the values of f_p decrease rapidly as the bulk concentration is increased. This could be due to the fact that, over this concentration range, the surface tensions of the PEO/water solutions with $M_w = 85K$ decrease with increasing bulk concentration, as show in Fig. (4.20). Also, the values of Δf_{exp} increase as the bulk concentration is increased, indicating an increase of the viscosity of the polymer solution.

The physical parameters obtained from the fits using Eq. (4.2) are the transient modulus, G_0, and the relaxation time, τ. Since the relaxation time, τ, for the PEO/water solutions with $M_w = 85K$ is typically about $1-3\times10^{-5}s$, we can calculate the viscosities using Eq. (4.3) and compare them with the values measured with a Couette viscometer. A comparison of these viscosity values is made in Fig. 4.24 for PEO/water with $M_w = 85K$. The values of the viscosities extracted from the spectral analysis are obtained by averaging the values obtained from the individual

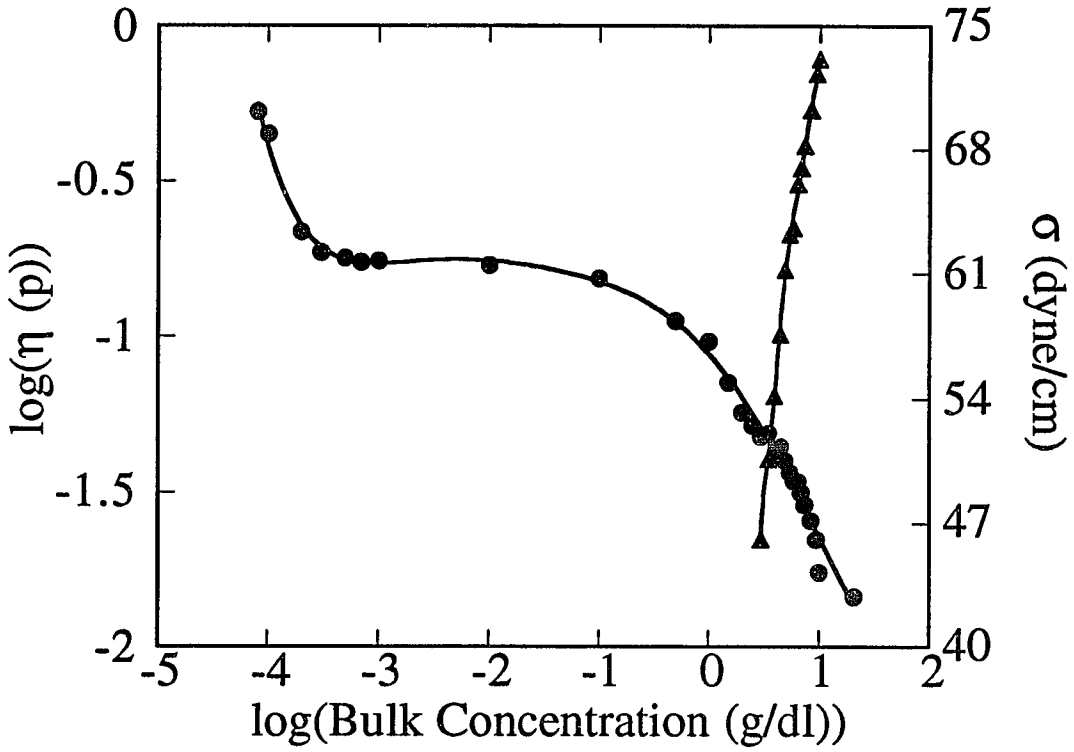

Fig. 4.19. Viscosity, η, and surface tension, σ, *vs.* bulk concentration of PEO/water with M_W = 85K. The symbols correspond to: ● viscosity from a Couette viscometer; ▲ surface tension from the du Nouy method. The smooth curves are drawn through the data points for clarity.

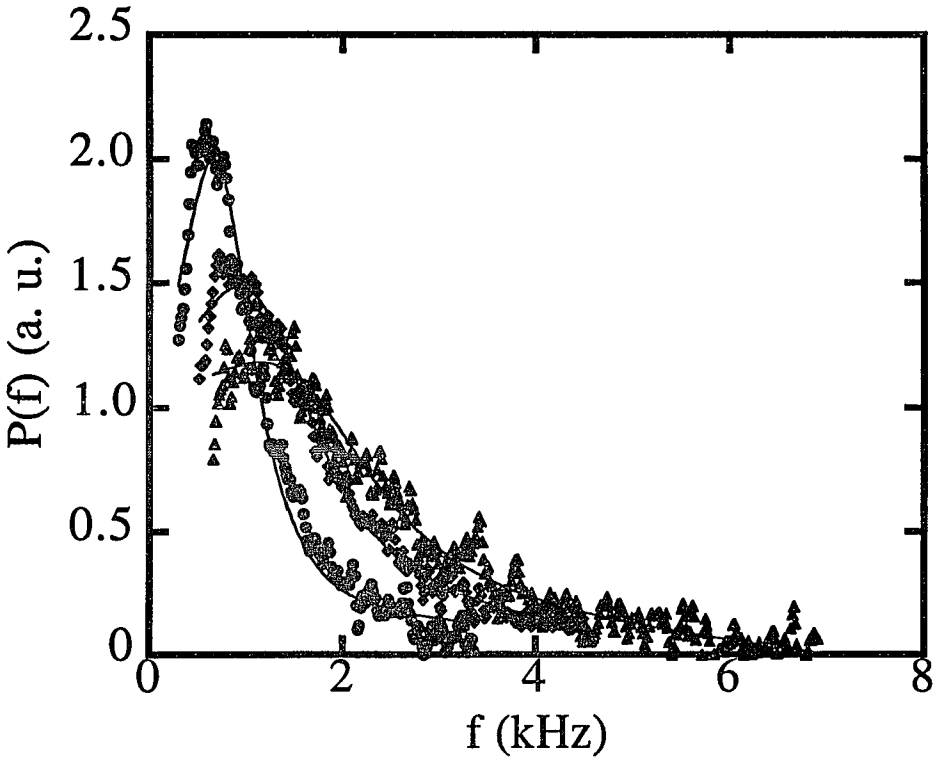

Fig. 4.20. Power spectra of the 10.0 g/dl concentration PEO/water with M_W = 85K at the diffraction orders 2-4, corresponding to k = 91.7, 137.9, and 183.7 cm^{-1}. They are rescaled to have the same baseline. The solids lines are the fits using Eq. (4.2). The symbols correspond to: ● n=2; ◆ n=3; and ▲ n=4.

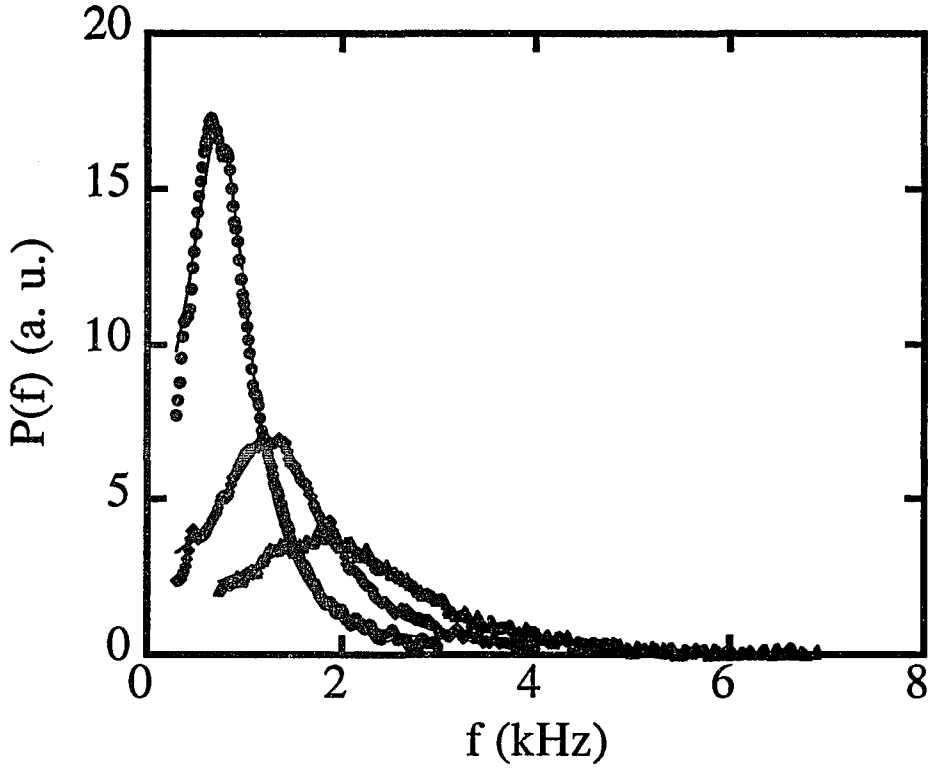

Fig. 4.21. Power spectra of the 5.5 g/dl concentration PEO/water with M_W = 85K at the diffraction orders 2-4, corresponding to k = 91.7, 137.9, and 183.7 cm^{-1}. They are rescaled to have the same baseline. The solids lines are the fits using Eq. (4.2). The symbols correspond to: ● n=2; ◆ n=3; and ▲ n=4.

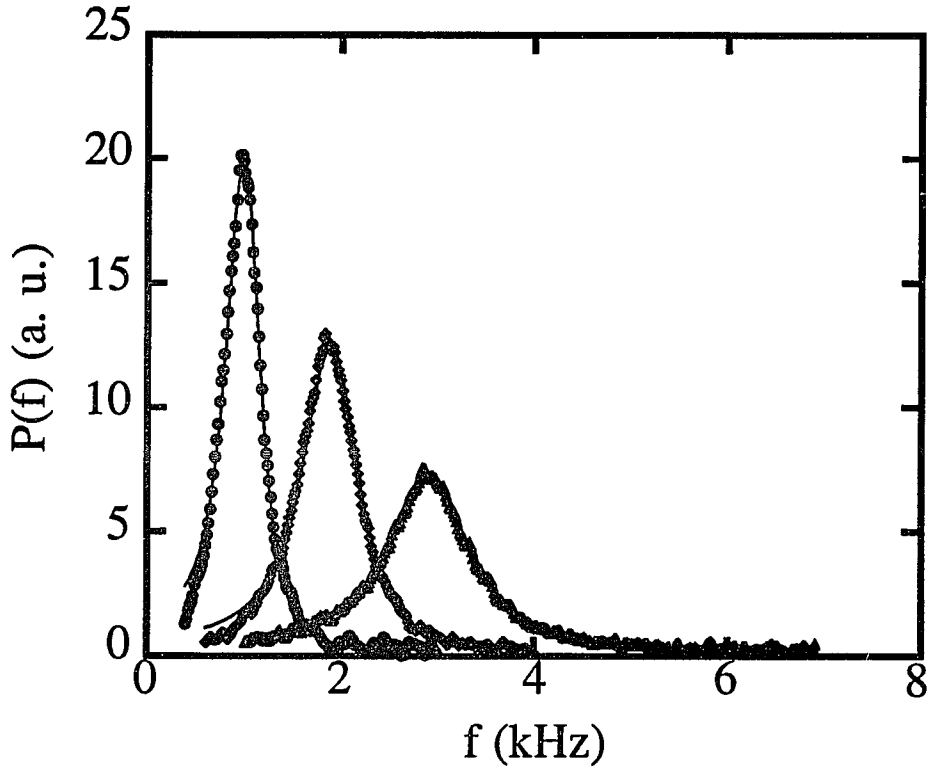

Fig. 4.22. Power spectra of the 0.5 g/dl concentration PEO/water with M_W = 85K at the diffraction orders 2-4, corresponding to k = 91.7, 137.9, and 183.7 cm^{-1}. They are rescaled to have the same baseline. The solids lines are the fits using Eq. (4.2). The symbols correspond to: ● n=2; ◆ n=3; and ▲ n=4.

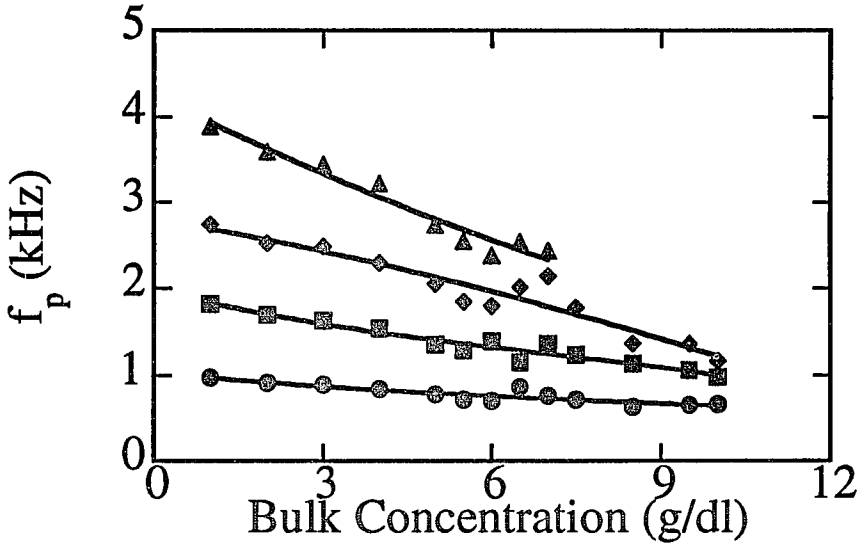

Fig. 4.23(a). Peak frequency, f_p, *vs.* bulk concentration for PEO/water with M_W = 85K at the diffraction orders 2-5. The smooth curves are drawn through the data points for clarity. The symbols correspond to: ● n=2; ■ n=3; ◆ n=4; and ▲ n=5.

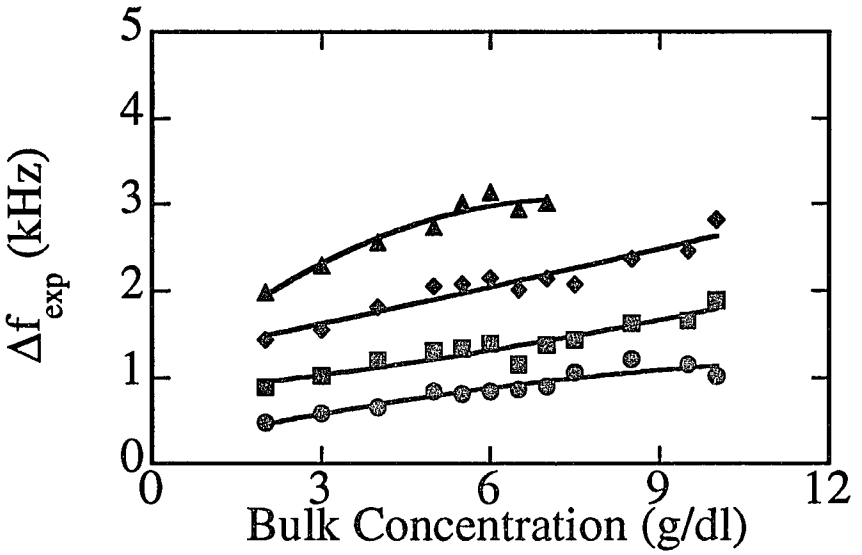

Fig. 4.23(b). Experimental frequency width, Δf_{exp}, *vs.* bulk concentration for PEO/water with M_W = 85K at the diffraction orders 2-5. The smooth curves are drawn through the data points for clarity. The symbols correspond to: ● n=2; ■ n=3; ◆ n=4; and ▲ n=5.

fits of 4 power spectra, using the diffraction orders $n = 2-5$. At polymer concentrations $> 6.0g/dl$, the values of the viscosities obtained from the spectral analysis are much smaller than those measured with the Couette viscometer. At concentrations $\leq 5.0g/dl$, the results are reversed; the values of the viscosities obtained from the spectral analysis are larger than those measured with the Couette viscometer. This inconsistency in the viscosity indicates that the adsorption layers of the PEO/water solutions have important effects on the surface waves. One of the assumptions for the theory for polymer solutions is that there are no gradients of polymer concentration near the interface.[4] Without taking into account the adsorbed layers, it is not surprising that the theory for polymer solutions gives incorrect results for the viscosity. Also, due to the hydrogen bond between PEO and water, the thickness of the PEO adsorption layers could be much greater than the radius of gyration, $\xi \sim 50$ Å.[15] This thick adsorption layer may strongly modify the surface waves of PEO/water solutions.

To interpret the experimental power spectra correctly, we need to use a comprehensive theory that accounts for the effects of the adsorbed layers at the solution interface. The only theory available for this case is the capillary wave theory for monolayer-covered interfaces, Eq. (4.4). Figure 4.25 shows the fits to the experimental power spectrum for the $10.0g/dl$ concentration PEO/water solution with $M_w = 85K$ at the diffraction order $n = 3$. We use both theoretical models, Eq. (4.2) and Eq. (4.4). Clearly, Eq. (4.4) gives the better fit at the low frequency part of the power spectrum. By contrast, for bulk concentrations $< 5.5g/dl$, both theories give good fits to the power spectra of the PEO/water solutions with $M_w = 85K$. However, we take the result from Fig. 4.25 as the direct evidence that the most suitable theoretical model for the PEO/water solutions with $M_w = 85K$ should include the effects of the adsorbed layers at the air/solution interface.

As discussed earlier, the surface longitudinal elasticity, ε, and the surface longitudinal viscosity, κ, can be calculated from the spectral analysis using Eq. (4.4). These results are obtained from fits using the measured values of the surface tensions. The results of ε and κ are shown in Figs. 4.26(a) and 4.26(b). For samples

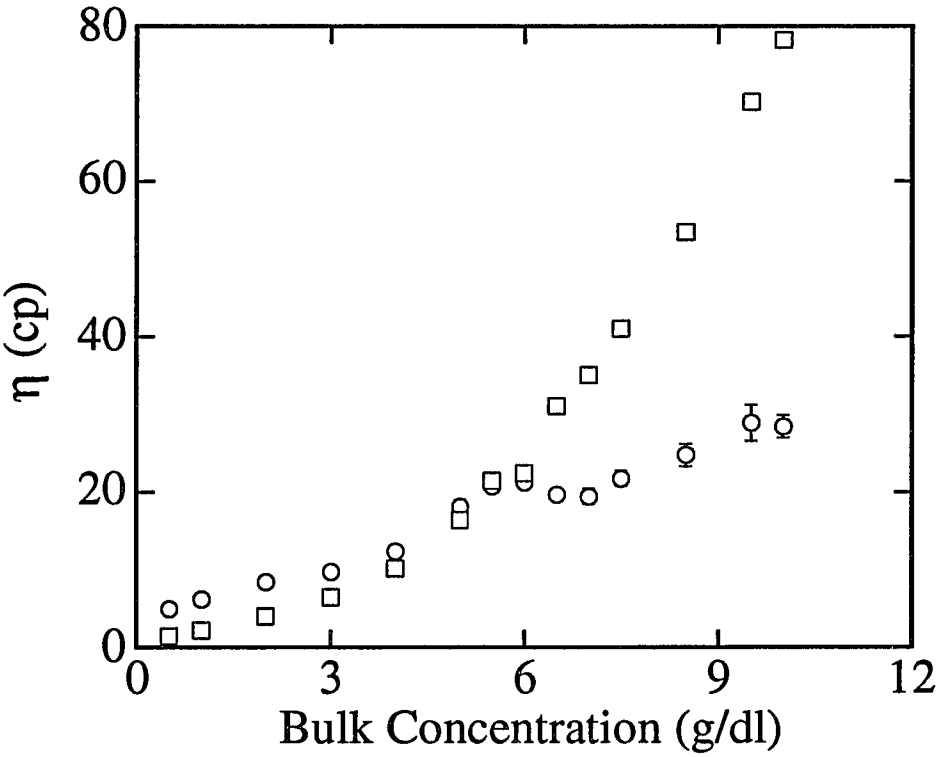

Fig. 4.24. Viscosity, η, *vs.* bulk concentration of PEO/water with M_W = 85K. The symbols correspond to: □ data obtained from a Couette viscometer; and o data obtained from the spectral fits using the theory for polymer solutions, Eq. (4.2).

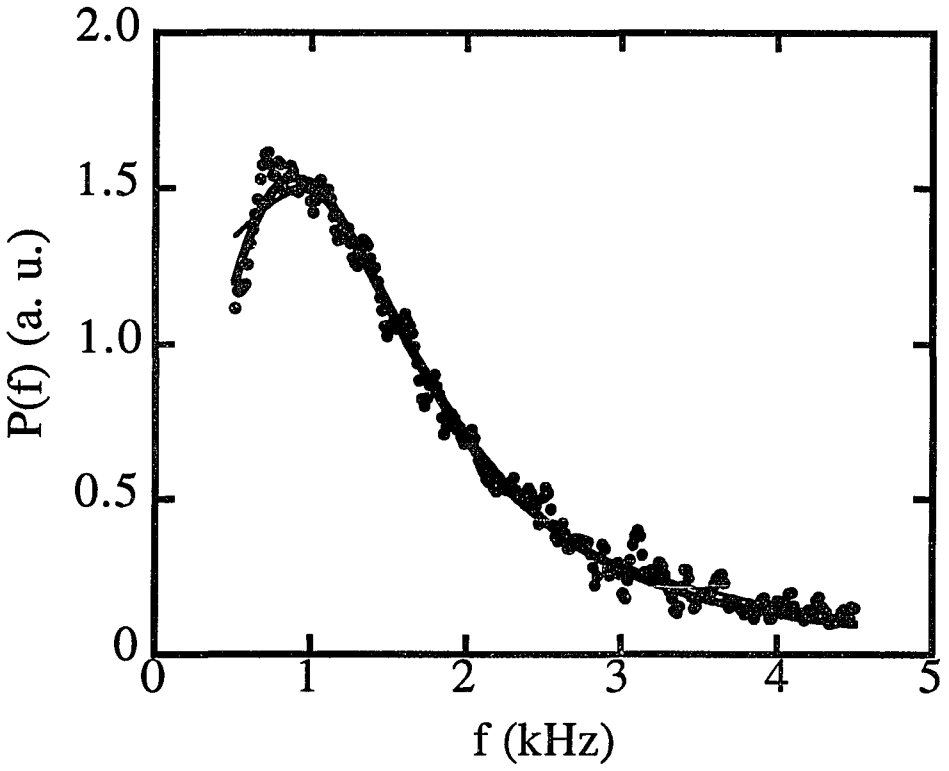

Fig. 4.25. Experimental Power spectrum of the 10.0 g/dl concentration PEO/water with M_W = 85K for k=137.9 cm^{-1}. The thin line is the fit using Eq. (4.2); the thick line is the fit using Eq. (4.4).

with concentrations higher than $4.0g/dl$, the values of ε and κ at each wave vector represent the average of the analysis of 3 power spectra. Clearly, at bulk concentrations higher than $6.0g/dl$, both ε and κ are wave vector dependent (frequency dependent) and decrease as k decreases, whereas, at bulk concentrations less than $6.0g/dl$, ε and κ show no wave vector dependence.

Since, in two dimensions, ε is the elasticity and κ is the viscosity, there is a direct analogy with the elastic modulus, G', and the viscosity, η, in three-dimensions. Thus, we expect that η, and therefore κ, should decrease with increasing frequency due to shear thinning. This is observed. By contrast, we expect that G', and therefore ε, should increase with increasing frequency. This is not observed. One possible reason for this is that the viscoelastic parameters in two dimensions can not be simply compared with those in three dimensions.

The viscoelastic parameters of the PEO adsorbed films at the very dilute concentration regime have been measured by other workers.[18,19] At low polymer concentrations, the films of PEO adsorbed from the bulk are very similar to those formed by spreading a monolayer of PEO at the air/water interface. The values of ε have been found to depend on the PEO concentration and to vary between $1dyn/cm$ and $30dyne/cm$, while those of κ vary between $1 \times 10^{-5}g/s$ and $30 \times 10^{-5}g/s$. We find that the values of ε and κ at high polymer concentrations are much larger than those measured for very low concentrations. This result further confirms that $85K$ PEO forms very dense and thick adsorption layers near air/solution interfaces.[15] Since we do not know the surface concentration at those high polymer concentrations, we cannot determine the static elasticity, ε_s, as defined in Eq. (2.54). Thus, it is not possible to directly compare the dynamic longitudinal elasticity, ε, with the static elasticity, ε_s.

We note that the use of the capillary wave theory for monolayer-covered interfaces implies that the PEO/water solutions behave as simple Newtonian fluids even at high polymer concentrations. As we showed earlier, this may not be true since, at high concentrations, surface waves at the air/solution interface can only be properly described by accounting for the viscoelastic properties of the bulk. Since

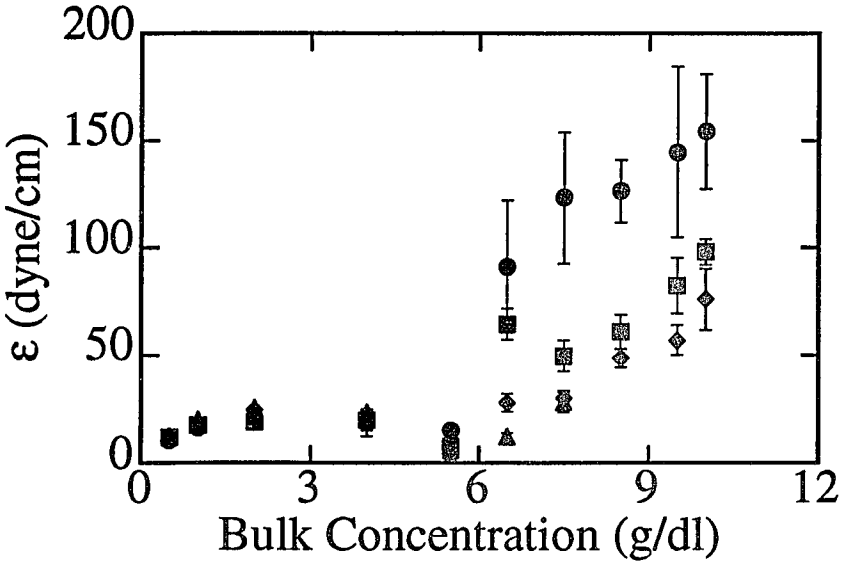

Fig. 4.26(a). Surface longitudinal elasticity, ε, *vs.* bulk concentration of PEO/water with M_W = 85K. The symbols correspond to: ● n=2; ■ n=3; ◆ n=4; and ▲ n=5.

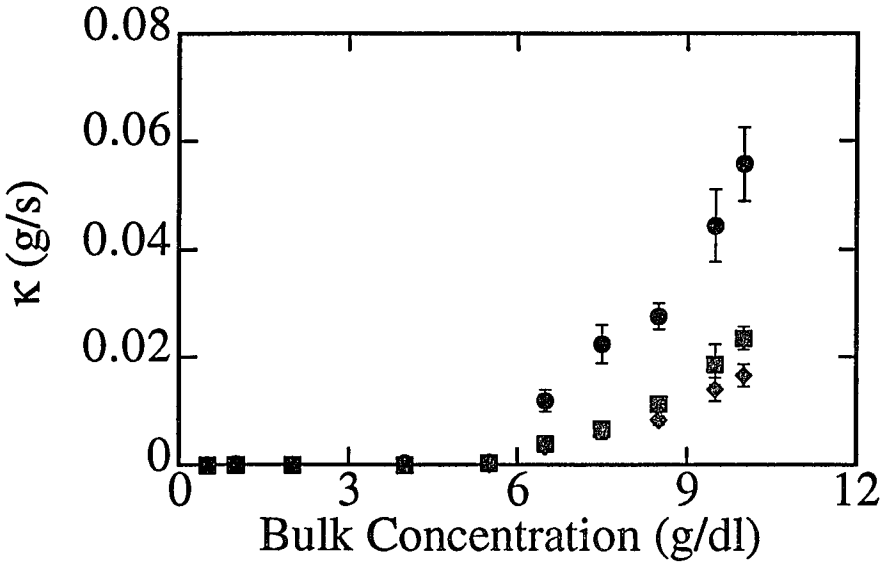

Fig. 4.26(b). Surface longitudinal viscosity, κ, *vs.* bulk concentration of PEO/water with M_W = 85K. The symbols correspond to: ● n=2; ■ n=3; ◆ n=4; and ▲ n=5.

the capillary wave theory does not account for these effects, it may give an incorrect prediction of the frequency dependence of ε and κ.

To conclude, the spectral data of the PEO/water solutions with $M_w = 85K$ can not be described by the theory for polymer solutions. We attribute this to the effects of layers of adsorbed PEO. The experimental power spectra are interpreted better by the capillary wave theory for monolayer-covered interfaces. The explanation for the frequency dependence of ε and κ needs further study. The presence of the adsorption layers changes the boundary conditions of polymer solutions, modifying the surface wave motion; a more sophisticated theory, which accounts for both the bulk and surface viscoelastic properties, is needed.

4.42 Polyethyleneoxide (PEO) with Molecular Weight 1000K

In Fig. 4.27, we plot the surface tension, σ, and the viscosity, η, as functions of the bulk concentration. The surface tensions were measured with the du Nouy ring method. At bulk concentrations $\leq 2.5g/dl$, the viscosities were measured with a Couette viscometer. At higher bulk concentrations, the viscosities were measured with a cone and plate rheometer (Rheometrics, Inc.), using $\eta = lim_{\omega \to 0} G''/\omega$. Based on the viscosity measurements, we found that c^* for the PEO/water solutions with $M_w = 1000K$ was $0.22g/dl$. In the very dilute regime, the surface tension decreases as the polymer concentration increases. At higher concentrations, the surface tension reaches a plateau, with $\sigma \sim 62.0 dyne/cm$. Unlike the surface tension of $85K$ PEO, which decreases from the plateau at the highest bulk concentrations, the surface tension of $1000K$ PEO remains constant.

In our surface wave studies, the bulk PEO concentration ranges from $1 \times 10^{-4} g/dl$ to $9.5g/dl$. The corresponding bulk viscosities exhibit a change of 10^6, from $10^{-2}p$ to $4 \times 10^4 p$.

Figures 4.28 - 4.30 show the experimental power spectra of PEO/water solutions with $M_w = 1000K$ and with bulk concentrations of $5.0g/dl$, $2.0g/dl$, and $0.5g/dl$ for the diffraction orders $n = 2 - 4$. For comparison, we also plot the fits to

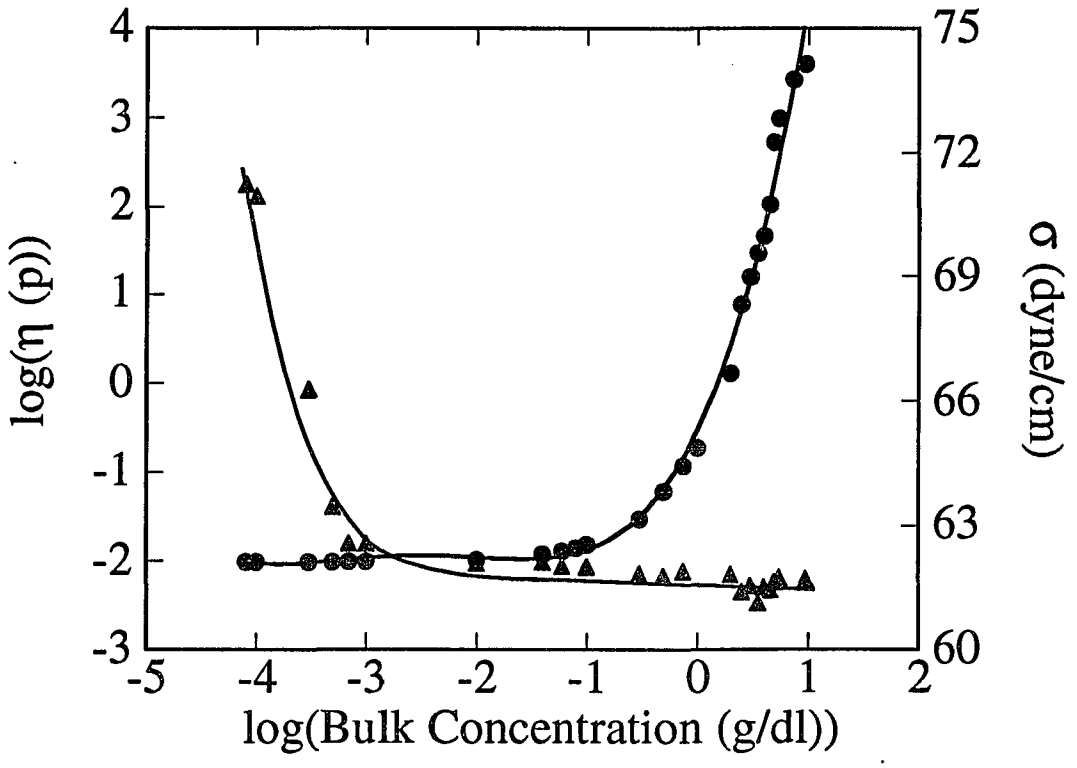

Fig. 4.27. Viscosity, η, and surface tension, σ, *vs.* bulk concentration of PEO/water with M_W = 1000K. The symbols correspond to: ● viscosity: from a Couette viscometer for bulk concentrations ≤ 2.5 g/dl, and from a cone and plate rheometer for bulk concentrations > 2.5 g/dl; and ▲ surface tension from the du Nouy method. The smooth curves are drawn through the data points for clarity.

Eq. (4.2). The experimental power spectra are well described by Eq. (4.2). Each experimental power spectrum of the $5.5g/dl$ sample was taken on the spectrum analyzer by accumulating for about one hour due to the weak scattering intensity from the sample. For the other two samples, the accumulation time was 10 to 15 mins.

In Figs. 4.31(a) and 4.31(b), we also plot the experimental power spectra at $k = 88.6cm^{-1}$ for six representative polymer solutions, along with the fits to Eq. (4.2). Their bulk concentrations are $7.4g/dl$,4.0 g/dl,3.0 g/dl,2.0 g/dl,0.75 g/dl and $0.5g/dl$. The surface tensions of these six samples measured with the du Nouy ring method have the same values, $\sim 62.0dyne/cm$. For bulk concentrations $< 2.5g/dl$, the peak frequency decreases with increasing bulk concentration; by contrast, for bulk concentrations $> 2.5g/dl$, the peak frequency increases with increasing bulk concentration. Similarly, for bulk concentrations $< 2.5g/dl$, the frequency width increases with increasing bulk concentration, indicating an increase of the viscosity of the polymer solution, while for bulk concentrations $> 2.5g/dl$, the frequency width decreases with increasing bulk concentration, despite the rapid increase of the viscosity of the polymer solution. This unusual behavior of the peak frequency and the frequency width for the PEO/water solutions with $M_w = 1000K$ at high bulk concentrations reflects the strong viscoelasticity of the PEO solutions which results in an additional restoring force for the surface waves.

We can determine the values of the peak frequency, f_p, and the frequency width, Δf_{exp}, from the fits to the power spectra for a given sample at a given wave vector. The values of the peak frequencies of the PEO/water solutions with $M_w = 1000K$ are plotted as a function of the bulk concentration in Fig. 4.32(a) and the corresponding frequency widths in Fig. 4.32(b). Figure 4.32 clearly summarizes the unusual behavior of the peak frequencies and frequency widths for the PEO/water solutions with $M_w = 1000K$, that was shown in Fig. 4.31. For bulk concentrations less than $2.5g/dl$, f_p decreases and Δf_{exp} increases as the bulk concentration is increased. However, at higher bulk concentrations, f_p increases significantly with increasing bulk concentration, whereas Δf_{exp} decreases initially and then remains

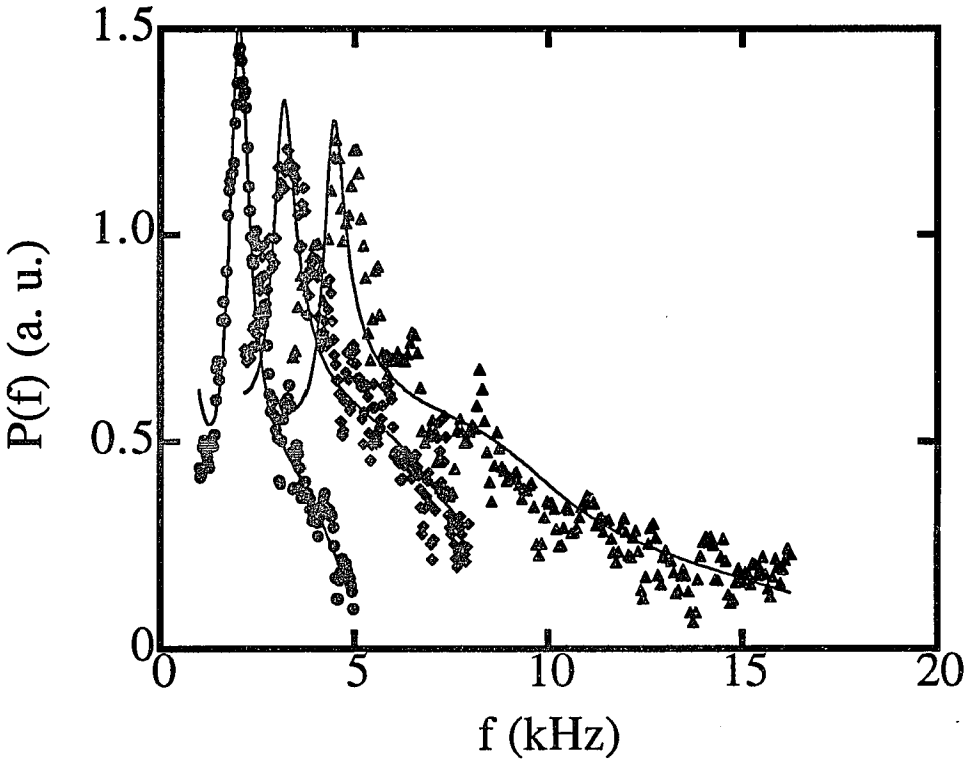

Fig. 4.28. Power spectra of the 5.0 g/dl concentration PEO/water with M_W = 1000K at the diffraction orders 2-4, corresponding to k = 88.6, 133.2, and 179.0 cm^{-1}. They are rescaled to have the same baseline. The solids lines are the fits using Eq. (4.2). The symbols correspond to: ● n=2; ◆ n=3; and ▲ n=4.

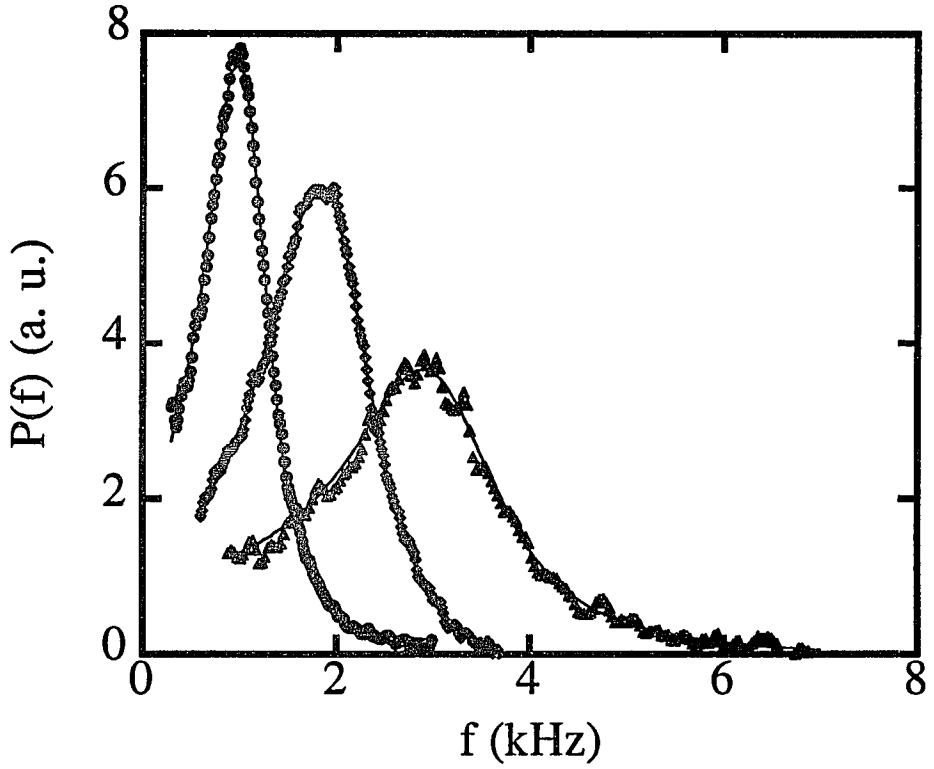

Fig. 4.29. Power spectra of the 2.0 g/dl concentration PEO/water with M_W = 1000K at the diffraction orders 2-4, corresponding to k = 88.6, 133.2, and 179.0 cm^{-1}. They are rescaled to have the same baseline. The solids lines are the fits using Eq. (4.2). The symbols correspond to: ● n=2; ◆ n=3; and ▲ n=4.

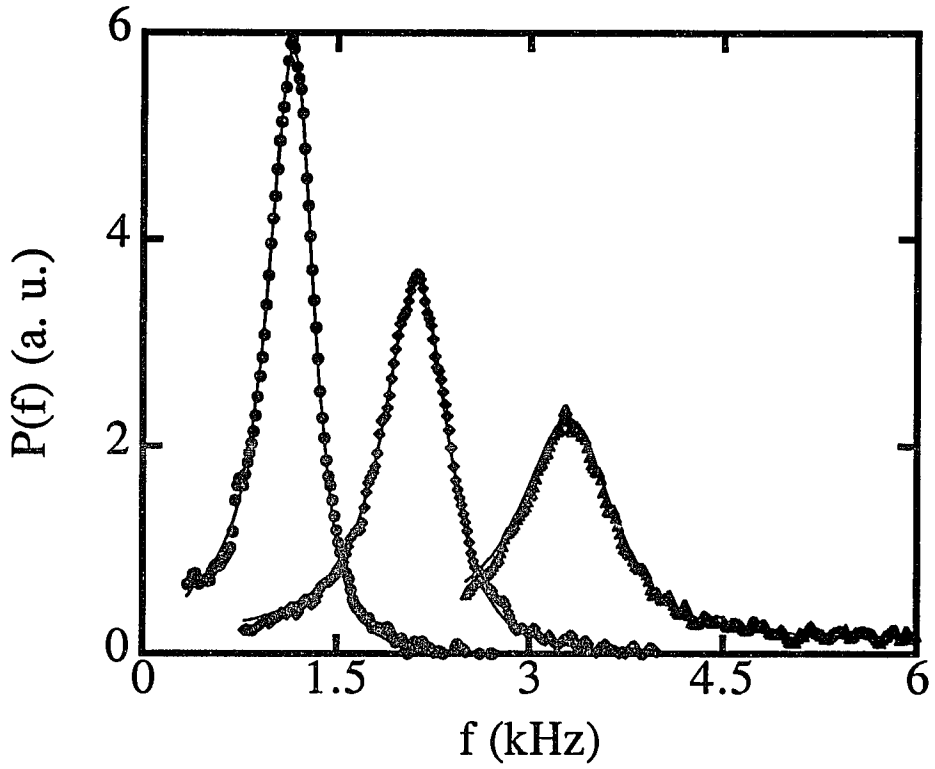

Fig. 4.30. Power spectra of the 0.5 g/dl concentration PEO/water with M_W = 1000K at the diffraction orders 2-4, corresponding to k = 88.6, 133.2, and 179.0 cm^{-1}. They are rescaled to have the same baseline. The solids lines are the fits using Eq. (4.2). The symbols correspond to: ● n=2; ◆ n=3; and ▲ n=4.

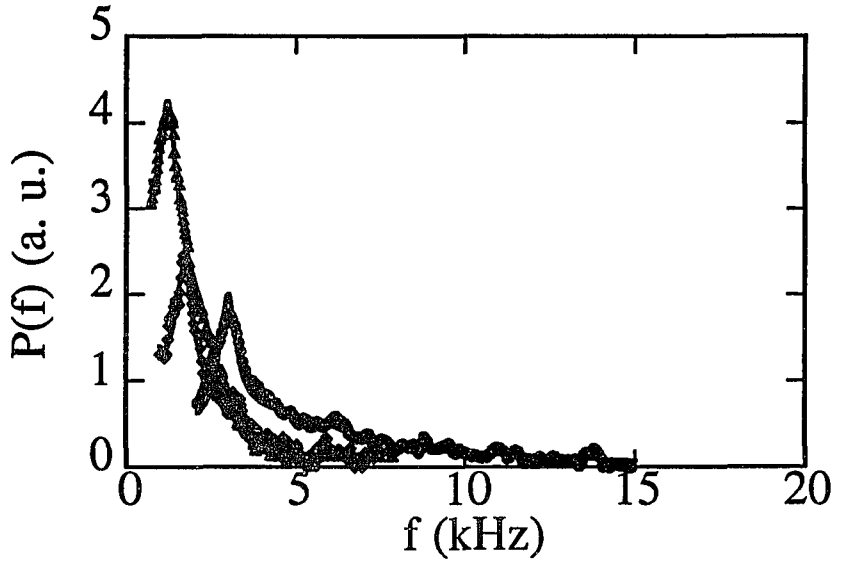

Fig. 4.31(a). Power spectra of PEO/water with M_W = 1000K for k = 88.6 cm^{-1} at the different bulk concentrations. The symbols correspond to: ● 7.4 g/dl; ◆ 4.0 g/dl; and ▲ 3.0 g/dl. The solid lines are the fits using Eq. (4.2).

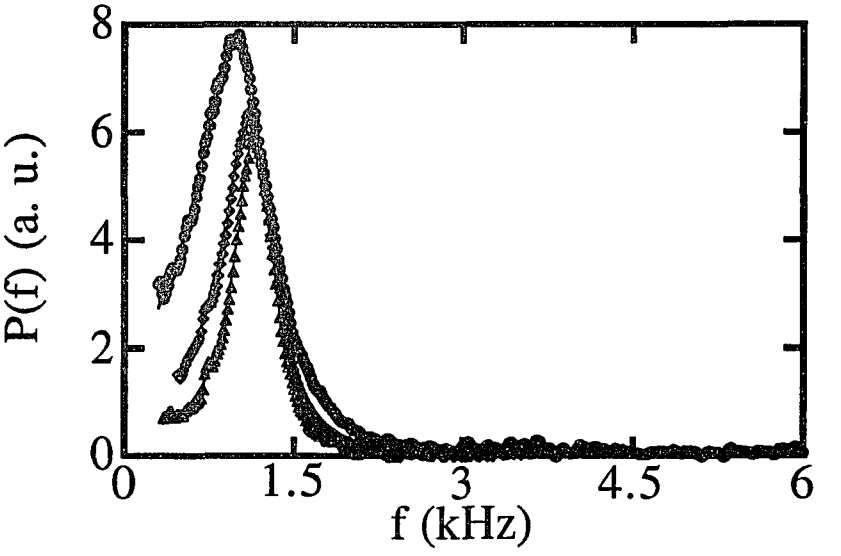

Fig. 4.31(b). Power spectra of PEO/water with M_W = 1000K for k = 88.6 cm^{-1} at the different bulk concentrations. The symbols correspond to: ● 2.0 g/dl; ◆ 0.75 g/dl; and ▲ 0.5 g/dl. The solid lines are the fits using Eq. (4.2).

almost constant when the bulk concentration reaches $4.0g/dl$. The concentration dependence of f_p and Δf_{exp} for the very high molecular weight PEO are totally different from all other polymer solutions studied here (see Fig. 4.5 for PIB/decane of $Mw = 80K$, Fig. 4.11 for PBrS/toluene of $M_w = 90K$, Fig. 4.18 for PBrS/toluene of $M_w = 900K$, and Fig. 4.23 for PEO/water of $M_w = 85K$). For all other polymer solutions, the values of f_p and Δf_{exp} only change monotonically with the bulk concentration. We note also that at bulk concentrations $> 4.0g/dl$, Δf_{exp} is about the same as that of the $1.0g/dl$ concentration PEO/water, while the viscosity at $4.0g/dl$ is about 2×10^3 larger that at $1.0g/dl$. This is a strong evidence that the bulk polymer solutions are viscoelastic fluids and that the viscosities are reduced at the high frequencies of the surface light scattering.

The theory for polymer solutions[4] predicts that for a polymer solution with a very high elastic modulus, the resonant frequency is primarily determined by the transient elastic modulus, G_0, as given in Eq. (2.128). Thus, the restoring force for the surface waves of polymer solutions is the surface tension at low polymer concentrations and crosses over to the elasticity when the polymer concentration is increased sufficiently for the modulus to dominate. Thus, the elasticity can overcome the effects of damping. Therefore, the peak frequency of the power spectrum can be shifted to a higher value and the surface waves can still propagate due to the high elastic modulus. Since the elastic modulus of polymer solutions increases with increasing bulk concentration, the peak frequency should also increase with increasing bulk concentration. This is the reason that, at high concentrations, the values of the peak frequencies are high and increase with increasing bulk concentration for the PEO/water solutions with $M_w = 1000K$, as shown in Fig. 4.32(a).

At high concentrations, polymer solutions are non-Newtonian fluids and their viscosities are frequency dependent. For the PEO/water solutions with $M_w = 1000K$, shear thinning behavior is observed in measurements with the cone and plate rheometer at bulk concentrations $> 2.5g/dl$. The frequencies for the mechanical measurements range from 1 to $100Hz$, while the typical frequency range for surface light scattering is from $1kHz$ to $100kHz$. Thus, the viscosities detected by

surface light scattering can be further reduced at these high frequencies. Since the viscosities of the low concentration polymer solutions are frequency independent, the frequency widths of the power spectra increase with increasing bulk concentration. At high polymer concentrations, the viscosities detected by surface light scattering are small despite the high zero-frequency viscosities; this results in the decrease of the frequency widths with increasing bulk concentration. This phenomenon is observed for the PEO/water solutions with $M_w = 1000K$, as shown in Fig. 4.32(b).

From the spectral analysis, we can obtain the transient modulus, G_0, and the relaxation time, τ. The values of G_0 and τ can also be obtained by fitting the rheological measurements, G' and G'', to the Maxwell model,[5] as given in Eq. (2.126). The results from these two measurement methods are compared in Figs. 4.33(a) and 4.33(b). The transient modulus, G_0, and the relaxation time, τ, obtained from the spectral analysis are calculated by averaging the values obtained from the individual fits of 3 to 4 power spectra, using the diffraction orders $n = 2 - 5$. We can see that the values of G_0 and τ from both methods increase as the bulk concentration is increased. This tendency is expected since polymer solutions change from more liquid-like to more solid-like materials as we increase the polymer concentration. It is also evident that the values of G_0 obtained from the spectral analysis are slightly higher that those calculated from the rheological results, while the values of τ from the spectral analysis are 100 times less than those calculated from the rheological results.

From the scaling laws,[20] we have $\tau \sim \tau_0 N^3 \phi^{3/2}$, where $\tau_0 \approx \eta_s a^3/k_B T$, and where a is the dimension of a monomer unit, N is the number of monomer units in the chain, and ϕ is the bulk concentration. For the $7.4g/dl$ PEO/water solution with $M_w = 1000K$, we have $\tau \sim 0.3s$, using $N \sim 2 \times 10^4$, $\eta_s = 1.0cp$ and assuming $a \sim 2$ Å. Thus, the value predicted for the full chain is closer to that obtained from the rheological measurements. The smaller values of τ measured with the surface light scattering suggest that, at the high frequencies probed by the scattering technique, the viscoelastic behavior reflects the relaxation of a smaller portion of each chain.

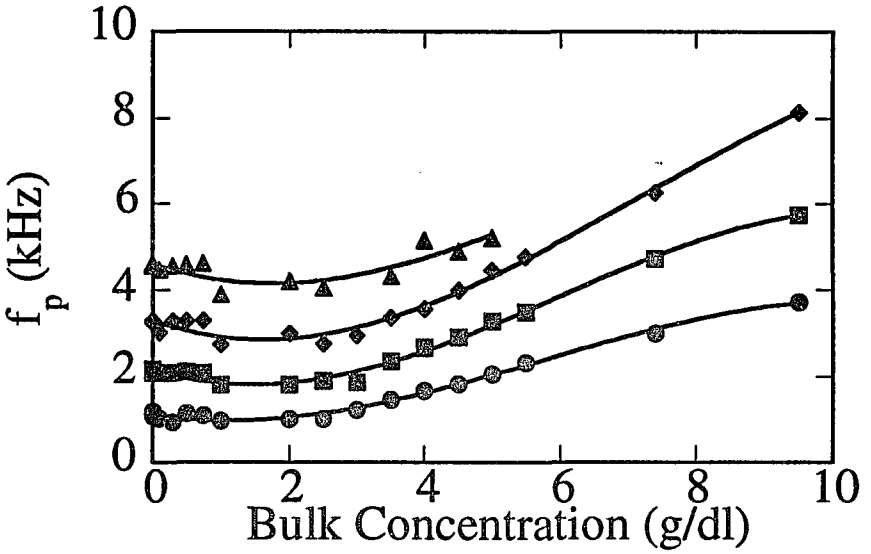

Fig. 4.32(a). Peak frequency, f_p, *vs.* bulk concentration of PEO/water with M_W = 1000K at the diffraction orders 2-5. The smooth curves are drawn through the data points for clarity. The symbols correspond to: ● n=2; ■ n=3; ◆ n=4; and ▲ n=5.

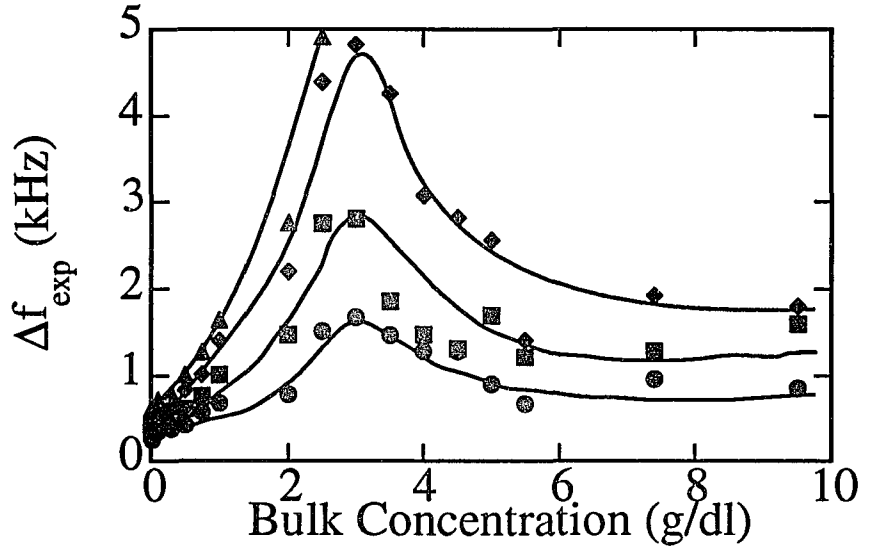

Fig. 4.32(b). Experimental frequency width, Δf_{exp}, *vs.* bulk concentration of PEO/water with M_W = 1000K at the diffraction orders 2-5. The smooth curves are drawn over the data points for clarity. The symbols correspond to: ● n=2; ■ n=3; ◆ n=4; and ▲ n=5.

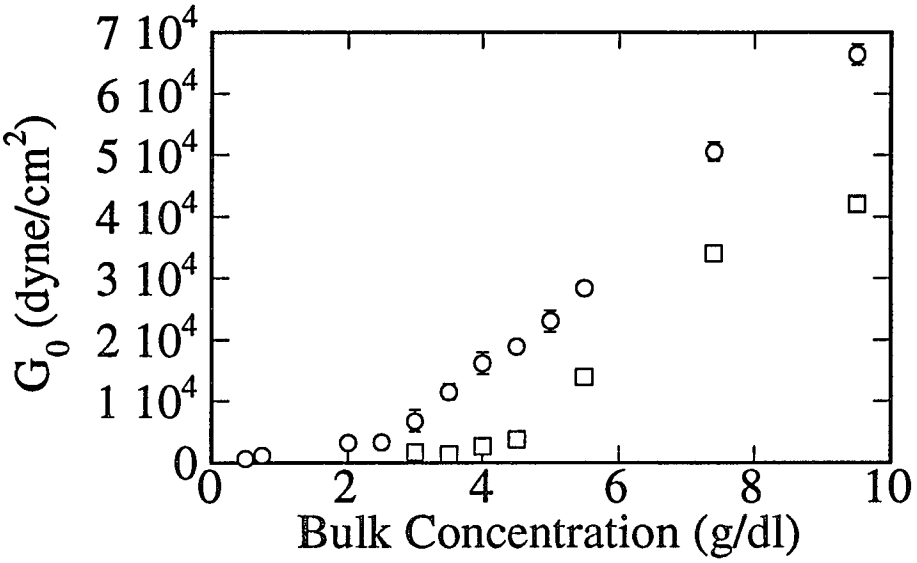

Fig. 4.33(a). Transient modulus, G_0, *vs.* bulk concentration of PEO/water with M_W = 1000K. The symbols correspond to: o data obtained from the spectral fits using the theory for polymer solutions, Eq. (4.2); and □ data obtained from the fits to the rheological measurements.

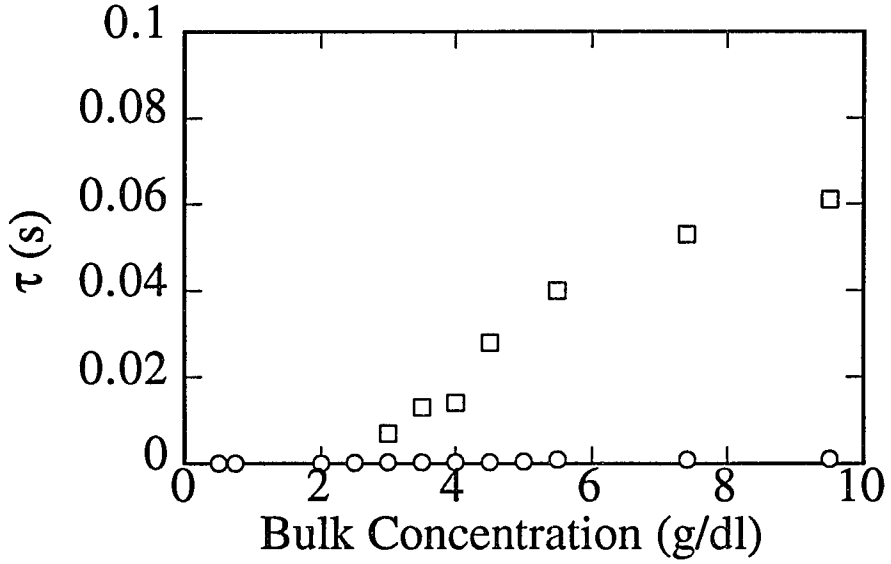

Fig. 4.33(b). Relaxation time, τ, *vs.* bulk concentration of PEO/water with M_W = 1000K. The symbols correspond to: o data obtained from the spectral fits using the theory for polymer solutions, Eq. (4.2); and □ data obtained from the fits to the rheological measurements.

This is also consistent with the high values of the elastic modulus measured with the surface light scattering.

One of the assumptions for the theory for polymer solutions is that there are no gradients of polymer concentration near the interface.[4] Since the experimental data for the PEO/water solutions with $M_w = 1000K$ can be well interpreted by the theory for polymer solutions, we can conclude that the adsorption layers of the PEO/water solutions with $M_w = 1000K$ have very limited effects on the surface waves at high concentrations. From surface tension and ellipsometry measurements, we know that $1000K$ PEO can not form dense and thick adsorption layers at the solution interface.[16] Thus, at high concentrations, the adsorption layers of $1000K$ PEO may not be large enough to affect the surface waves.

In conclusion, we have shown experimentally that the surface waves of PEO/water solutions with $M_w = 1000K$ cross over from capillary waves to elastic waves as the polymer concentration is increased. At high polymer concentrations, the peak frequency, f_p, increases with increasing polymer concentration, while the frequency width, Δf_{exp}, decreases with increasing polymer concentration. This behavior is well understood using a recent theoretical calculation by Harden *et al.*[4], who predicted a similar behavior for polymer solutions. In addition, we find that there appears to be no effect of an adsorption layer of $1000K$ PEO.

4.5 Conclusions

We use surface heterodyne light scattering to study the thermally excited surface waves at the interface between air and a polymer solution. We have demonstrated that the technique of surface heterodyne scattering can be used to probe both surface and bulk properties of polymer solutions. Three specific polymer solutions are chosen to vary the degree of surface adsorption from a depletion layer to an adsorption layer. The first solution is polyisobutylene (PIB) in decane, which exhibits no depletion or adsorption at the interface; the second one is polybromostyrene (PBrS) in toluene which exhibits a depletion layers; and the third one

is polyethyleneoxide (PEO) in water, which exhibits an adsorption layer since the polymer is surface active. Since the thicknesses of the depletion and adsorption layers depend on the molecular weight, we also study the interfacial properties of PBrS in toluene and PEO in water using polymers with both low and high molecular weights.

We measure the power spectra at several scattering vectors, and as the bulk polymer concentration and molecular weight are varied. Two theoretical models are used to analyze the experimental data. The first model uses the theory for capillary waves at a monolayer-covered liquid interface.[6] The second model uses the theory for viscoelastic polymer solutions at an air/solution interface.[4] At low polymer concentrations, both models can be reduced to describe monolayer-free liquid interfaces by setting the appropriate parameters equal to zero.

For PIB in decane, we find that the theory for viscoelastic polymer solutions is a more suitable model for relatively high polymer concentrations; it also gives better results for the surface tensions and viscosities.

For PBrS in toluene, we find that, for low molecular weight ($90K$), the surface waves lie in the capillary wave regime over the entire concentration range accessible to our experiments. By contrast, for high molecular weight ($900K$) at high polymer concentrations, the surface waves are strongly affected by the viscoelastic behavior of the bulk. In all cases, the depletion layers have no effect on the surface waves. This result is consistent with the small thickness of the depletion layers.

For PEO in water, we find that, for low molecular weight ($85K$), the surface wave motion is strongly modified by the presence of the adsorption layers. By contrast, for high molecular weight ($1000K$), the adsorption layers appear to have no effect on the surface waves. This is consistent with the results of surface tension and ellipsometry measurements, which show that $85k$ PEO forms very dense and thick adsorption layers at the solution interface while $1000K$ PEO can not form this type of adsorption layer. We also show experimentally that the surface waves of PEO/water solutions with $M_w = 1000K$ cross over from capilllary waves to elastic waves as the polymer concentration is increased.

References

1. R. T. Kambour and J. T. Bendler, *Macromolecules* **19**, 2679 (1986).

2. W. Zhao, X. Zhao, J. Sokolov, M. H. Rafailovich, M. K. Sanyal, S. K. Sinha, B. H. Cao, M. W. Kim, and B. B. Sauer, *J. Chem. Phys.* **97**, 8536 (1992).

3. M. A. Bouchiat and J. Meunier, *J. Physique* **32**, 561 (1971).

4. J. L. Harden, H. Pleiner, and P. A. Pincus, *J. Chem. Phy.* **94**, 5208 (1991).

5. J. D. Ferry, *Viscoelastic Properties of Polymers* (John Wiley & Sons, Inc., N.Y. 1980).

6. D. Langevin, *J. Colloid Interface Sci.* **80**, 412 (1981).

7. D. Byrne and J. C. Earnshaw, *J. Phys. D* **12**, 1145 (1979).

8. S. Hård and H. J. Löfgren, *J. Colloid Interface Sci.* **60**, 529 (1977).

9. S. Hård and R. D. Neuman, *J. Colloid Interface Sci.* **83**, 315 (1981).

10. Y.L. Chen, M. Kawaguchi, H. Yu, and G. Zografi, *Langmuir* **2**, 349 (1986).

11a. B.H. Cao, M.W. Kim, H. Schaffer, and H.Z. Cummins, *J. Chem. Phys.* **95**, 9317 (1991).

11b. R. B. Dorshow and L. A. Turkevich, *Phys. Rev. Letters* **70**, 2439 (1993).

12 M. W. Kim, D. G. Peiffer, and P. A. Pincus, *J. Physique. Lett.* **45**, L-953 (1984).

13. B. H. Cao, M. W. Kim, H. Z. Cummins, J. Sokolov and M. H. Rafailovich, **Molecular Weight Dependence of Surface Waves at Air/solution Interfaces of Polybromostyrene (PBrS)/toluene**, to be submitted to *Macromolecules.*

14. H. Hammarlund, L. Ilver, I. Lundström, and D. McQueen, *J. Chem. Soc. Faraday I* **69**, 1023 (1973); I. Lundström, and D. McQueen, *J. Chem. Soc. Faraday I* **70**, 2351 (1974).

15. M. W. Kim and B. H. Cao, *Europhys. Lett* **24** (3), 229 (1993).

16. B. H. Cao and M. W. Kim, **Molecular Weight Dependence of the Surface Tension of Aqueous Polyethyleneoxide (PEO) Solutions**, submitted to *J. Chem. Soc. Faraday Trans.*.

17. B. H. Cao, M. W. Kim, and H.Z. Cummins, **Adsorption effects on Surface**

Waves at Air/solution Interfaces of Polyethyleneoxide (PEO)/water, in preparation.

18. B. B. Sauer, M. kawaguchi, and H. Yu, *Macromolecules* **20**, 2732 (1987).

19. B. B. Sauer and H. Yu, *Macromolecules* **22**, 786 (1989).

20. P.-G. de Gennes, *Scaling Concepts in Polymer Physics* (Cornell Univ. Press, Ithaca, N.Y. 1979).

Appendix A

SURFACE ACTIVITY OF POLYETHYLENEOXIDE (PEO)

ABSTRACT

Adsorption characteristics of polyethyleneoxide (PEO) are investigated at an aqueous/air interface by surface tension and ellipsometry measurements as a function of polymer concentration and molecular weight.[1,2] At low polymer concentrations, we find that the adsorption isotherm is similar to that of PEO monolayers at the air/water interface, and is also molecular weight independent. This indicates that the self-assembled adsorbed films created at low polymer concentrations behave similarly to PEO monolayers at an air/water interface. However, at high polymer concentrations, we observe a novel additional surface tension reduction behavior. This additional surface tension reduction depends on both the polymer concentration and the molecular weight of PEO. This addition adsorption at high polymer concentrations can also be seen by ellipsometry measurements. This interesting phenomenon can be qualitatively explained by the change in the interaction between PEO and water molecules. The molecular weight dependence at high polymer concentrations is likely due to the hydrophilic and lipophilic balance (HLB) of PEO.

INTRODUCTION

Polyethyleneoxide (PEO: $(CH_2CH_2O)_N$) is a nonionic water soluble polymer with wide technical usage including contact lens coatings, drag reduction agents, among many other applications.[3–5] The CH_2CH_2 component is sufficiently hydrophobic to reduce the surface tension of water, and to form an adsorbed PEO layer.[6,7] Previous studies[8–10] show that PEO molecules can be spread at the air/water interface by conventional monolayer techniques. The PEO monolayers

show the same behavior as the adsorbed PEO films.[11,12] However, all of the PEO adsorption study is in a dilute polymer concentration, because the surface tension of the solution is expected to be constant in a concentration regime greater than the critical concentration.[13]

It is well known that water is a very good solvent at very dilute concentrations, but becomes a less good solvent for PEO molecules at high polymer concentrations.[14–16] This phenomena is related to changes in the hydrogen bond interaction of water and PEO molecules either through intra or inter hydrogen bonds.[17–19] Therefore, there is no reason to expect to have the same adsorption properties of PEO molecules as other surface-active materials at high polymer concentration. A recent study[20] shows a confirmational change in a adsorption layer of telechelic PEO ($C_{16}H_{33}$-PEO-$C_{16}H_{33}$: CPC) molecules on colloid particles as the polymer concentration is increased. Therefore, the interesting adsorption behavior of PEO at an air/water interface can be expected at higher PEO concentrations.

In this study[1,2], we have investigated the surface activity of PEO solutions in a wide range of polymer concentration. Since a PEO molecule has enough hydrophobic moiety (CH_2CH_2), the surface tension of polymer solutions decreases by the presence of adsorbed PEO molecules at an air/water interface as the polymer concentration is increased. Furthermore, PEO molecules can be spread at an air/water interface by conventional monolayer techniques. PEO is therefore an ideal molecule to study the interfacial properties of an adsorbed film and also a spreading monolayer film. At the same time, interesting surface behavior can be expected because of the changes in the hydrogen bonding associations of PEO molecules.

In this study, the additional surface tension reduction by adding more PEO in water is shown for the first time. Ellipsometry is used to measure the additional polymer adsorption concentration at the high polymer concentration at which the additional reduction of surface tension occurs. There is unfortunately no theoretical model to compare with these experimental data. A possible explanation to understand the additional reduction of the surface tension is given by the changes of the chemical potential of PEO molecules due to the changes of hydrogen bonding which

modify the Flory χ parameter. Furthermore, the molecular weight dependence of the additional reduction of the surface tension is likely due to the hydrophilic and lipophilic balance (HLB) of PEO.

The experimental results will be divided into two parts. The first part[1] emphasizes on the detailed studies of surface activity of $85K$ PEO. The second one[2] presents the results of molecular weight dependence measurements for PEO polymers.

In the first part,[1] PEO adsorbed films and spreading monolayers films of $85K$ were studied. To understand the additional surface tension reduction, and polymer adsorption, telechelic-PEO-molecule (CPC) monolayers with molecular weight $100K$ at the air/water interface are studied. The CPC monolayer shows the same surface pressure-area isotherm as a PEO monolayer at a low surface concentration regime, and an additional increase of the surface pressure at a high surface concentration regime, which is similar to the additional surface tension reduction of PEO solution at high polymer concentrations. A spreading monolayer of PEO is stable[8–10] so long as the surface concentration is less than $1.4mg/m^2$. However, the film becomes unstable if the surface concentration is larger than $1.4mg/m^2$ because some of the PEO chains begin dissolving into the water subphase. The solubility of PEO molecules can be reduced by adding a long hydrocarbon chain such as $C_{16}H_{33}$ located at each end of the PEO molecule. $C_{16}H_{33}$ provides a strong anchor for PEO at an air/water interface and because of the strong anchoring from the $C_{16}H_{33}$ moiety, a CPC monolayer film is very stable in the high surface concentration regime.

In the second part,[2] molecular weight dependence of PEO adsorbed films were studied. To understand the molecular weight dependence phenomenon, the surface properties of monolayers of PEO and CPC with different molecular weights are studied and compared with those of PEO solutions. Both surface tension and ellipsometry measurements will be presented.

EXPERIMENTAL SECTION

A. Material

The monodisperse PEO samples with molecular weights $0.425K$, $20K$, $85K$, $160K$, $270K$, $400K$ and $1000K$ were purchased from American Polymer Standards Corporation. M_w/M_n for all PEO samples is less than 1.05. The water used as the solvent for PEO was house distilled water further purified with a Milli-Q filtering system (Millipore) with one carbon and two ion-exchange filters. The resistance and PH values of the water was $18M\Omega/cm$, and 6.5, respectively. The $C_{16}H_{33}$-PEO-$C_{16}H_{33}$ (CPC) molecules with molecular weights $17K$, $32K$, $51K$ and $100K$ were provided from Dr. D. Ou-Yang's group at the Lehigh University. The chemical structure and details of the CPC polymer can be found in Ref. 20. The PEO polymer were used as received and were subsequently dissolved in triple distilled water for the adsorbed film (AF) behavior study. For the spreading monolayer film (MF), chloroform (Aldrich, HPLC grade) was used as a spreading solvent. Known amounts of the solution were delivered onto a water surface using a micro-syringe. The polymer monolayer formed after the spreading solvent evaporated.

B. Experimental Methods

All experiments were performed at room temperature (21.3 ± 0.5^0). The surface tensions of PEO solutions were measured using the de Nouy ring method, as discussed in chapter 3. Four readings were always taken and the values quoted are the averages from four reading. The du Nouy ring was cleaned with a flame after each measurement to prevent contamination. The surface tension of triple distilled water were measured at regular interval in order to ensure that the apparatus was indeed clean and calibrated. The surface pressure of polymer monolayers was measured by using a standard Langmuir film balance technique by monitoring the horizontal force of the monolayer against a Teflon barrier. The surface concentration was

controlled with a sliding Teflon barrier.

Ellipsometry can be used to measure the relationship of the ellipsometry phase angle change $\delta\Delta$ to the surface concentration for adsorbed films and spreading monolayers films. The phase angle change is $\delta\Delta = \Delta' - \Delta$ where Δ' and Δ are the ellipsometric phase angles for the monolayer-covered solution surface and the water surface, respectively.

The ellipsometer is based on modulation ellipsometry principles.[21] A block diagram of the ellipsometry instrument is shown in Fig. A.1. The experiments was performed at a fixed incident angle (64.0 ± 0.1^0) measured relative to the axis normal to the surface by using a $7mW$ He-Ne laser beam with $\lambda = 6328$ Å ($1mm$ beam diameter). The important component which gives high sensitivity at the air/water interface is the photoelastic modulator (Hinds International, Portland, OR, PEM-80). This modulator introduces a periodic relative phase shift between orthogonal amplitude components at a frequency of $42kHz$. Reflection from the surface causes additional phase shift and amplitude attenuation, and the phase shift was detected in the analog mode by locking into the modulation frequency.

The calibrator was used to perform a manual calibration of the instrument before a monolayer experiment, but the calibrator had no function during the actual determination of $\delta\Delta$ from a monolayer-covered surface. An increment in the calibrator corresponded to a known change in Δ, giving a relationship between the voltage measured by the multimeter (Hewlett-Packard, model 3457) and Δ.

RESULTS AND DISCUSSION

Polyethyleneoxide (PEO) with Molecular Weight 85K.

Figure A.2 shows the results of the surface tension reduction and ellipsometric signal of $85K$ PEO solutions as a function of bulk concentration. This reduction in surface tension is due to the adsorption of the PEO molecules at the solution surface. The surface tension reduction is equivalent to the surface pressure. This reduction at very dilute concentration regime (regime I in the Fig. A.2) has been studied

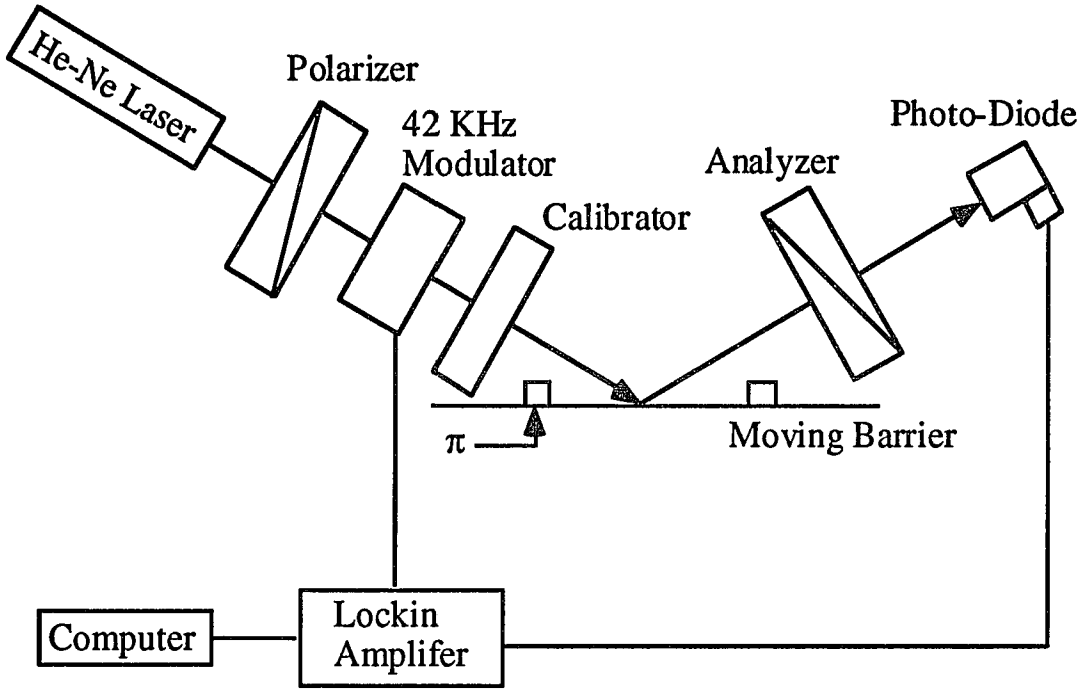

Fig. A.1. A block diagram of the ellipsometry instrument.

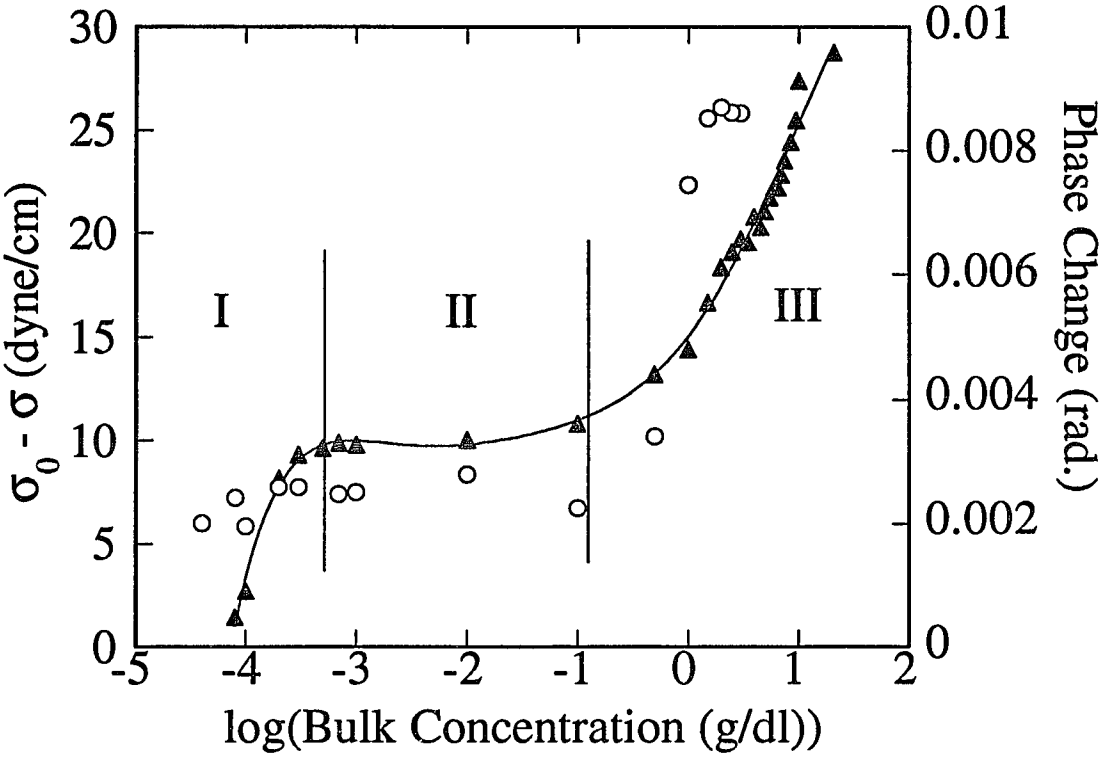

Fig. A.2. Surface pressure σ_0–σ and the change in the ellipsometric phase angle *vs.* bulk concentration of PEO solutions with M_W = 85K. The symbols correspond to: ▲ surface pressure and o ellipsometry signal. The solid line is the fit to a polynomial function.

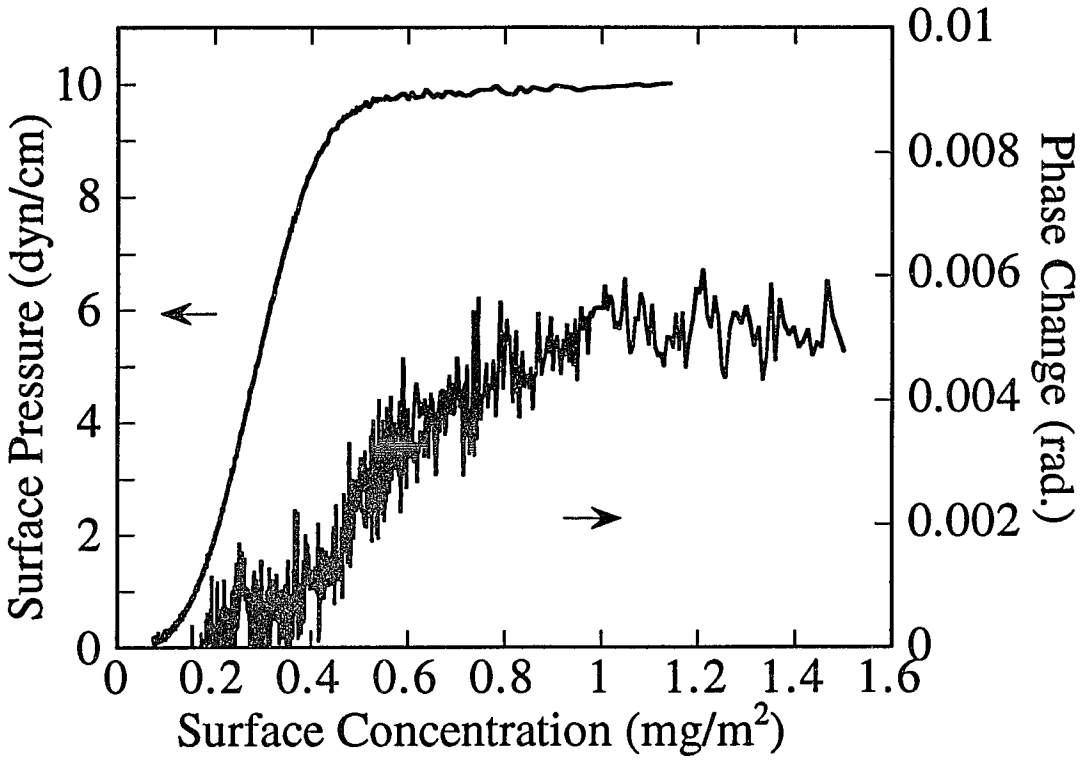

Fig. A.3. Surface pressure and the change in the ellipsometric phase angle *vs.* surface concentration of an 85K PEO monolayer.

extensively.[6,7] It is known that the properties of such an adsorbed film is very similar to those of a PEO monolayer formed by spreading.[11,12] The interesting feature in the Fig. A.2 is the second further surface tension reduction which occurs at relatively low polymer concentration (regime III), but still slightly higher than the chain overlap concentration. The overlap concentration for $85K$ PEO is $1.19g/dl$ based on the measured value of the intrinsic viscosity ($0.84dl/g$) by a Couette viscometer (Contraves).

Figure A.3 shows the surface isotherm of the monolayer of PEO with molecular weight $85K$ at an air/water interface where monolayer was compressed at very slow speed (0.025Å^2/molecule/s). We have used the modified Lauda film balance to measure the isotherm and ellipsometric signal simultaneously. The monolayer was prepared by spreading a known amount of the PEO solution onto a known initial surface area of water surface. This figure is almost identical to the results reported previously.[9] Interestingly, the saturated surface pressure is the same as the plateau value ($\sim 9.8dyne/cm$) of the surface tension reduction in the dilute polymer concentration regime.

Figure A.4 shows the surface pressure isotherm of the monolayer of CPC with molecular weight $100K$ at an air/water interface as well as the ellipsometry signal. This figure is obtained from overlapping the isotherms taken from several surface concentration ranges because of the large concentration range. The surface pressure in the overlapped surface concentration regime is the same within the experimental reproducibility ($1dyne/cm$). In the low surface concentration regime, both the surface pressure and ellipsometry signal are identical with the PEO data. The $C_{16}H_{33}$ end groups do not contribute to the surface tension and the ellipsometric signal because of their very low concentration (area per $C_{16}H_{33} > 2\times10^4\text{Å}^2$/molecule). In the intermediate polymer concentration regime, the surface pressure remains constant, but the ellipsometric signal increases with increasing polymer surface concentration. This indicates that PEO molecules are no longer dissolved into water. This behavior is very different from that of a PEO monolayer. At the high surface polymer concentration regime, both the surface pressure and ellipsometric signal increase

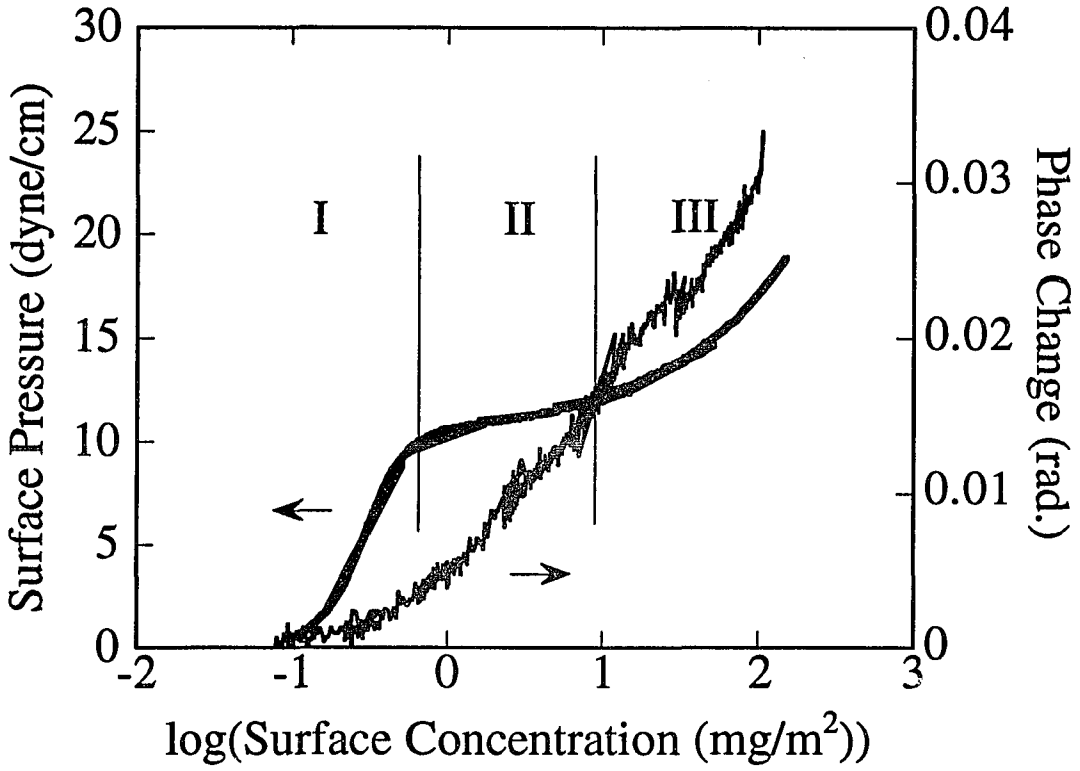

Fig. A.4. Surface pressure and the change in the ellipsometric phase angle *vs.* surface concentration of a 100K CPC monolayer.

as the surface concentration is increased. Based on the monolayer study of a long chain alcohol, the end group contribution should be of no significance even at high polymer surface concentration, because of the relatively high surface area per head group ($450Å^2$/molecule). The increase in the surface pressure should be primarily due to the contribution of PEO molecules near the interface. The surface tension reduction of PEO solution at high polymer concentration regime is likely due to the same effect, *i.e.* as observed in CPC monolayer surface pressure increasing with high surface polymer concentration.

It is interesting to see whether the surface concentration can be calculated by using the Gibbs adsorption isotherm in a dilute polymer concentration regime. Since, there is no good theoretical equation of state for the adsorbed layer, a polynomial function is used to fit the experimental adsorption data, as shown in Fig. A.2. From this polynomial curve, the surface concentration is calculated as a function of polymer concentration. The calculated surface concentration at $2.7 dynes/cm$ surface tension reduction is about one molecule in $8.2Å^2$. This is 4 times larger than the surface concentration from the spread monolayer. There are two possibilities which can explain the discrepancy. The first is that the self-assembled PEO film is not the same as a two-dimensional monolayer which only resides at the water interface. The other explanation is that the Gibbs adsorption isotherm with the 1.0 activity coefficient is not valid for the polymer adsorption phenomenon. Ellipsometry was used to measure the total amount of polymer near the surface so as to resolve which possibility is dominant.

Figure A.2 shows the signal from the ellipsometry of PEO solutions. The signal level in regime I and II is almost the same as in the monolayer case shown in Fig. A.3. This means that the adsorbed layer is very similar to the spread monolayer, This result is similar to Kawaguchi *et al* findings.[16] Based on the ellipsometry and surface tension measurement, the self-assembled film in regime I should be identical to the spread PEO monolayer. Therefore, PEO molecules in the adsorbed layer are also in the two-dimensional semi-dilute concentration regime. In other words, the surface tension reduction should be molecular weight independent which is confirmed by

the experiments results in the next part. However, the ellipsometry signal is too low to distinguish between regime 1 and regime 2 within the experimental uncertainty ($\pm 0.002 rad$).

In the intermediate polymer concentration regime (regime II), the surface tension no longer decreases as the polymer concentration is increased. In this range, the surface excess of PEO at an interface should be increased based on the chemical potential equilibrium. The behavior is similar to that of the surface concentration regime between $1.0 mg/m^2$ and $1.4 mg/m^2$ in the monolayer study. The excess amount of PEO for the monolayer is extended into the water subphase, and these excess molecules do not contribute to the reduction in the surface energy. This ineffectiveness of the sublayer on the reduction of water surface tension is also noticeable for the adsorbed film in the intermediate concentration range. This means that the polymer concentration gradient in this sublayer film contributes very little to the reduction in the surface tension compared with the PEO monolayers. Furthermore, any dielectric constant change due to a PEO sublayer is too small to be measured with ellipsometry. That is, the index of refraction of the PEO sublayer is matched to the water subphase by the highly hydrophilic nature of the strong hydrogen bond with a water molecule.

The most interesting finding is the additional surface tension reduction by adding more PEO in water. In the majority of surface active materials, the surface tension does not change with increasing concentration after a critical concentration is reached, *i.e.* critical micellar concentration (c.m.c.) or critical aggregation concentration (c.a.c.) at which the aggregates form. When the concentration is higher than the c.m.c, the solute forms aggregates in the bulk rather than adsorbing at the interface due to the equalization of the chemical potential of solute at the interface (μ_s), in bulk as a monomer (μ_m) and as an aggregate (μ_a), *i.e.* $\mu_s = \mu_m = \mu_a$. Based on a dynamic laser light scattering, there are no aggregates in the concentration regime for the PEO polymer solutions. Furthermore, the hydrogen bond interactions with a water molecule in solution should be maintained in the concentration regime studied here. In this case, the surface excess amount of PEO

molecules should increases as the PEO concentration in bulk is increased. As a consequence, the sublayer polymer concentration becomes the critical concentration that triggers the changes in the hydrogen bond interaction even though the polymer concentration in solution is much less than the critical concentration. As noted previously, the PEO molecule in the concentration regime higher than the critical concentration becomes more hydrophobic than the fully hydrogen bonded PEO chain. As a consequence, the solution surface tension decreases as the number of partially hydrogen bonding PEO molecules at the water surface increases.

The additional surface tension reduction by a PEO monolayer can not be achieved because the PEO monolayer is no longer stable at a water surface. At high surface concentrations greater than $1.4mg/m^2$, the PEO molecules dissolve into the water substrate. However, the hydrophobic end groups ($C_{16}H_{33}$) attached to the PEO molecules prevent solubilization at high surface concentrations, as shown in Fig. A.4. The CPC monolayer surface pressure isotherm clearly shows three distinct regimes including an additional surface pressure increase at high surface concentrations. The CPC monolayer isotherm is, in general, very similar to the surface tension reduction behavior of a self-assembled adsorbed PEO film. At low surface concentration (regime I), the surface pressure isotherm and ellipsometry data are very similar with those of the PEO monolayer. Furthermore, the other two high surface concentration regimes can be identified with the corresponding regimes (regime II and III) of a PEO adsorbed film. There is the possibility of forming "2D micellization" of CPC molecules by aggregating the hydrophobic end groups as show in triblock and diblock copolymer monolayers at very high surface concentrations. This can occur unless the $C_{16}H_{33}$ molecule lie down on the water surface. However, as mentioned earlier, the area per $C_{16}H_{33}$ molecule ($450Å^2$/molecule) is too large to form aggregates.

The ellipsometry measurements do not have adequate resolution in terms of the depth profile, so we cannot identify the particular structure of the PEO film. However, we can determine whether the optical property of the CPC monolayer is changed based on the linear dependence of the ellipsometry signal on surface

polymer concentration. This implies that the structure of PEO molecules of a CPC monolayer in regime I is the same as the PEO structure in a dilute polymer concentration regime. In other words, the PEO hydrogen bond interaction with a water molecule is identical to the dilute surface concentration up to $1mg/m^2$. Above $1mg/m^2$, the optical properties of PEO molecules have less contrast with the water so that the slope of the ellipsometry signal *vs.* concentration of CPC is small. At concentrations greater than $15mg/m^2$, the addition of CPC molecules at the interface forms a similar structure to the high PEO concentration adsorbed film (regime III in Fig. A.2). This highly concentrated film has hydrogen bonds with water molecules markedly different than with dilute PEO molecules. Due to the reduced hydrogen bonding between the PEO and water molecules, the effective hydrophobicity of PEO in this regime is higher than in the low surface concentration regime. As a consequence, there is an additional reduction of the surface energy with the "introduction" of the more hydrophobic molecules, *i.e.* less water bounded PEO molecules.

In conclusion, we have observed for the first time the additional surface tension reduction of PEO in solution at relatively low polymer concentration. These observations are compared with the surface pressure isotherm of an end functionalized PEO (CPC) monolayer. This additional surface tension reduction is primarily due to the formation of a highly concentrated PEO adsorbed film which causes a change in the nature of the hydrogen bonding with water. This adsorbed film formation is mainly 1) chemical potential driven, and 2) due to the breakage of hydrogen bonds between PEO and water molecules. The osmotic pressure from the chemical potential drives PEO molecules to the interface and PEO molecules becomes more hydrophobic as the surface excess increases. As a result, the surface energy decreases as the hydrophobicity of PEO chains increases. We used PEO and CPC monolayer studies to prove this proposition. Again, the CPC monolayer isotherm also shows an additional increase of the surface pressure at high surface concentration at which the ellipsometry signal shows markedly different optical properties.

Polyethyleneoxide (PEO) with Different Molecular Weights.

Figure A.5 shows the results of the surface tension reduction of PEO solutions as a function of bulk concentration for different molecular weights. In the low polymer concentration regime (regime I and II), the adsorption isotherms are similar to those of PEO monolayers at the air/water interface. Furthermore, the surface tension reductions are independent of the molecular weight of PEO; which is consistent with scaling concepts for polymer chains in the semi-dilute regime. This part of the results agrees with other works[6,7] that only measures the surface tension reduction at low bulk concentrations. This further confirms that the behavior of a self-assembled films at low PEO concentration is very similar to that of a PEO monolayer at an air/water interface. The most interesting observation in the Fig. A.5 is the second stage of the surface tension reduction in the polymer concentration regime III. In this concentration regime, the additional surface tension reduction strongly depends on the molecular weight.

Figure A.6 clearly shows how this additional surface tension reduction depends on the molecular weight of PEO by plotting the surface tension reduction for two typical bulk concentrations in regime III, *i.e.* $1.0g/dl$ and $10.0g/dl$. There is a slight increase in amount of the additional surface tension reduction as the molecular weight is increased from $0.425K$ to $85K$, then there is a decrease as the molecular weight is further increased. Finally the additional surface tension reduction disappears at $M_w = 400K$. In other words, there is an optimum molecular weight of PEO to achieve the maximum surface tension reduction of water in regime III. The objective of this part of studies is to understand the molecular weight dependence of this additional surface tension reduction. To understand this phenomenon, the surface properties of PEO and CPC monolayers were studied and compared with those of PEO solutions.

Figure A.7(a) shows the surface isotherms of the PEO monolayers at an air/water interface for two different molecular weights of PEO, *i.e.* $1000K$ and $85K$. Each monolayer was compressed at a very slow speed (0.025Å^2/molecule/s) to measure surface pressure versus area per molecule. At the same time, the ellip-

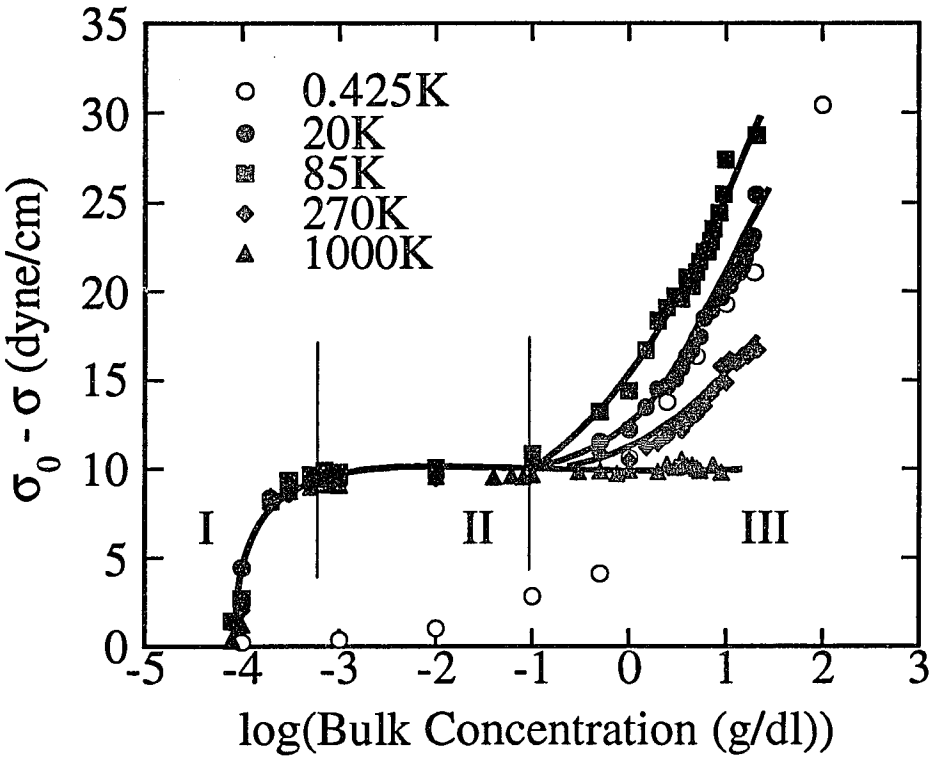

Fig. A.5. Surface pressure, $\sigma_0-\sigma$, *vs.* bulk concentration of PEO solutions with different molecular weights. The molecular weights and the corresponding symbols are shown in the legend. The solid lines are drawn through for clarity.

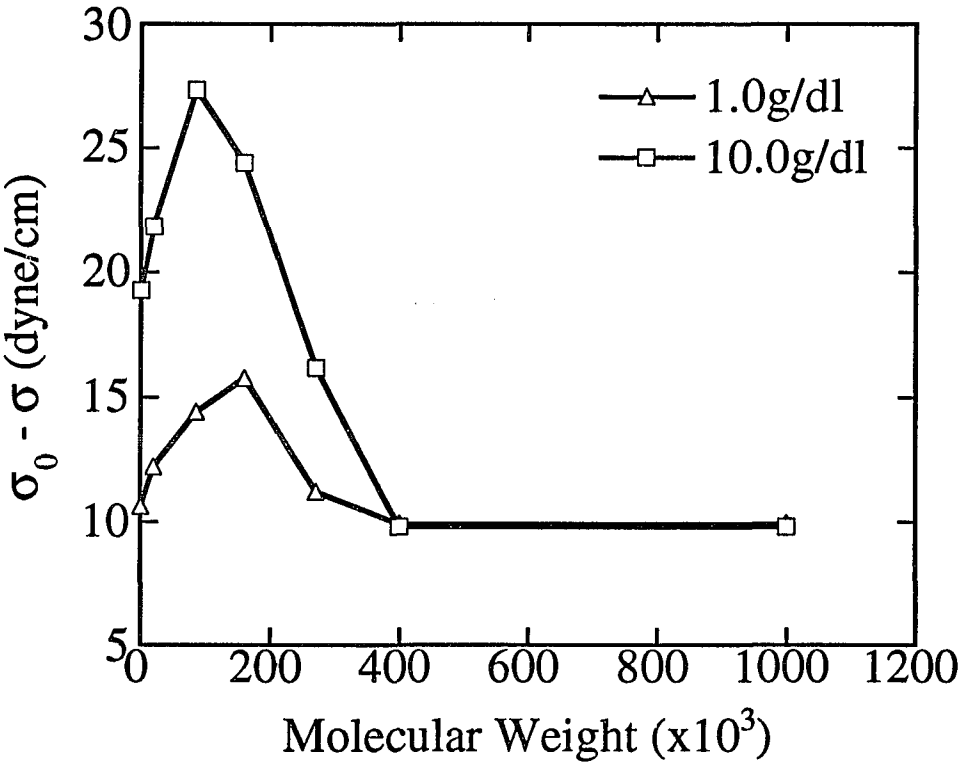

Fig. A.6. Surface pressure, σ_0–σ, *vs.* molecular weight of PEO for two typical bulk concentrations in regime III. The bulk concentrations and the corresponding symbols are shown in the legend.

sometry signal was monitored. The output of the ellipsometry signals is shown in Fig. A.7(b). The results in Figure 3(a) and Figure 3(b) are almost identical to the results reported previously,[9] and are clearly molecular weight independent.

Figure A.8 shows the surface pressure isotherms of the CPC monolayers at an air/water interface for polymers with various molecular weights. The surface isotherm is obtained from overlapping the isotherms taken from several surface concentration ranges. The surface pressure in the overlapping surface concentration regime is the same within the experimental reproducibility ($\sim 1 dyne/cm$). In the low surface concentration regime, the surface isotherms are identical with those of PEO. The $C_{16}H_{33}$ end group does not contribute to the surface tension because of the very low concentration. For example, the surface area per $C_{16}H_{33}$ for $M_w = 100K$ is $2 \times 10^4 Å^2$/molecule. Furthermore, the isotherms are molecular weight independent in this dilute surface concentration regime. For surface concentrations $> 1.4 mg/m^2$, the surface pressure isotherms depend on the molecular weight of CPC. This is very different behavior as compared with the PEO monolayer. On the basis of the monolayer study of a long chain alcohol, the end group contribution should be of no significance even at high polymer surface concentrations, because of the relatively high surface area per head group ($450 Å^2$/molecule). The increase in the surface pressure should be primarily due to the contribution of the PEO molecules.

If the PEO molecules reside at the interface and the polymer concentration is the only parameter for the additional surface tension reduction, the surface isotherms should be independent of the molecular weight of CPC because the PEO molecules are indistinguishable in the concentration regime above semi-dilute polymer concentrations. However, the surface isotherms in the high surface concentration regime strongly depend on the molecular weight of CPC polymers, as shown in Fig. A.8. This finding indicates that the PEO chains of the CPC molecules form a single monolayer with a diffused layer in which the polymer concentration is not semi-dilute. In other words, the PEO molecules form a less hydrophilic layer (hydrogen bond modified layer which we propose in the previous part)[1] with a fully

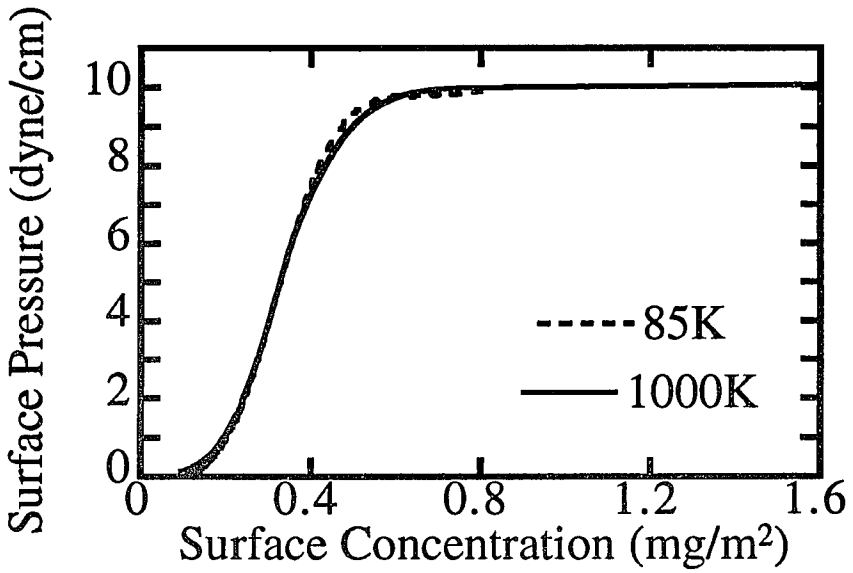

Fig. A.7(a). Surface pressure *vs.* surface concentration of PEO monolayers with two different molecular weights. The molecular weights and the corresponding lines are shown in the legend.

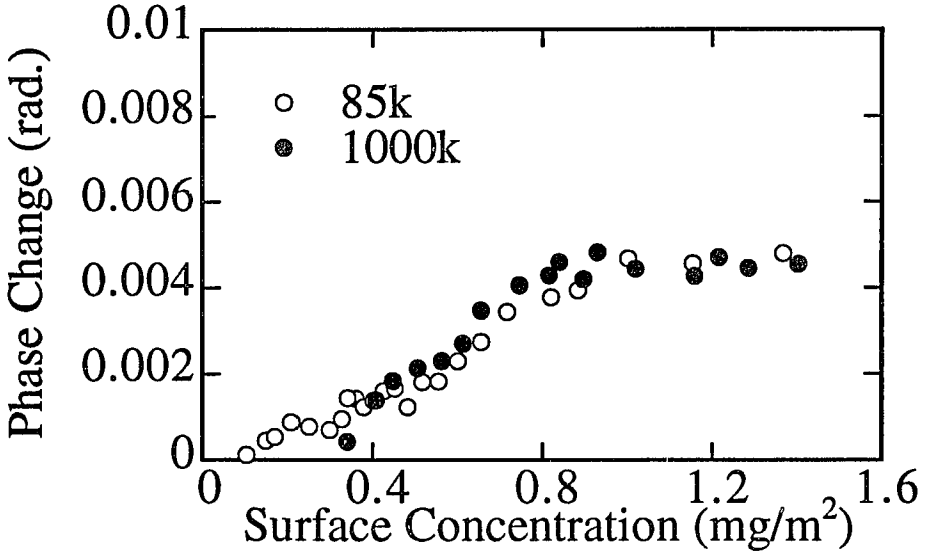

Fig. A.7(b). The change in the ellipsometric phase angle *vs.* surface concentration of PEO monolayers with two different molecular weights. The molecular weights and the corresponding symbols are shown in the legend.

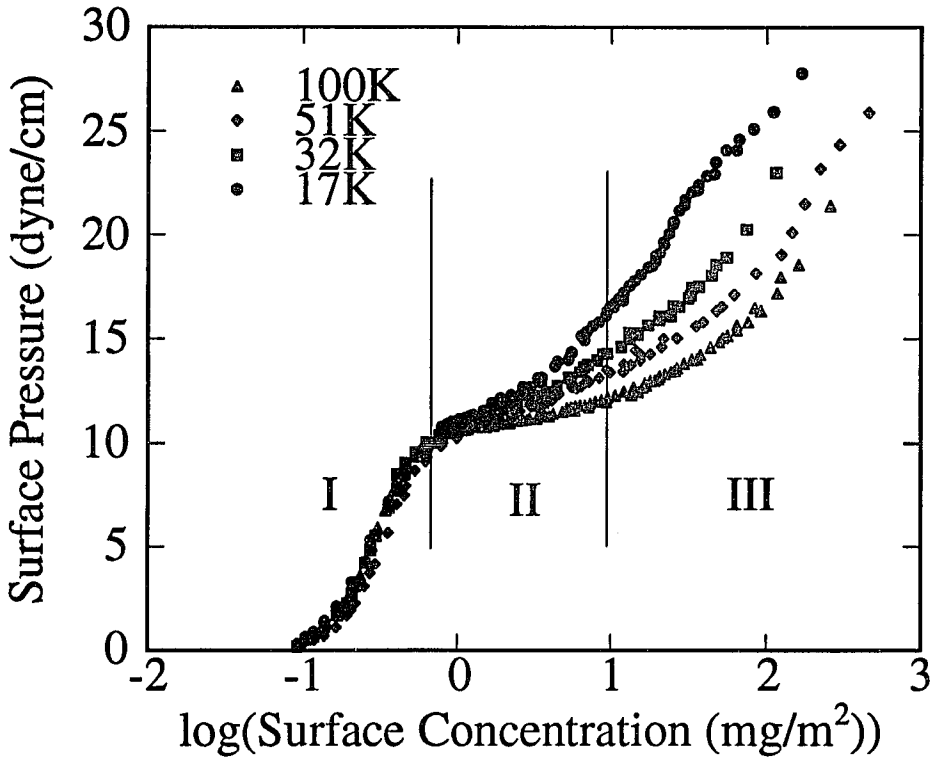

Fig. A.8. Surface pressure *vs.* surface concentration of CPC monolayers with different molecular weights. The molecular weights and the corresponding symbols are shown in the legend.

extended sublayer that controls the solubility of polymers. This two layer model of PEO molecules in CPC films can be checked by measuring the optical phase retardation (Φ) of reflected beam by ellipsometry measurements for the $100K$ CPC, as given in Fig. A.4.[1] There are two different slopes, $d\Phi/dc = 5rad.m^2/gm$, and $0.08rad.m^2/gm$, in dilute (I) and concentrated (III) regime, respectively. In the intermediate concentration regime (regime II), $d\Phi/dc = 0.8rad.m^2/gm$. The optical phase retardation with an additional polymer monolayer strongly depends on the local environment.[22] On the basis of the ellipsometry values, a PEO monomolecular layer forms initially and then a hydrogen bond modified layer (less hydrophilic), and finally, a very dilute PEO film (completely water solubilized) is arranged as adding CPC molecules on the air/water interface.

It is interesting to see the additional surface tension reduction as a function of number of $C_{16}H_{33}$ instead of the total polymer amount per surface area. Figure A.9 shows the additional surface tension reduction as a function of area per $C_{16}H_{33}$. In high concentrations, the experimental data can be fit reasonably to a single master curve. This means that $C_{16}H_{33}$ with a PEO segment can be considered as a single surfactant molecule that has same surface activity regardless of polymer molecular weight in the experimental range. In other words, the surface activity of CPC depends strongly on the anchor groups ($C_{16}H_{33}$). This means that altering the carbon length of end group or/and the molecular weight of PEO changes its hydrophilic-lipophilic balance (HLB) as well as its solubility. This observation gives a clue to understand the molecular weight dependence of the additional surface tension reduction of PEO solutions in the high polymer concentration regime (regime III).

The previous part[1] shows that the self-assembled films from the PEO solutions in the dilute concentration regime (regime I) is the same as the spread PEO monolayers at an air/water interface based on the ellipsometry and surface tension measurements. Therefore, the PEO molecules in the adsorbed layer are also in the two-dimensional semi-dilute concentration regime. In other words, the surface tension reduction in regime I should be molecular weight independent, as shown in Fig. A.5. Furthermore, Fig. A.7(b) shows that the ellipsometry signals of the

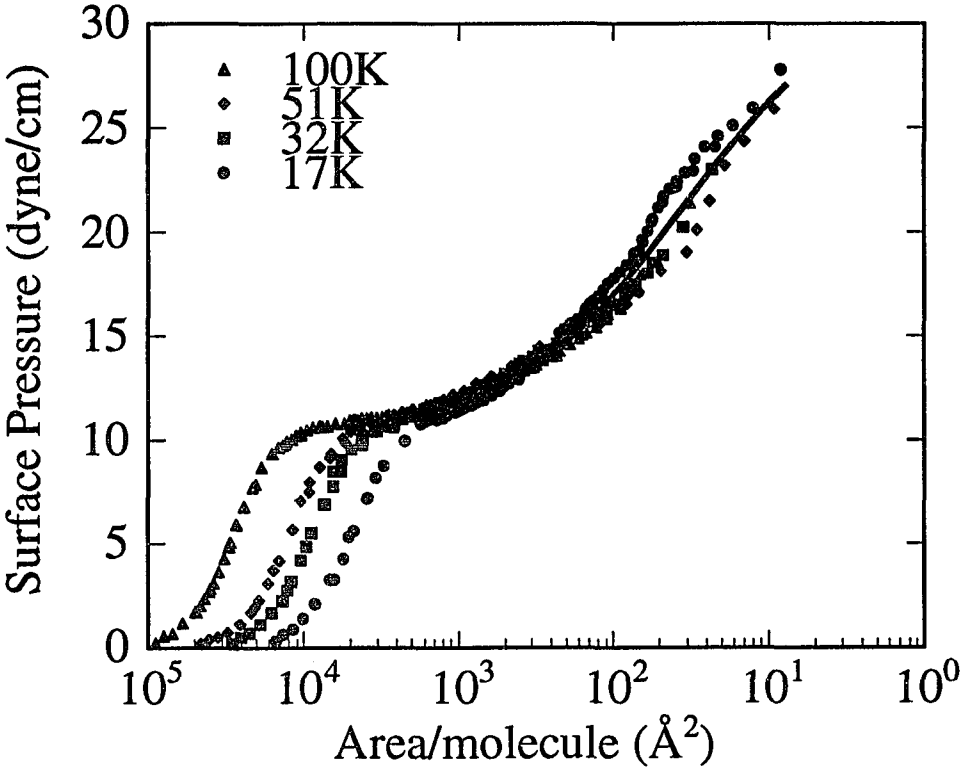

Fig. A.9. Surface pressure *vs.* area per $C_{16}H_{33}$ end group of CPC monolayers with different molecular weights. The molecular weights and the corresponding symbols are shown in the legend. The scaled experimental data collapses reasonably well onto the single solid curve.

PEO monolayers are indistinguishable for $1000K$ and $85K$ within the experimental uncertainty ($\pm 0.001 rad$). Figure A.10 shows the ellipsometry signals from the PEO solutions of $M_w = 1000K$ and $85K$. As expected, the ellipsometry signals in regime I and II are molecular weight independent.

The most interesting finding is in the high polymer concentration regime (regime III). An additional surface tension reduction for $85K$ is noted, but no additional surface tension reduction for $1000K$ is observed. As noted previously,[1] the PEO molecule in the concentration regime higher than the critical concentration becomes more hydrophobic than the fully hydrogen bonded PEO chain. As a consequence, the solution surface tension decreases as the number of partially hydrogen bonding PEO molecules at a water surface increases. This phenomenological explanation can be justified by comparing CPC monolayer study and by measuring the excess amount of PEO at the interface using ellipsometry that is shown in previous part.[1]

If the additional surface tension reduction is caused only from the less hydrophilic layer formed by hydrogen bonding modified PEO, the additional surface tension reduction should be molecular weight independent because the polymer concentration is larger than the overlapping concentration. However, the surface tension measurements for the PEO solutions indicate the strong dependence of the molecular weight of PEO, as shown in Fig. A.6. It is easy to explain the increase of the additional surface tension reduction as the molecular weight is increased. This is mainly due to the difference of the solubility of small molecules (simple liquid mixture) and the polymer adsorption. For high molecular weight PEO cases ($M_w > 400K$), the less hydrophilic layer concept is no longer applicable. But, it can be explainable by invoking the PEO monolayer instability and the CPC monolayers stability for the high surface concentration regime at an air/water interface. This is the same as the low and high values for the HLB of PEO and CPC, respectively. By increasing the molecular weight, the values of HLB for PEO are decreased. In other words, even hydrogen bond modified PEO molecules are hydroscopic, so that the end group of PEO (either CH_3 or H) can not provide sufficient anchoring strength

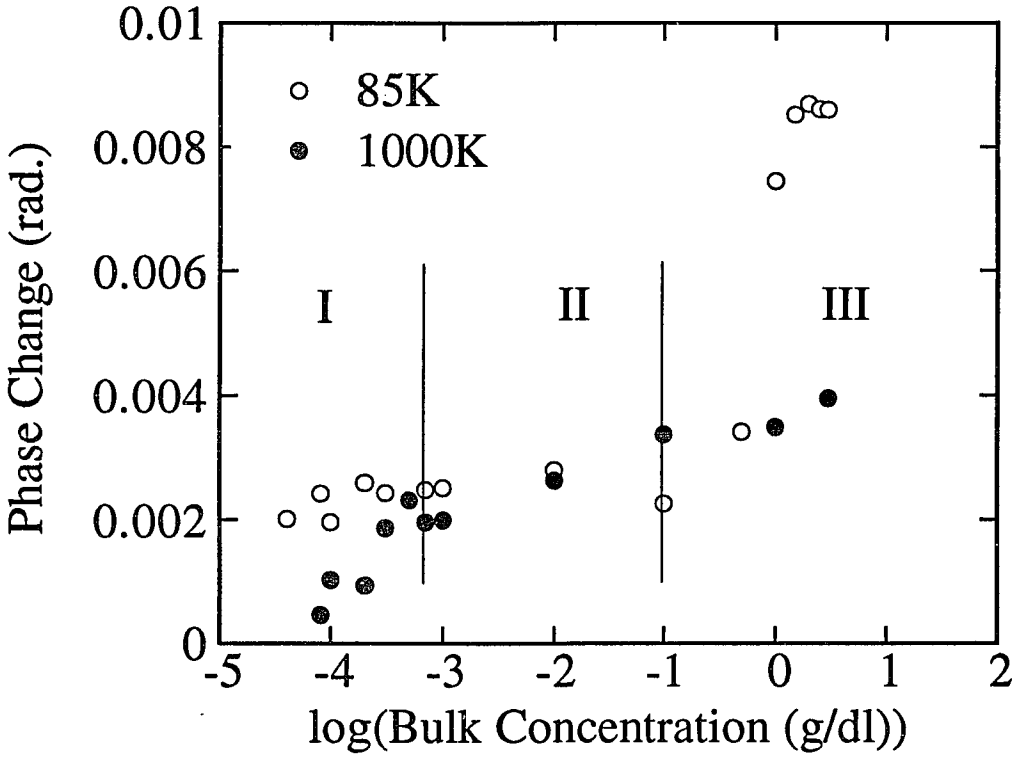

Fig. A.10. The change in the ellipsometric phase angle *vs.* bulk concentration of PEO solutions with two different molecular weights. The molecular weights and the corresponding symbols are shown in the legend.

for the PEO molecules with high molecular weights. Therefore, it is only possible to form the first monolayer. The total adsorption amount of PEO for the high molecular weight, *i.e.* $1000K$ should be smaller than that for the intermediate molecular weight, *i.e.* $85K$. This is further confirmed by the ellipsometry measurements, as shown in Fig. A.10, regime III.

In conclusion, we have observed for the first time that there is an optimum molecular weight of PEO for the additional surface tension reduction of PEO in solution at relatively low polymer concentrations. These observations are compared with the surface pressure isotherms of end functionalized PEO (CPC) monolayers. This additional surface tension reduction is primarily due to the formation of a PEO high concentrated adsorbed film that causes a change in the nature of the hydrogen bonding with water. The molecular weight dependence results from the end group effects that determine the HLB values for PEO by changing the molecular weight. As a result, the surface energy decreases as the hydrophobicity of PEO chains increases, but the solubility of PEO is also increased as the molecular weight is increased. As a consequence, there is the optimum molecular weight of PEO to have the maximum additional surface tension reduction. We studied the PEO and CPC monolayers with different molecular weights and measured the excess amount of PEO at the surface using ellipsometry to prove this proposition. It would be of interest to measure the PEO layer structure either by neutron or x-ray reflectivity to improve the understanding of this phenomenon.

References

1. M. W. Kim and B. H. Cao, *Europhys. Lett* **24** (3), 229 (1993).

2. B. H. Cao and M. W. Kim, **Molecular Weight Dependence of the Surface Tension of Aqueous Polyethyleneoxide (PEO) Solutions**, submitted to *J. Chem. Soc. Faraday Trans.*.

3. F. E. Bailey, Jr. and R. W. Callard, *Poly(ethylene oxide)* (Academic Press, N.Y. 1976).

4. G. E. Gadd, *Nature* **217**, 1044 (1968).

5. C. R. Cox, E. H. Dunlop, and A. M. North, *Nature* **249**, 243 (1974).

6. J. E. Glass, *J. Phys. Chem.* **72**, 4459 (1968).

7. M. Kawaguchi, M. Tohyama, and A. Takahashi, *Polymer, J.* **12**, 849 (1980).

8. R. L. Shuler and W. A. Zisman , *J. Phys. Chem.* **74** 1523 (1970).

9. B. B. Sauer, H. Yu, M. Yazdanian, G. Zografi, and M. W. Kim, *Macromolecules* **22**, 2332 (1989).

10. M. Kawaguchi, M. Tohyama, and A. Takahashi, *Langmuir* **4**, 411 (1988).

11. B. B. Sauer and H. Yu, *Macromolecules* **22**, 786 (1989).

12. J. C. Scott and R. W. B. Stephens, *J. Acoustical Soc. of America* **52**, 871 (1972).

13. D. K. Chattoraj and K. S. Birdi, *Adsorption and the Gibbs Surface Excess* (Plenum Press, N.Y. 1984).

14. H. Daoust and D. St-Cyr, *Macromolecules* **17**, 596 (1984).

15. P. G. de Gennes, *C. R. Acad. Sci. Ser. 2* **313**, 1117 (1991).

16. A. Matsuyama and F. Tanaka, *Phys. Rev. Lett.* **65**, 341 (1990).

17. R. L. Cook, H. E. King, Jr., and D. G. Peiffer, *Phys. Rev. Lett.* **69**, 3072 (1992).

18. D. M. Woodley, C. Dam, H. Lam, M. LeCave, K. Devanand, and J. C. Selser, *Macromolecules* **25**, 5238 (1992).

19. N. B. Graham, M. Zulfiqar, N. E. Mwachuku and A. Rashid, *Polymer* **30**, 528 (1989).

20. H. D. Ou-Yang and Z. Gao, *J. Phys. II(France)* **1**, 1375 (1991).

21. R. M. A. Azzam and N. M. Bashara, *Ellipsometry and Polarized Light* (North Holland, N.Y. 1977).

22. B.B. Sauer, H. Yu, and M. W. Kim, *Langmuir* **4**, 278 (1989).

Appendix B

INTERFACIAL PROPERTIES OF MODEL GRAFT COPOLYMERS

ABSTRACT

We combine measurements using a surface balance, ellipsometry, and surface light scattering in order to study the interfacial properties of graft copolymers at the air/water interface.[1] By using Langmuir-Blodgett (L-B) techniques to transfer the monolayers of the graft copolymers onto silica substrates, we also examine the films at the air/solid interface by atomic force microscopy (AFM). The polymers are composed of a polyethylacrylate (PEA) main chain and pendant polystyrene (PS) grafts. In addition, the copolymers have, on average, 1, 3 and 5 PS grafts per PEA chain backbone. The PEA molecules in these graft copolymers provide sufficient hydrophilic groups to form a stable monolayer. Our results show that, at low surface concentration, the surface pressure of these copolymers is mainly influenced by the PEA backbone. At high surface concentration, the surface pressure deviates from that for the PEA homopolymer, and depends on the number of PS grafts. This is mainly due to the overlap of the grafted PS chains. The interfacial structure of these graft copolymers can be derived from the results of the surface isotherm and ellipsometry measurements, and are further confirmed by the results of the surface light scattering and AFM measurements.

INTRODUCTION

The interfacial properties of homopolymers and block copolymers at the air/water interface have been studied by many researchers.[2–5] There have been, however, very few experimental studies of interfacial properties of graft copolymers at the air/water interface. The investigation of polymer monolayers at the air/water interface leads to an understanding of the static and dynamic properties

of polymer chains in two dimensions. In this study, we investigate the interfacial properties of graft copolymers composed of a polyethylacrylate (PEA) main chain onto which pendant polystyrene (PS) chains are grafted. The behavior of these copolymers at the air/water interface is studied, using a surface balance, ellipsometry, surface light scattering, and atomic force microscopy (AFM). The results from surface balance, ellipsometry, and surface light scattering measurements give direct information about the surface structure of these graft copolymers at the air/water interface, while the results from AFM measurements give information about the surface conformations of L-B films. In the latter measurements, the L-B films can be examined directly on a solid silicon substrate. For comparison, we also examine a PEA homopolymer ($M_n = 124,000 g/mole$) using these techniques. The objective of this study is to examine the interfacial structure of the graft copolymers at the air/water interface using these techniques.

It is also important to note at this junction that graft copolymers are widely used in the compatibilization of polymer blends. In a majority of case, polymeric materials are immiscible when combined. As a result of this phase incompatability, the interfacial adhesion between the components is weak. Poor mechanical properties result. In some cases, the tensile properties can be markedly improved with the formation of graft copolymers. Typically these materials are formed in-situ, *i.e.* in the melt phase, during processing. The graft copolymers can then span across the phase boundaries "tying" the interfacial region together. Markedly enhanced and technologically useful properties are found. The structure and properties of graft copolymers at the air/water interface can aid in understanding the behavior of these materials in multiphase and multicomponent blends.

Surface isotherms obtained from surface balance measurements are very useful in exploring the thermodynamic properties of polymer chains in two dimensions. In analogy with the scaling theory in three dimensions, the scaling behavior for surface isotherms can be predicted.[6] Theoretically, the radius of polymer chains in a d-dimensional space for a good solvent is expressed as a power of its degree of

polymerization, N, with an exponent, ν:[7]

$$R_F \sim N^{\nu}$$
$$\nu = 3/(d+2). \tag{B.1}$$

This Equation indicates that ν is 0.75 and 0.6 for $d = 2$ and 3, respectively. However, for a poor solvent, ν is independent of the dimension of the space, and is 0.5.

At low surface concentrations, the surface pressure is given by the expression, $\pi \sim \Gamma T/N$, where Γ is the surface concentration and T is the temperature. This is the classical result for an ideal gas of noninteracting chains. This simple model breaks down when the chains become strongly interacting. The concentration of first contact between chains is given by, $\Gamma^* \sim N/[R_{F2}]^2$, where R_{F2} is the polymer chain radius in two dimensions. For concentrations $> \Gamma^*$, scaling predicts that π can still be described as an ideal gas, but of smaller units called blobs which are of size ξ. Extending the scaling theory from three to two dimensions, we have:

$$\pi \sim \xi^{-2}. \tag{B.2}$$

The scaling form of ξ with concentration is obtained from the usual requirements that $\xi = R_{F2}$ at $\Gamma^* = \Gamma$ and that ξ has to be independent of N above Γ:

$$\xi = R_{F2}\left(\frac{\Gamma}{\Gamma^*}\right)^x \tag{B.3}$$

where $x = \nu/(1-2\nu)$. Substituting Eq. (B.3) into Eq. (B.2), we have the central result

$$\pi = \Gamma^y \tag{B.4}$$

where $y = 2\nu/(2\nu-1)$. Therefore, the determination of the exponent y from a surface pressure versus surface concentration curve yields the exponent ν for the scaling of the radius with the molecular weight for polymer chains in two dimensions. From the value of ν, one can determine whether an air/water interface is a good, or a poor solvent for the polymer monolayers.

From the surface isotherm alone, the conformational properties of polymer chains at the air/water interface cannot be deduced directly. Additional information

can be obtained from ellipsometry, which measures the relationship of the phase angle change, $\delta\Delta$, to the surface concentration, Γ, by which the interfacial structures of polymers can be obtained.[4] The phase angle change is defined as:

$$\delta\Delta = \Delta' - \Delta \qquad (B.5)$$

where Δ' and Δ are the ellipsometric phase angles for the monolayer covered surface and the water surface, respectively. Using theoretical models, the film thicknesses and refractive indices of monolayers can be calculated for various surface concentrations.[4,5] In this study, we use a sensitive phase-modulated ellipsometer[8] to examine how $\delta\Delta$ depends on Γ for graft copolymer monolayers.

While the surface pressure and ellipsometry measurements give the static interfacial properties of monolayers at an air/water interface, the surface light scattering measurements examine their dynamic interfacial properties. At the air/water interface, the capillary wave motion is determined by the interfacial tension, the viscosity and the density. However, if the interface is covered with a monolayer, the capillary wave motion is also affected by the surface transverse viscosity, μ, the surface longitudinal elasticity, ε, and the surface longitudinal viscosity, κ, of the monolayer.[9] These surface viscoelastic parameters can be extracted from the spectral data measured with the technique of surface light scattering. Monomolecular monolayers[10–12] and polymer and diblock polymer monolayers [2,3] at the air/water interface were studied using this technique. We apply the technique of surface light scattering to study the monolayers of the PEA homopolymer and its related graft copolymers at the air/water interface.

The optical techniques, *i.e.* ellipsometry and surface light scattering, can only probe macroscopic properties of the samples, since they collect the signals averaged over the beam size of the laser. By contrast, atomic force microscopy can produce topographic images of a surface with atomic resolution in all three dimensions. Moreover, AFM has the advantage of probing the surface structure for both conducting and nonconducting samples at the molecular level, and provides a sensitive and nondestructive method for investigating L-B films of these graft copolymers.

Recently, AFM has been used to image L-B films of fatty acids on mica.[13,14] We have used AFM to examine the structures of L-B films of graft copolymers to gain an insight into the monolayer structure of the graft polymers at the air/water interface. The surface structures of the films on the silica substrates can be related to those derived from the surface balance, ellipsometry, and surface light scattering measurements, by assuming that the L-B transfer does not change the structure of the polymer monolayers.

EXPERIMENTAL SECTION

A. Material

The model graft copolymers[15] were synthesized by copolymerizing an anionically polymerized macromonomer of methacrylate-terminated polystyrene (PS) with ethylacrylate. Three copolymer compositions were made containing 10, 28 and 47 weight percent PS. Since the number-averaged molecular weight (M_n) of these samples was $150,000 g/mol$ and the M_n of PS macromonomers was $14,600 g/mole$, the copolymer had, on the average, 1, 3 and 5 PS grafts per PEA backbone, respectively.

Chloroform (Aldrich, HPLC grade) was used as the spreading solvent for all polymer samples. The concentration of the spreading solutions were between 1 and $2 mg/ml$. The distilled water used was further purified with a Milli-Q filtering system (Millipore) with one carbon and two ion-exchange filters.

B. Experimental Methods

For studies of the polymer monolayers at the air/water interface, the experiments are performed at room temperature (21.3 ± 0.2^0) on a Teflon-coated Lauda trough with a width of $15 cm$. The surface pressure is measured by using the Langmuir film balance technique by monitoring the horizontal force of the monolayer

against a Teflon barrier. The surface concentration is controlled with a sliding Teflon barrier. The compression speed for all monolayers was $0.2cm^2/s$. The ellipsometer is based on modulation principles,[8] as discussed in Appendix A (Fig. A.1).

The experimental setup for surface light scattering has been described in details in Chapter 3. The essential feature of the setup is the use of a transmission grating to provide local oscillators for heterodyne beating at the photomultiplier tube (PMT). This gives us a simple method for selecting a well-defined scattering angle for each diffraction order of the grating. The grating is illuminated with a $35mW$ He-Ne laser ($\lambda = 6328$ Å) and a combination of the three lenses is used to focus simultaneously the real image of the grating on the scattering surface and the diffraction spots on the PMT. We used four different wave vectors, $k = 134.68$, 199.07, 263.30, and $331.89cm^{-1}$, in this study.

The films examined with AFM are made by transferring polymer monolayers onto the silicon (111) substrates by the standard L-B techniques. The substrate was dipped into the clean water surface (trough area = $300cm^2$) first, and then the polymer monolayer is spread. The film transfer was accomplished by lifting at a speed of approximately $4mm/min$. After one monolayer deposition, the films were stored in air in sealed containers for no more than 2 days prior to imaging with the AFM.

Atomic force microscopy uses a sharp tip mounted on a flexible cantilever. When the tip comes within a few Å of the sample's surface, forces between the atoms on the tip and those on the sample cause the cantilever to deflect. The magnitude of the deflection depends on the tip-to-sample distance. The AFM employs a piezoelectric transducer to scan the tip across the sample (Fig. B.1), and the feedback loop operates on the scanner to maintain a constant separation between the tip and the sample. Atomic force microscopy measurements were performed with a Nanoscope II-FM[16] in air, using a $15 \times 15\mu m^2$ scan head and a silicon nitride tip on a cantilever with a spring constant of $0.12N/m$. The AFM image is obtained in the so-called "force mode" by scanning the tip at the same height and measuring

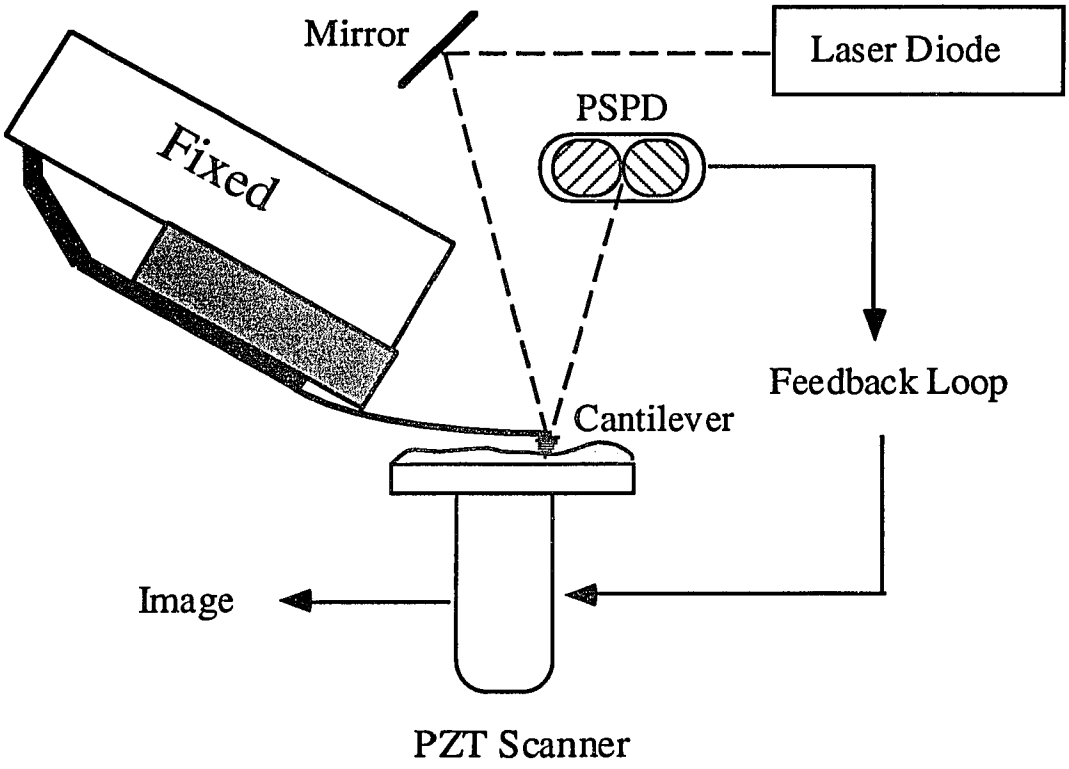

Fig. B.1. A schematic drawing of atomic force microscopy (AFM).

spring deflection.

RESULTS AND DISCUSSION

Figure B.2 shows the surface pressure, π, versus the surface concentration, Γ, for the PEA homopolymer and its related graft copolymers, the 10%-, 28%- and 47%-PS samples. For the PEA monolayer, at $\Gamma = 1.0 mg/m^2$, the surface pressure reaches a plateau of $22.5 dyne/cm$. This usually corresponds to the transition from a two-dimensional monolayer to a three-dimensional multilayer.[17] We also find that the surface isotherm of the PEA monolayer is reversible, indicating that there is no adsorption or desorption of the PEA chains into the water subphase. This is anticipated since it is known that PEA is wholly water insoluble. It is evident that there is only a slight difference between the isotherm of the PEA homopolymer and that of the 10%-PS sample. However, for the monolayers of the 28%- and 47%-PS samples, the isotherms are totally different from that of the PEA homopolymer. This indicates that the grafted PS chains have strong effects on the surface pressure of the monolayers of the graft copolymers with higher graft levels.

To directly compare the surface isotherms of these four different samples, we define a surface concentration of PEA, Γ_{PEA}, which is the measured surface concentration, Γ, multiplied by the weight ratio of the PEA backbone. In Fig. B.3, we plot the values of π as functions of Γ_{PEA}. Interestingly, we find that, at $\Gamma_{PEA} < 0.7 mg/m^2$, the isotherms fall onto the same curve, while, at higher Γ_{PEA}, they deviate from each other. This clearly shows that at low surface concentration, the surface pressure of graft copolymers is mainly influenced by the PEA backbone, and at high surface concentration, the deviations are due to the effects of the grafted PS chains.

Figure B.4 displays a logarithmic plot of π versus Γ_{PEA} for all four polymers. We find that, at $\Gamma_{PEA} < 0.7 mg/m^2$, π increases linearly with Γ_{PEA} with a slope of 3.2, while, at higher surface concentration, π deviates from this straight line. As discussed above, we can conclude that, at $\Gamma_{PEA} < 0.7 mg/m^2$, the two-dimensional monolayers of the PEA homopolymer and its related graft copolymers are in the

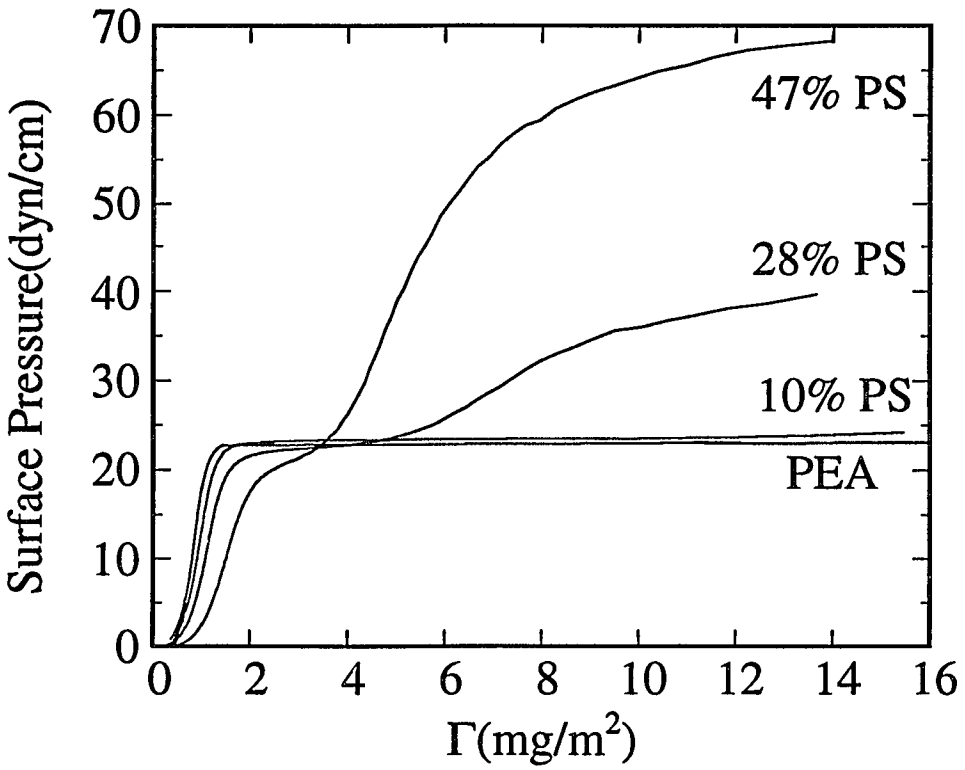

Fig. B.2. Surface pressure *vs.* surface concentration of a PEA monolayer and the related graft copolymer monolayers. The PS graft levels are shown in the plot.

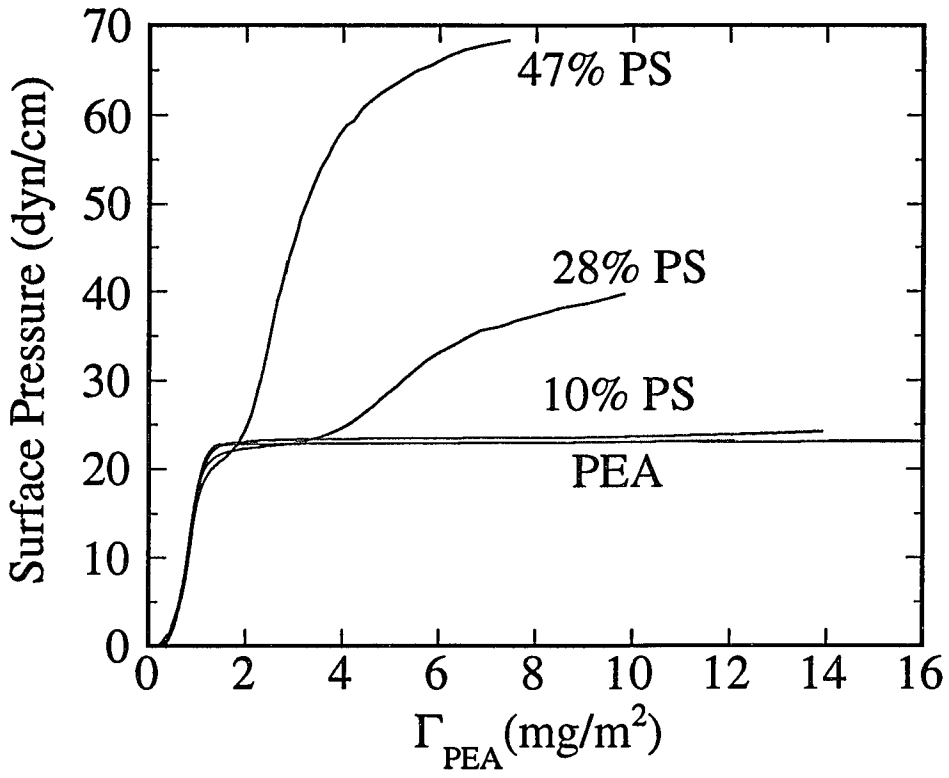

Fig. B.3. Surface pressure *vs.* the measured surface concentration after scaling by the weight ratio of the PEA backbone for PEA and its related graft copolymers. The PS graft levels are shown in the plot.

semi-dilute regime. Furthermore, the measured slope can be used to derive the exponent ν. From the slope of 3.2, we get $R_{f_2} \sim N^{0.73}$ which is in good agreement with the scaling prediction for a polymer chain configuration in two dimensions under good solvent conditions. Thus, an air-water interface behaves as a good solvent for the PEA homopolymer and its related graft copolymers in the semi-dilute regime. Previous studies indicate that an air/water interface behaves as a poor solvent for PS homopolymers.[18]

Since the PS chain is a pure hydrocarbon without any polar groups and the PEA chain has strong hydrophilic groups, we can propose a surface structure of these graft copolymers at an air/water interface. That is the PEA chains lie flat at the air/water interface, while the coiled PS chains sit on the top of the PEA chains. At low surface concentrations, the PS chains are far from each other and do not contribute to the values of the surface pressure to the graft copolymer monolayers. As the surface concentration increases, the PS chains move closer, and eventually start to contact each other. This process results in an additional contribution to the surface pressure. Thus, at high surface concentrations, the surface pressure increases rapidly with increasing surface concentration. Furthermore, at the same high Γ_{PEA}, the surface pressure of the graft copolymer monolayer depends on the PS graft level, and increases with increasing PS graft number. It is also noteworthy that the amount of the additional surface pressure is time dependent. The typical time for the surface pressure of the graft copolymer monolayer to relax to the plateau value ($\pi = 22.8 dyne/cm$) is in the range of $20 - 30 mins$. This phenomenon could be used to study the relaxation of polymer chains in two dimensions.

In Fig. B.5, we plot the ellipsometry results for PEA and its related graft copolymers. Although the surface isotherms for the graft copolymer monolayers are only reversible up to $\Gamma_{PEA} = 1.0 mg/m^2$, there is no detectable hysteresis in $\delta\Delta$ over the entire surface concentration range. This indicates that no desorption occurs for these graft copolymer monolayers. We observe that all of the ellipsometry data increases in a monotonic manner with increasing surface concentration. From this result, we can conclude that the PEA homopolymer and its related graft copolymers

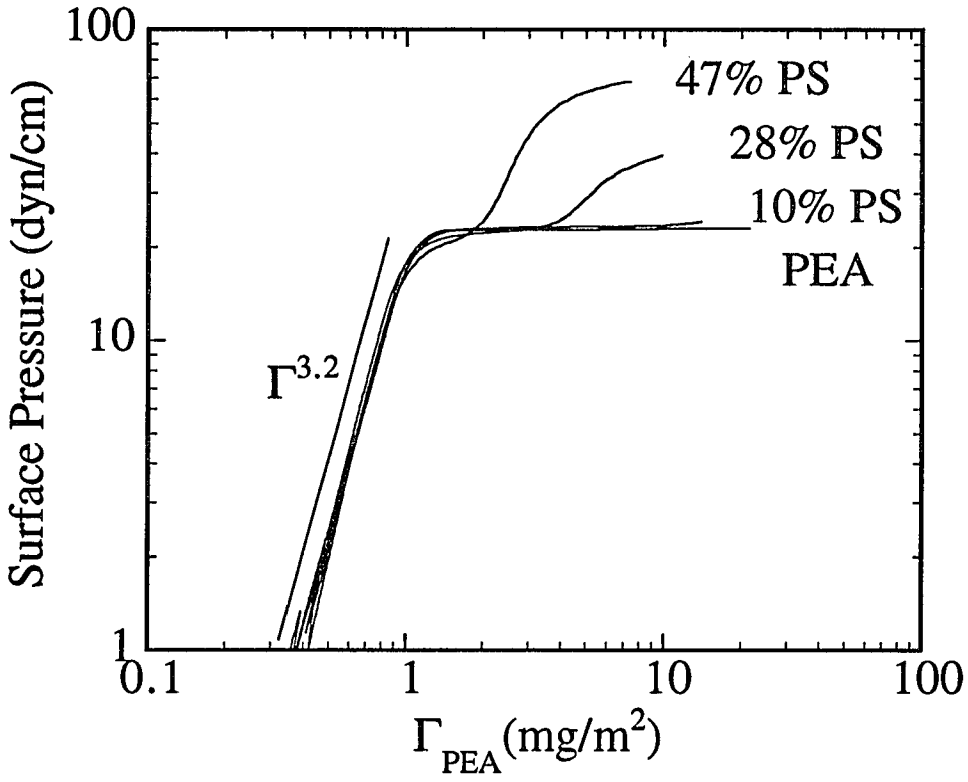

Fig. B.4. Logarithmic plot of surface pressure *vs.* the measured surface concentration (multiplied by the weight ratio of the PEA backbone) for PEA and its related graft copolymers. The PS graft levels are shown in the plot.

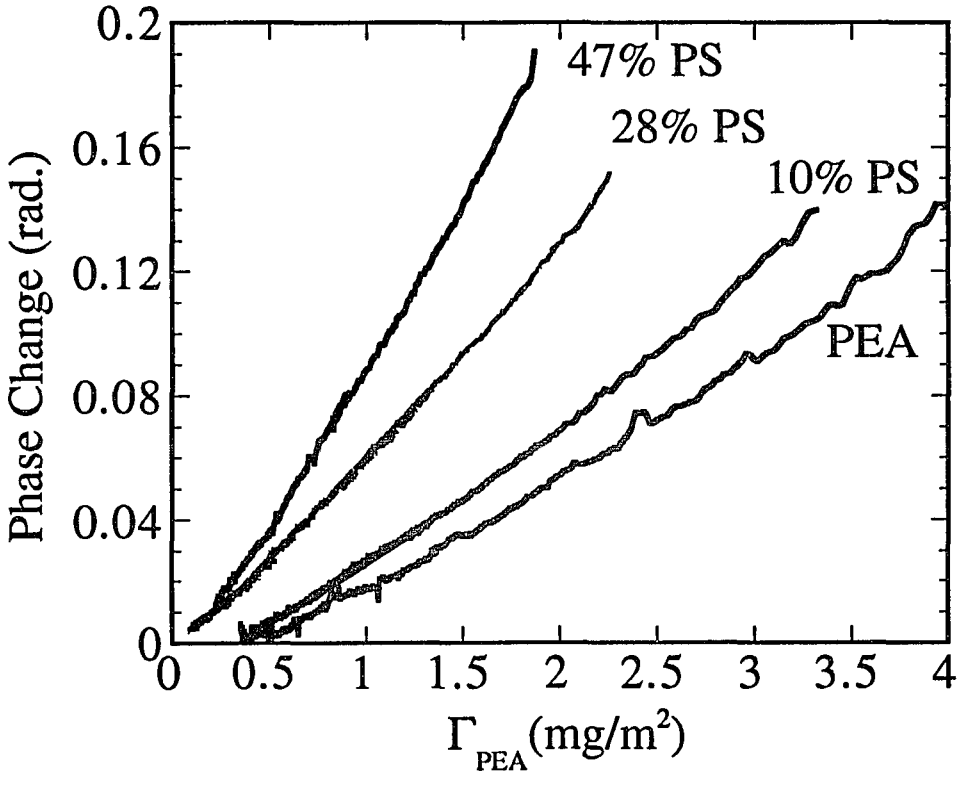

Fig. B.5. The change in the ellipsometric phase angle *vs.* the measured surface concentration (multiplied by the weight ratio of the PEA backbone) for PEA and its related graft copolymers. The PS graft levels are shown in the plot.

form uniform films at the air/water interface on a macroscopic scale. For the graft copolymers, $\delta\Delta$ increases as the PS percentage increases at the same Γ_{PEA}. This result is primarily due to the contributions from the grafted PS chains.

To probe the dynamic properties of the monolayers of the PEA homopolymer and its graft copolymers at the air/water interface, the power spectra of the capillary waves are measured. Several surface concentrations are used for each sample. Figure B.6 shows the experimental power spectra obtained for a monolayer of the graft copolymer with 28% PS at $\Gamma = 1.0mg/m^2$ and using the diffraction orders $n = 2-5$. For comparison, we also plot the fits to the capillary wave theory for monolayer-covered interfaces, Eq.(4.4). The power spectra are well described by this theory. In the spectral analysis, we use the values of the surface tension measured by the surface balance techniques. As in earlier studies,[10–12] the transverse viscosity, μ, was assumed to be negligible. We calculate the surface longitudinal elasticity, ε, and the surface longitudinal viscosity, κ, from the spectral analysis. The resultant values are shown in Figs. B.7(a) and B.7(b), respectively. To compare with the dynamic longitudinal elasticity, ε, in Fig. B.7(a) we also plot the static elasticity, ε_s, which is determined from the concentration dependence of π:

$$\varepsilon_s = \Gamma(d\pi/d\Gamma). \qquad (B.6)$$

It is seen that the dynamic longitudinal elasticity, ε, agrees quite well with the static elasticity, ε_s, at concentrations up to $\Gamma_{PEA} = 0.7mg/m^2$ for the PEA homopolymer and its related graft copolymers. Other authors have also reported similar agreement between the dynamic longitudinal elasticity, ε, and the static elasticity, ε_s.[2,3] The maximum ε is reached at the point when the monolayers of all polymers are in the fully covered state ($\Gamma_{PEA} = 0.7mg/m^2$). This result is consistent with that of the surface isotherms previously described. This suggests that for $\Gamma_{PEA} > 0.7mg/m^2$, the monolayers of all polymers examined in this study depart significantly from a two-dimensional conformation so that Eq. (B.6) no longer holds. This leads to the discrepancy between ε and ε_s values. Furthermore, for the graft copolymers at $\Gamma_{PEA} > 0.7mg/m^2$, the surface pressures are not stable and a

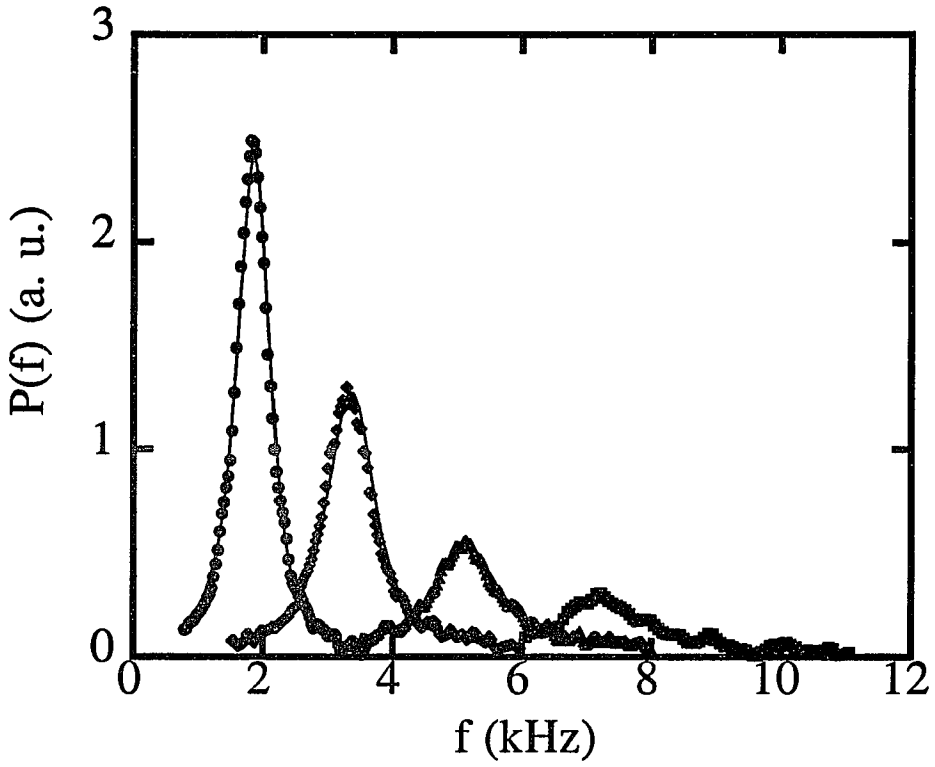

Fig. B.6. Power spectra of a monolayer of the graft copolymer with 28% PS at Γ = 1.0 mg/m^2 at the diffraction orders 2-5, corresponding to k = 134.68, 199.07, 263.30, and 331.89 cm^{-1}. They are rescaled to have the same baseline. The solids lines are the fits using Eq. (4.4). The symbols correspond to: ● n=2; ◆ n=3; ▲ n=4; and ■ n=5.

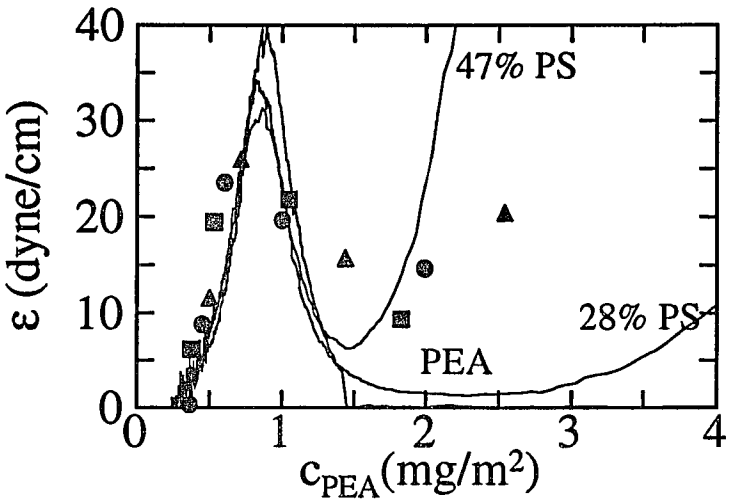

Fig. B.7(a). Surface dynamic longitudinal elasticity, ε, *vs.* the measured surface concentration (multiplied by the weight ratio of the PEA backbone) for PEA and its related graft copolymers. The symbols correspond to: ● PEA; ▲ 28% PS; and ■ 47% PS. The solid lines show the static elasticity calculated using Eq. (B.7) for all samples.

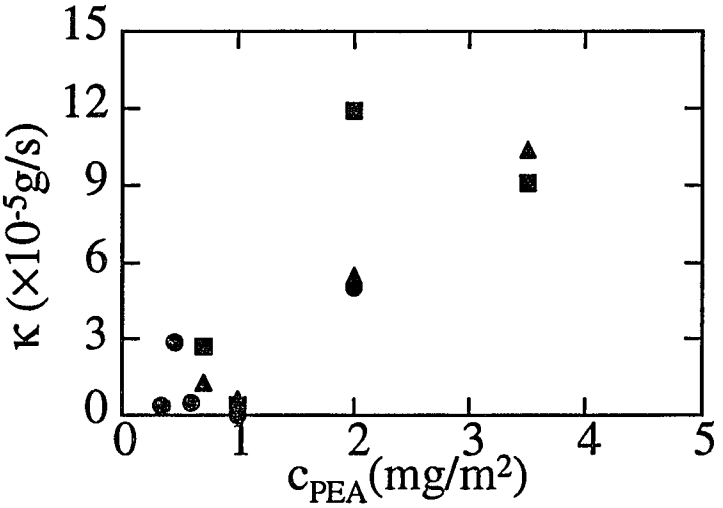

Fig. B.7(b). Surface longitudinal viscosity, κ, *vs.* the measured surface concentration (multiplied by the weight ratio of the PEA backbone) for PEA and its related graft copolymers. The symbols correspond to: ● PEA; ▲ 28% PS; and ■ 47% PS.

direct comparison between these quantities is not possible. The values of κ increase with increasing surface concentration of PEA, suggesting an initial increase of the density followed by an increase in the thickness of the monolayer.

To obtain the surface conformations of all samples on a microscopic scale, their L-B films are examined with an AFM. We assume that the surface conformation is not changed in the L-B films upon deposition from the air/water interface to the solid silicon/air interface. The AFM images cover four different surface concentrations for each material, Γ = 0.7, 1.0, 2.0, and $3.5mg/m^2$. For the PEA homopolymer, we find that, at $\Gamma < 0.7mg/m^2$, the AFM images are uniform while at higher concentrations, the AFM images indicate that the L-B films have variations in height. By contrast, for the graft copolymers the AFM images show that the L-B films are rough, even at $\Gamma = 0.7mg/m^2$. The films possess small individual grains with average lateral dimensions $\sim 7 \times 10^3 nm^2$, and an average height $\sim$ 25Å, $\sim$ 35Å, and $\sim$ 50Å for the graft copolymers with 10% PS, 28% PS and 47% PS, respectively. Since at this surface concentration, the PEA homopolymer forms uniform L-B films, we attribute this inhomogeneity to the grafted PS chains. This conclusion parallels the previously described surface isotherm measurements where it was concluded that the grafted PS chains protrude out from the monolayer surface. Therefore, the increase of the average height with the PS graft number is not unexpected. Furthermore, the large lateral dimensions of the individual grains indicate some aggregation of the grafted PS chains. We also find that for each graft copolymer, the average height is initially independent of the surface concentration. However, at higher concentrations the grains form a sponge-like, interconnected network. This phenomenon occurs at $\Gamma = 3.5mg/m^2$ for the 10%-PS and 28%-PS copolymers, and $\Gamma = 2.0mg/m^2$ for the 47%-ps copolymer. We note that the surface conformation of the L-B films also depends on the method of preparation of the materials at these high surface concentrations.

In conclusion, the interfacial properties of PEA and its related graft copolymers are studied, using a surface balance, ellipsometry, surface light scattering and AFM. We show that for the graft copolymers at $\Gamma < 0.7mg/m^2$, the interfacial properties

are mainly influenced by the PEA backbone. At higher surface concentrations, the interfacial properties depend strongly on the graft level, indicating the important contribution to the properties within the film of the grafted PS chains. It should also be noted that the results of the surface light scattering and AFM measurements are entirely consistent with those of the surface balance and ellipsometry measurements.

References

1. B. H. Cao, M. W. Kim and D. G. Peiffer, to be submitted to *Langmuir.*

2. B. B. Sauer, H. Yu, C. Tien and D. F. Hager, *Macromolecules* **20**, 393 (1987).

3. M. Kawaguchi, B. B. Sauer, H. Yu, *Macromolecules* **22**, 1735 (1989).

4. B. B. Sauer, H. Yu, M. Yazdanian, and G. Zografi, *Macromolecules* **22**, 2332 (1989).

5. M. Kawaguchi, M. Tohyama, Y. Mutoh, and A. Takahashi, *Langmuir* **4**, 407 (1988), and M. Kawaguchi, M. Tohyama, Y. Mutoh, and A. Takahashi, *Langmuir* **4**, 411 (1988).

6. R. Vilanove and F. Rondelez, *Phys. Rev. Lett.* **45**, 1502 (1980).

7. P.-G. de Gennes, *Scaling Concepts in Polymer Physics* (Cornell Univ. Press, Ithaca, N.Y. 1979).

8. R. M. A. Azzam and N. M. Bashara, *Ellipsometry and Polarized Light* (North Holland, N.Y. 1977).

9. D. Langevin, *J. Colloid Interface Sci.* **80**, 412 (1981).

10. S. Hård and H. J. Löfgren, *J. Colloid Interface Sci.* **60**, 529 (1977).

11. D. Byrne and J. C. Earnshaw, *J. Phys. D: Appl. Phys.* **12**, 1145 (1979).

12. S. Hård and R. D. Neuman, *J. Colloid Interface Sci.* **83**, 315 (1981).

13. R. Viswanathan, D. K. Schwartz, J. Garnaes, and J. A. N. Zasadzinski, *Langmuir* **8**, 1603 (1992).

14. D. K. Schwartz, R. Viswanathan, and J. A. N. Zasadzinski, *Phys. Rev. Lett.* **70**, 1267 (1993).

15. W. D. Dozier, P. Thiyagarajan, D. G. Peiffer, M. Rabeony, M. Y. Lin, G. Agrawal and R. P. Wood, *Polymer*, accepted for publication (1994).

16. Digital Instruments, Inc., Goleta, CA 93117.

17. D. J. Crisp, *J. Colloid Sci.* **1**, 49 (1949).

18. M. W. Kim and D. G. Peiffer, *Polymer* **30**, 668 (1989).

Bibliography

Azzam, R. M. A. and Bashara, N. M., *Ellipsometry and Polarized Light* (North Holland, N.Y. 1977).

Bailey, Jr., F. E. and Callard, R. W., *Poly(ethyleneoxide)* (Academic Press, N.Y. 1976).

Berne, B. J. and Pecora, R., *Dynamic Light Scattering* (Wiley-Interscience, N.Y. 1976).

Billmeyer, JR., F. W., *Textbook of Polymer Sciences* (John Wiley & Sons, Inc., N.Y. 1984).

Bouchiat, M. A. and Meunier, J., *C. R. Acad. Sc. Paris* **266B**, 301 (1969).

Bouchiat, M. A. and Meunier, J., *J. Physique* **32**, 561 (1971).

Byrne, D. and Earnsharw, J. C., *J. Phys. D: Appl. Phys.* **12**, 1133 (1979).

Byrne, D. and Earnshaw, J. C., *J. Phys. D* **12**, 1145 (1979).

Cao, B. H.; Kim, M. W.; Schaffer, H.; and Cummins, H. Z., *J. Chem. Phys.* **95**, 9317 (1991).

Cao, B. H. and Kim, M. W., *Molecular Weight Dependence of the Surface Tension of Aqueous Polyethyleneoxide (PEO) Solutions*, submitted to *J. Chem. Soc. Faraday Trans.*

Cao, B. H.; Kim, M. W.; Sokolov J.; and Rafailovich, M. H., *Depletion Layer Effects on Surface Waves at Air/solution Interfaces of Polybromostyrene (PBrS)/toluene,* submitted to *Macromolecules.*

Cao, B. H.; Kim, M. W.; and Cummins, H. Z., *Surface Wave on Polymer Solutions: Complete Capillary-wave Elastic-wave Crossover,* submitted to *J. Chem. Phys.*

Cao, B. H. and Kim, M. W., *Adsorption Layer Effects on Surface Waves at the Polyethyleneoxide (PEO) Solution/air Interface,* submitted to *Europhys. Lett.*

Cao, B. H. and Kim, M. W., *Surface Activity of Polyethyleneoxide (PEO),* to be submitted to *Phys. Rev. E.*

Cao, B. H.; Kim M. W.; and Peiffer, D. G., *Interfacial Properties of Model Graft Copolymers,* submitted to *Langmuir.*

Chattoraj, D. K. and Birdi, K. S., *Adsorption and the Gibbs Surface Excess* (Plenum, N.Y. 1984).

Chen, Y. L.; Kawaguchi, M.; Yu, H.; and Zografi, G., *Langmuir* **2**, 349 (1986).

Chen, Y. L.; Kawaguchi, M.; Yu, H.; and Zografi, G., *Langmuir* **3**, 31 (1987).

Chu, B., *Laser Light Scattering* (Academic Press, N.Y. 1974), Ch. IV.

Cox, C. R.; Dunlop, E. H.; and North, A. M., *Nature* **249**, 243 (1974).

Crisp, D. J., *J. Colloid Sci.* **1**, 49 (1946).

Cummins, H. Z. and Swinney, H. L., *Prog. Opt.* **8**,.133 (1970).

Cummins, H. Z. and Pike, E. R., *Photon Correlation and Light Beating Spectroscopy* (Plenum Press, N.Y. 1974).

Cummins, H. Z. and Pike, E. R., *Photon Correlation Spectroscopy and Velocimetry* (Plenum Press, N.Y. 1977).

de Gennes, P. -G., *Macromolecules* **9**, 594 (1976).

de Gennes, P.-G., *Scaling Concepts in Polymer Physics* (Cornell Univ. Press, Ithaca, N.Y. 1979).

de Gennes, P. G., *C. R. Acad. Sci. Ser.* 2 **313**, 1117 (1991).

Daoust, H. and St-Cyr, D., Macromolecules 17, 596 (1984).

Digital Instruments, Inc., Goleta, CA 93117.

Dorrestein, R., *Koninkl. Ned. Akad. Wetenshap. Proc.* **B54**, 260 (1951).

Dorshow, R. B.; Hajiloo, A.; and Swofford, R. L., *J. Appl. Phys.* **63**, 1265 (1988).

Dorshow, R. B. and Turkevich, L. A., *Phys. Rev. Letters* **70**, 2439 (1993).

Ferry, J. D., *Viscoelastic Properties of Polymers* (John Wiley & Sons, Inc., N.Y. 1980).

Fleury, P. A. and Boon, J. P., in *Advances in Chemical Physics* edited by Prigogine, I. and Rices, S. A. (John Wiley and Sons, N.Y. 1973); Vol. 24., and references therein.

Flory, P., *Principles of Polymer Chemistry* (Cornell University Press, Ithaca, N.Y. 1971).

Gadd, G. E., *Nature* **217**, 1044 (1968).

Gaines, G. L., *Insoluble Monolayers at the Liquid Gas Interface*, (Wiley, N.Y, 1966).

Glass, J. E., *J. Phys. Chem.* **72**, 4459 (1968).

Goodrich, F. C., *J. Phys. Chem.* **66**, 1858 (1962).

Cook, R. L., King, Jr., H. E.; and Peiffer, D. G., *Phys. Rev. Lett.* **69**, 3072 (1992).

Dozier, W. D.; Thiyagarajan, P.; Peiffer, D. G.; Rabeony, M.; Lin, M. Y.; Agrawal G.; and Wood, R. P., *Polymer,* accepted for publication (1994).

Graham, N. B.; Zulfiqar, M.; Mwachuku, N. E.; and Rashid, A., *Polymer* **30**, 528 (1989).

Hansen; R. S. and Mann, J. A., *J. Appl. Phys.* **35**, 152 (1964).

Hammarlund, H.; Ilver, L.; Lundström, I.; and McQueen, D., *J. Chem. Soc. Faraday I* **69**, 1023 (1973).

Hård, S.; Hamnerius, Y.; and Nilsson, O., *J. Appl. Phys.* **47**, 2433 (1976).

Hård, S. and Löfgren, H. J., *J. Colloid Interface Sci.* **60**, 529 (1977).

Hård, S. and Neuman, R. D., *J. Colloid Interface Sci* **83**, 315 (1981).

Harden, J. L.; Pleiner, H.; and Pincus, P. A., *J. Chem. Phys.* **94**, 5208 (1991).

Harkins, W. D. and Jordan, H. F., *J. of Am. Chem. Soc.* **52**, 1751 (1930).

Herpin, J. C. and Meunier, J., *J. Phys. (Paris)* **35**, 847 (1974).

Jon, D. I.; Rosano, H. L.; and Cummins, H. Z., *J. Colloid Interface Sci.* **114**, 330 (1986).

Kambour, R. T. and Bendler, J. T., *Macromolecules* **19**, 2679 (1986).

Katyl, R. H. and Ingard, U., *Phys. Rev. Lett.* **19**, 64 (1967).

Katyl, R. H. and Ingard, U., *Phys. Rev. Lett.* **20**, 248 (1968).

Kawaguchi, M.; Tohyama, M.; and Takahashi, A., *Polymer, J.* **12**, 849 (1980).

Kawaguchi, M.; Tohyama, M.; Mutoh, Y. and Takahashi, A., *Langmuir* **4**, 407 (1988).

Kawaguchi, M.; Tohyama, M. and Takahashi, A., *Langmuir* **4**, 411 (1988).

Kawaguchi, M.; Sauer, B. B.; and Yu, H., *Macromolecules* **22**, 1735 (1989).

Kim, M. W. and Peiffer, D. G., *Polymer* **30**, 668 (1989).

Kim, M. W.; Peiffer, D. G.; and Pincus, P. A., *J. Physique. Lett.* **45**, L-953 (1984).

Kim, M. W. and Cao, B. H., *Europhys. Lett* **24** (3), 229 (1993).

Kramer, L., *J. Chem. Phys.* **55**, 2097 (1971).

Landau, L. D. and Lifshitz, E. M., *Fluid Mechanics* (Pergamon Press, N.Y. 1959), Ch. VII.

Landau, L. D. and Lifshitz, E. M., *The Theory of Elasticity* (Pergamon Press, N.Y. 1959).

Landau, L. D. and Lifshitz, E. M., *Statistical Mechanics* (Pergamon Press, N.Y. 1980).

Langevin, D. and Bouchiat, M. A., *C. R. Acad. Sci. Paris* **272B**, 1422 (1971).

Langevin, D., *J. Chem. Soc. Faraday Trans.1* **70**, 95 (1974).

Langevin, D. and Griesmar, C. J., *J. Phys. D: Appl. Phys.* **13**, 1189 (1980).

Langevin, D., *J. Colloid Interface Sci.* **80**, 412 (1981).

Levich, V., *Physiochemical Hydrodynamics* (Prentice Hall, Englewood Cliffs, N.J. 1962).

Lundström, I. and McQueen, D., *J. Chem. Soc. Faraday I* 70, 2351 (1974).

Mann, J. A., in *Surface and Colloid Science* edited by E. Matijevic and R. J. Good (Plenum Press, N.Y. 1984; Vol 13, P145).

Matsuyama, A. and Tanaka, F., *Phys. Rev. Lett.* **65**, 341 (1990).

Ou-Yang, H. D. and Gao, Z., *J. Phys. II (France)* **1**, 1375 (1991).

Pleiner, H.; Harden, J. L.; and Pincus, P. A., *Europhys. Lett.* 7(5), 383 (1988).

Pouchelon, A.; Meunier, J.; Langevin, D.; and Cazabat, A. M., *J. Phys. (Paris)* **41,** 1239 (1980).

Sano, M.; Kawaguchi, M.; Chen, Y-L.; Skarlupka, R. L.; Chang, T.; Zografi, G.; and Yu, H., *Rev. Sci. Instrum.* **57**(6), 1158 (1986).

Sauer, B. B.; Yu, H.; Tien, C.; and Hager, D. F., *Macromolecules* **20**, 393 (1987).

Sauer, B. B.; kawaguchi, M.; and Yu, H., *Macromolecules* **20**, 2732 (1987).

Sauer, B. B. and Yu, H., *Macromolecules* **22,** 786 (1989).

Sauer, B. B.; Yu, H.; Yazdanian, M.; Zografi, G.; and Kim, M. W., *Macromolecules* **22,**

2332 (1989).

Sauer, B. B.; Yu, H.; and Kim, M. W., *Langmuir* **4,** 278 (1989).

Schwartz, D. K.; Viswanathan, R.; and Zasadzinski, J. A. N., *Phys. Rev. Lett.* **70**, 1267 (1993).

Scott, J. C. and Stephens, R. W. B., *J. Acoustical Soc. of America* **52**, 871 (1972).

Shuler, R. L. and Zisman W. A., *J. Phys. Chem.* **74**, 1523 (1970).

van den Tempel, M. and van de Riet, R. P., *J. Chem. Phys.* **42**, 2769 (1965).

Vilanove, R. and Rondelez, F., *Phys. Rev. Lett.* **45**, 1502 (1980).

Viswanathan, R.; Schwartz, D. K.; Garnaes, J.; and Zasadzinski, J. A. N., *Langmuir* **8**, 1603 (1992).

Woodley, D. M.; Dam, C.; Lam, H.; LeCave, M.; Devanand, K.; and Selser, J. C., *Macromolecules* **25**, 5238 (1992).

Wu, X. Z.; Ocko, B. M.; Sirota, E. B.; Sinha, S. K.; Deutsch, M.; Cao B. H.; and Kim, M. W., *Science* **261**, 1018 (1993).

Zhao, W.; Zhao, X.; Sokolov, J.; Rafailovich, M. H.; Sanyal, M. K.; Sinha, S. K.; Cao, B. H.; Kim, M. W.; and Sauer, B. B., *J. Chem. Phys.* **97**, 8536 (1992).

Zuidema, H. H. and Walters, G. W., *ASTM Bull.* **13**, 312 (1941).